ABSTRACT

Title of Dissertation: OPTIMAL MEMS PLATE DESIGN AND CONTROL FOR LARGE CHANNEL COUNT OPTICAL SWITCHES

Yuan Ma, Doctor of Philosophy, 2004

Dissertation Directed By: Professor Robert W. Newcomb, Department of Electrical and Computer Engineering

The design and control of an optimal mirror plate actuator suitable for large channel count MEMS optical switch applications is researched. An optimal plate actuator structure is presented. Its performance in equilibrium status is analyzed. A design example, which is confirmed by ANSYS simulation, is given along with a design methodology. By considering the squeeze film damping effects, the transient response of this optimal plate actuator is performed. The system stability is proven by using a Lyapunov function and the Routh-Hurwitz test. A conclusion is that the optimal tilted bottom plate can stably approach the maximum tilt angle with the minimum applied actuating voltage, which is one-half of the present industry standard actuating voltage. A four-level stage structure is given as an example of a practical multi-step realization of such an optimal plate structure. A feedback control system is described using a sensing bridge with a sensing capacitor. Two optimal control methodologies are described, these being fast switching bang-bang control and closed loop feedback

control. A high voltage driving circuit is introduced along with design equations based on the special features needed in MEMS mirrors. In addition, by introducing a shift register, a modular architecture to control MEMS mirrors for scalable embedded systems is described. By using this modular structure with its shift register, the system can be scaled when there is a future need to increase channel counts.

Overall, this research improves upon the performance of large channel count MEMS optical switches. It achieves low actuating voltage by reducing by one-half of the present industry standard actuating voltage, that is, a reduction from 250V to 120V. By using the new high voltage driving circuit, it cuts in half the number of required control actuating voltages. It obtains a scalable structure for the embedded system, which is beneficial to cost reduction, future maintainability and design simplification. It provides optimal control to switch the mirrors in order to achieve the minimum switching time and to maintain the stability of the system in the appearance of any perturbation.

OPTIMAL MEMS PLATE DESIGN AND CONTROL FOR LARGE CHANNEL COUNT OPTICAL SWITCHES

By

Yuan Ma

Dissertation submitted to the Faculty of the Graduate School of the
University of Maryland, College Park, in partial fulfillment
of the requirements for the degree of
Doctor of Philosophy
2004

Advisory Committee:
Professor Robert Newcomb, Chair
Professor Neil Goldsman
Professor Tien-Mo Shih
Professor Martin Peckerar
Professor John Melngailis
Dr. Xiqun Zhu

Dedication

This dissertation is dedicated to my family, to their love and support

How could a blade of grass

Repay the warmth from the spring sun

-Meng Jiao (751-814)

Acknowledgements

I would like to express my special thanks to Dr. Newcomb for his advice and support to write this dissertation. Without him, this research is not possible.

I would like to express my special thanks to Dr. Goldsman for his advice and support during my whole Ph.D study.

I am grateful to Dr. Peckerar and Dr. Melngailis for their advice and support. They were in my Ph.D qualify exam committee and are in my dissertation committee.

I am grateful to Dr. Shih to serve in my dissertation committee. I appreciate his advice and support.

I thank Miss Koranan Limpaphayom for her help on PSpice and MATLAB.

Last not least, I want to express my thanks to Dr. Zhu for his advice and support. Valuable discussions with him have helped to shape some concepts in this dissertation.

Table of Contents

List of Tables

List of Figures

Chapter 1: Introduction

Abstract

In this chapter, we present the introduction to this dissertation along with the outline of its structure. An overview is given on MEMS emphasizing its applications to the optical switch. Different actuation methods to activate MEMS are reviewed and compared, with the conclusion to use electrostatic actuation in the MEMS mirror for the optical switch. After a review of the research work that has been done in the areas to reduce the actuating voltage and to provide optimal control, the contributions of this dissertation are presented.

1.1 Concept of MEMS with its applications to the optical switch

MEMS, "Micro-Electro-Mechanical System", provides the motion-ability to an otherwise all-stationary electrical system. By taking advantage of today's matured planar integrated circuit process, MEMS technology has been springing rapidly into various areas [1] [2] [3], such as the MEMS projection display technology provided by Texas Instruments Inc. [4] [5] and MEMS based thermal inkjet heads from HP [6]. One of its most noticeable application areas is in optical telecommunication systems [3]. With considerable technology advances in MEMS along with the system demands in optical layered networks, MEMS based all optical components, such as optical switches, variable optical attenuators, and tunable lasers, have shown their great potentials; and some of these have been put into use in systems[1][8][9][10][11][28].

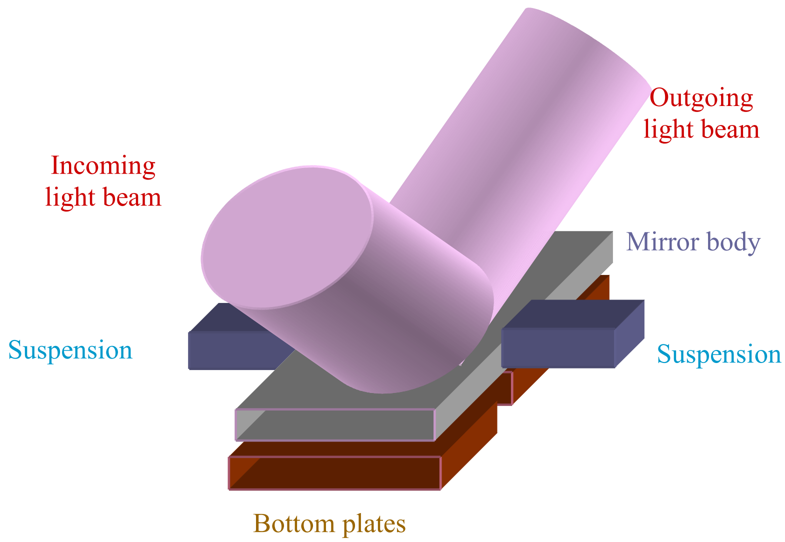

Figure 1-1 A typical structure of a MEMS electrostatic actuator

A typical MEMS mirror actuator in the optical switch applications is shown in Figure 1-1 [12]. Mainly the mirror structure is composed of three parts, the mirror body, the bottom plates and the holding suspensions. The light beam is reflected by the upside surface of the mirror body. The mirror body can rotate around its axis, which is mechanically held by the suspensions. The bottom plates are fixed in position.

Actuating voltage is applied on the top mirror body and the bottom plate. As shown in Figure 1-1, when an electrical voltage potential difference exists between the mirror and one of the bottom plates, the mirror rotates around its axis an amount determined by this applied torque (due to this potential difference). As long as the mirror rotates, a spring torque is applied to the mirror body from the suspension structures. Damping torque also appears, proportional to the rotational angular velocity. When the balance between these three torque is reached, the mirror is settled down at some equilibrium point. Thus we have successfully tilted the mirror to some desired angular position. Then the mirror can reflect the light beam from the input fiber to the output fiber. More details will be covered in Chapter 2.

With the outgrowth in fiber optical communication at the end of the twentieth century fueled by the need of Internets and IP (Internet protocol) technology, major long haul telecommunication transmission has mostly migrated to optical transmission with WDM (Wavelength Division Multiplexing) technology, which has demands for large channel count optical switches that can handle optical signals with no restriction on wavelength and data rate. Two important functions are required for an optical switch. One is to restore a failed connection inside the network and the other is to make new connection provisioning [3] [12] [27]. As a very important optical component in a long haul telecommunication layered network, an optical switch system performs the function to connect and bypass the failed channel-path or to reconfigure the optical path according to the whole system load schedule change [27].

Optical switches can be basically put into two main categories based on how the optical signals are handled. One is called an OEO (optical–electrical-optical) switch, where the optical signals are translated to electrical ones to be preceded and are translated back to optical ones afterwards. The other category is called an OOO (optical–optical-optical) or an all-optical switch, where all the signals are handled inside the optical domain.

The current popular optical switch systems are OEO switch systems. They convert optical signals to electrical ones (O/E conversion), perform switching in the electrical domain, and then translate the electrical signals back to optical ones, as shown in Figure 1-2. Figure 1-2 illustrates a multi-channel OEO switch. Examples include AOS products from Zhone-Tellium company [12] [26].

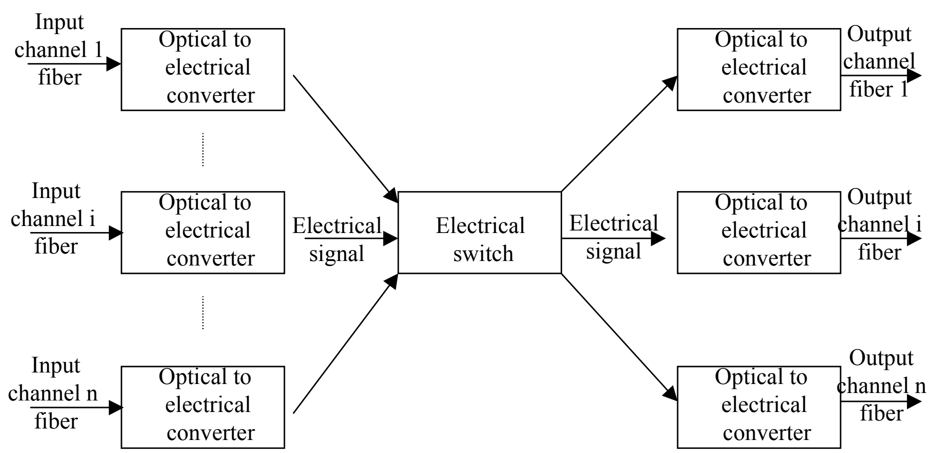

Figure 1-2 A multi-channel OEO switch

The advancement of the core electrical parts has made OEO switches dominant in the current market. By using multiple-stage structure, these OEO switches can handle thousands of switching channels according to [27]. However, because of the complexity in their signal-path translation, these OEO optical switches suffer from problems such as poor scaling to large channel count optical switches and poor performance due to the optical insertion loss involved in multi-stage structure. They also can not meet the challenges to process data rate up to 40Gb/s, which is brought about by the WDM (Wavelength Division Multiplexing) technologies.

OOO switches deal with the optical signals directly, without going through the stages to translate the signals to electrical ones and backwards, as shown in Figure 1-3. Because of using non-block light transmission in free space when switching, these OOO switches are immune to wavelength and data rate. They provide super optical performance.

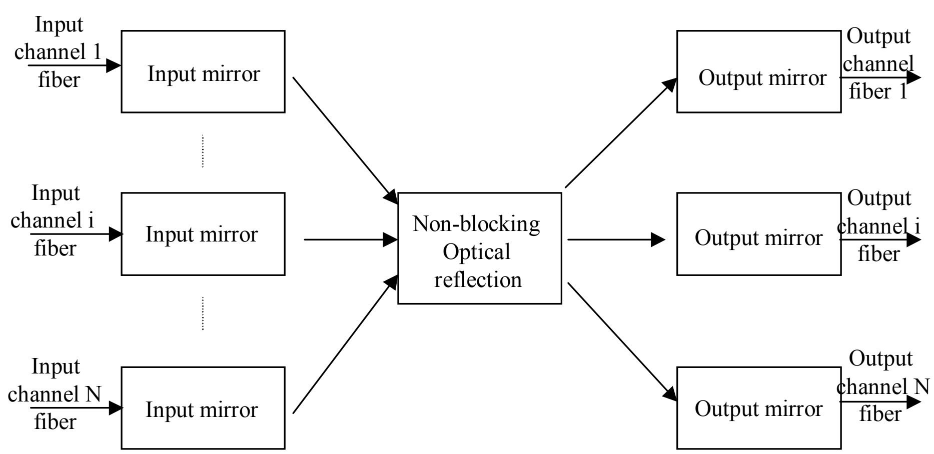

Figure 1-3 A multi-channel MEMS based optical switch

One important kind of OOO switches is MEMS based optical switch. This MEMS based optical switch distinguishes itself with super low power consumption and scalability. It is viewed as a long-term solution to the large channel count optical switch systems [12] [21]. Because it utilizes MEMS based micro mirrors to reflect the light beam, MEMS optical switch system is low in cost, easy to scale, capable to handle large channels of fibers. It also has super optical performance parameters including low optical insertion loss and cross talk [12] [13]. These features make the MEMS optical switch to be the right candidate to solve the complex problems involved in long haul telecommunication transmission.

Petersen [7] in IBM first presented the idea of using micro-mirrors to reflect light in 1980. Since then, there are continuous researches and industrial efforts on the MEMS based large channel count optical switches [8]. Especially during the optical boom in the late twentieth century, a number of companies were involved in commercializing the MEMS based optical switches. Bell Labs in Lucent Technologies first demonstrated such an optical switch based on MEMS mirrors with channel numbers more than 100 [2] [3] [28] [30] [38] [39]. Company Tellium is another company working on MEMS based optical switches [15]. Following experimental demonstration of a few hundred channels in [30], Kim et al. from Lucent presented a MEMS based optical switch with 1100 channel counts [31].

Large channel count optical switches have put special demands on the MEMS mirror actuation and control, the key to MEMS based optical switches. It requires special considerations on mirror structure, control signals and the embedded system to make successful mirror actuation.

1.2 Different actuation methods

The first step to control the MEMS mirrors successfully is to select the right kind of actuation method. Several actuation methods have been investigated to actuate the movement of these mirrors. These mainly include thermal, piezoelectric, electromagnetic and electrostatic methods [15].

1.2.1 Thermal actuation

Thermal actuation utilizes the force developed in thermal expansion. One example of thermal actuation is the thermal expansion between two different material layers with different thermal coefficients. When the temperature increases, one layer expands more than the other, resulting in thermal bending forces. Normally, thermal actuation gives large and long-range force. The required driving voltage is low and there is a linear relationship between the thermal stress and the displacement. However, this actuation method requires a lot of space and is slow in speed. It depends on the environmental temperature. It suffers low energy efficiency due to heat loss. As a result, it has pretty high power consumption [16] [17].

1.2.2 Piezoelectric actuation

In piezoelectric actuation, the applied electrical voltage makes the internal electric dipoles inside the material to realign, causing the atoms to change positions, which results in observable dimensional changes. Conversely, if a strain is applied on the material, a related voltage can be measured between the two contacts terminals. The relationship between the applied voltage and the dimensional change of the material can be expressed as [18]:

$$F = \frac{\varepsilon \cdot A}{c \cdot L} V \tag{1-1}$$

Here c is the piezoelectricity coefficient; L is the thickness of the piezoelectric film; ε is the dielectric permittivity; A is the contact area, which is perpendicular to the dimension L; F is the piezoelectricity force; V is the applied voltage across the material of length L. Figure 1-4 shows an example of a piezoelectric actuator.

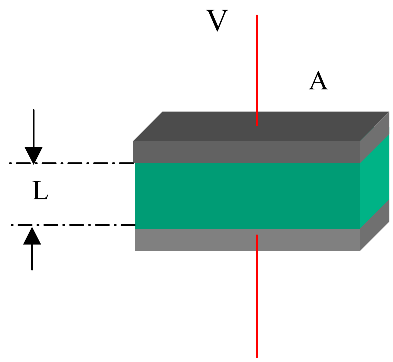

Figure 1-4 A piezoelectric actuator

The piezoelectricity force is strong, especially when thick piezoelectric films are used. In the case of thin-films less than 5μm, the actuating force is in the range of mili-Newtons. However, the movement range is very small for piezoelectric actuation. This limits its application. Another issue with piezoelectric actuation is the challenge in process integration using the current silicon technology since piezoelectric films need special material depositions [18].

1.2.3 Electromagnetic actuation

An electromagnetic force is generated when a loop with current I moves in a magnetic field $\vec{B}$. The magnetic force on the current loop is perpendicular to the magnetic field and the current. This force is expressed as

$$\vec{F} = I\oint_C d\vec{l} \times \vec{B} \tag{1-2}$$

where $\vec{F}$ is the electromagnetic force; I is the current flowing in the loop; $d\vec{l}$ is the differential vector along with the circumference of the loop; $\vec{B}$ is the vector of direction and magnitude of the magnetic field; and C is the closed loop in which the current flows. For example, if $I = 10mA$, $|\vec{B}| = 0.1Tesla$, $C = 1mm$ in length, we have:

$$\vec{F} = 10mA \cdot 1mm \cdot 0.1T = 0.01A \cdot 1 \cdot 10^{-3}\, m \cdot 0.1T = 1 \cdot 10^{-6}\, N \tag{1-3}$$

Thus we have a magnetic force in the range of several micro Newtons. For electromagnetic actuation, it features relatively high current and low driving voltage. The drawbacks for this actuation method are: 1) the low energy efficiency, so power consumption is high 2) the bulky space for the coil, 3) the difficulty to integrate with planar silicon technology [19].

1.2.4 Electrostatic actuation

Contrary to electromagnetic actuation, in electrostatic actuation, the driving voltage is high and the current is very low, ideally zero. There is no power consumption in the ideal case due to the capacitive nature of the two terminals. When there is a voltage difference between two charged parallel conductive plates, the electrostatic force established between them is [40, p128-129].

$$F = \frac{\varepsilon A V^2}{2d^2} \tag{1-4}$$

where d is the distance between the two plates; and ε is the dielectric permittivity.

Figure 1-5 An example of an electrostatic plate actuator

As an example shown in Figure 1-5, if the supplied voltage is 100V; the spacing between the two plates is 30 μm; and the area of the two plates individually is $A = 100\mu m \times 100\mu m$, the calculated electrostatic force is

$$F = \frac{\varepsilon A V^2}{2d^2} = \frac{8.86 \times 10^{-12} \times \left(\frac{100}{10^6}\right)^2 \times 100^2}{2\left(\frac{30}{10^6}\right)^2} = 4.9 \times 10^{-6} N \tag{1-5}$$

This force is also in the micro-Newtons range. One special advantage of this actuation method is its easy scalability, as this force is directly proportional to the area. Another advantage of this actuation is almost zero power consumption. These two features have made it possible for thousands of these actuators to be packaged into a single chip using the present silicon planar manufacturing processes with very little power consumption. Thus it has become the most common actuation method used to tilt the mirrors optical switch systems. The examples of using electrostatic actuation include the Lucent LambdaRouter cross-connect [3], 238x238 channel optical switches [30], and 1100x1100 optical switches [31].

1.3 Previous research work and motivation of this dissertation

1.3.1 Methods to reduce the high actuating voltage

The main drawback with the electrostatic actuation method in large channel count optical switch applications is the requirement of high actuating voltage. According to Petersen [7], an actuating voltage in the range of 100-400V is needed to drive the mirror body in the structure as shown in Figure 1-1.

This high voltage requirement has put special demands in system design, such as a special power supply design and isolation materials. To reduce this requirement, several methods have been studied. One method is to expand the electro-plates' area according to Equation (1-5), [29]. However, this negatively increases the space occupied, which is unrealistic to a large channel count optical switch with thousands of mirrors involved. Another solution is to decrease the gap between the two electro-plates. Still, there is a physical process limit for such a decrease.

An alternative method to reduce this high voltage requirement is to change the mechanical structure of the actuator. One such example is a comb driver, as shown in Figure 1-6 [22]. The actuating force in such a comb driver is expressed as [23] [24]:

$$F = \frac{N \cdot t\varepsilon}{g} V^2 \tag{1-6}$$

where N is the number of fingers in a comb; t is the thickness of the electrodes; ε is the permittivity of the medium between the gap; g is the gap distance between the fingers; and V is the applied external voltage.

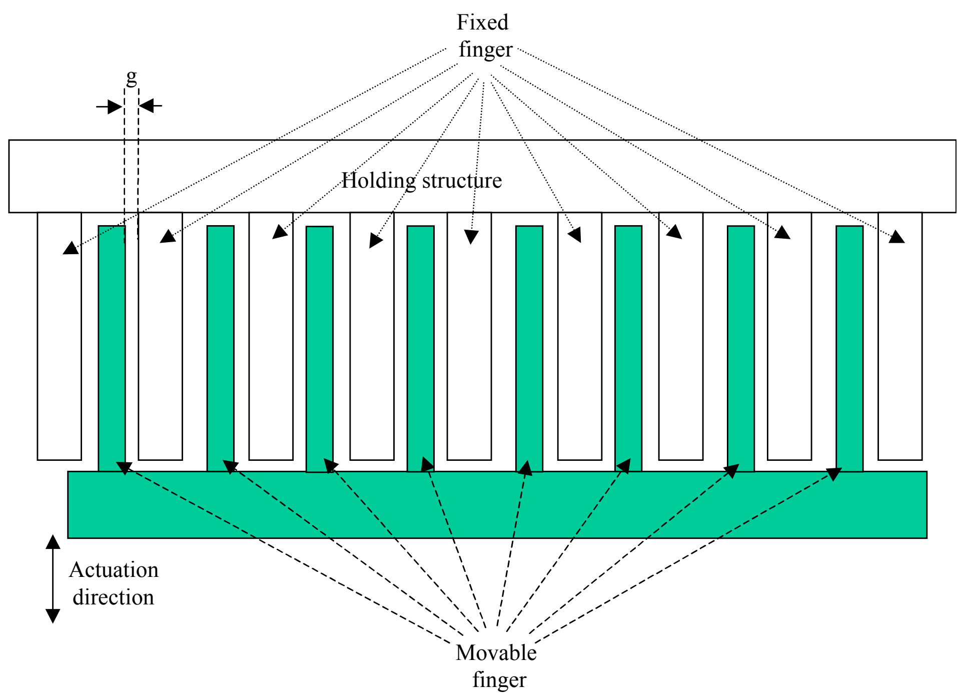

Figure 1-6 The top view of several fingers in a comb driver

By using a large number of fingers in the comb, the required actuating voltage can be reduced according to Equation (1-6) to reach the same displacement. However, this comb driver structure suffers from a large area requirement and has limitation in the force direction [23] [24]. It can provide only one force direction, not suitable to rotate a mirror as the required in the optical switch applications.

One goal of this dissertation is to present a structure to reduce the actuating voltage, which can be reasonably handled by current manufacturing and circuit design technologies. Besides the reduction of the driving voltage, another issue addressed in this dissertation is the control in MEMS mirror's actuating.

1.3.2 Control in MEMS mirror's actuating

MEMS based optical switches can not succeed without the control of MEMS mirrors during their whole life time periods. Control theory has already been applied on MEMS mirror actuation to improve its performance. For example, Maithripala [32] provided a port-controlled Hamiltonian approach to analyze the stability and control of two parallel plates. Seeger [35] and Chan [33] investigated the methods to expand the system's moving range by introducing a proper capacitor feedback. Wang [34] used proportional, integral, derivative (PID) linear feedback control to stabilize the MEMS mirror.

However, the feedback control in Maithripala [32] has limitation because it assumes that the damping coefficient is constant with no change with time, which is not true in reality. Even though Seeger [35] has successfully increased the traveling range of the top plate with a capacitor, however, the fact that a higher actuating voltage needed than the case without the capacitor can not meet our goal to reduce the actuating voltage. In this dissertation we will provide an optimal control methodology for a MEMS mirror actuator system in the large channel count optical switch applications.

In a large channel count optical switch, because a mirror is used to reflect the light beam when tilted properly, a feedback control is targeted to achieve its stability. In order to construct such a feedback control, we need to figure out a way to sense the position of the mirror in real time. One popular way to construct such detection is by using light-power detection [34] [41].

An optical tap module is used to detect the light-power density of the light beam. An optical tap is an optical component, which can extract a small portion of the light-power away from a fiber [42], and let most light-power pass through without any interruption. Based on this light-power detection method, an example of feedback control architecture is shown in Figure 1-7.

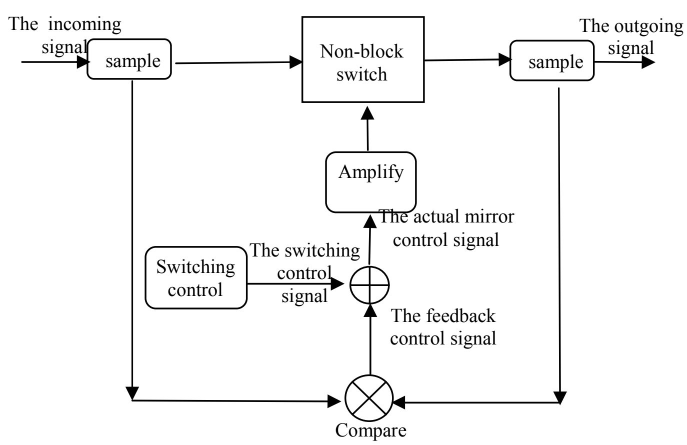

Figure 1-7 Closed loop control for a MEMS mirror actuator

This architecture is very popular to achieve the stability for a MEMS mirror in the industry [34] [41]. The incoming light signal is sampled or tapped first and then compared with the sample of the outgoing signal after the light beam is reflected. The result of this comparison is used to fine tune this mirror (by changing the actuating voltage) to the desired tilt angle to assure that the incoming light-power is the same as the outgoing light-power. In this way, a minimized overall insertion loss is achieved.

There is a problem with the above popular position sensing method based on the light-power detection. It has position limitation. Because there are physical size and location limitation on the output light-power detector, this results in a threshed position detection range for the output light beam. If the output light beam is out of this detection range, the output light detector can not detect anything. When this happens, the system does not have any information about where the output light beam goes. The feedback fails when the mirror undergoing large rotation. To solve this, we will provide a sensing capacitor along with an optimal control methodology in this dissertation.

The switching control signals, shown in Figure 1-7, from the control module normally is pretty low in value compared to what is required to actuate the mirror. An amplification circuit is needed. For the large channel count optical switch applications, this circuit should be simple so that it can be small in size and low in power consumption. In this way, the size and power consumption of the whole system can be within a reasonable range.

Also this amplification circuit should be easy to be integrated with other parts of the system, ideally, the whole system integrated on a chip. Plus, the driving voltage involved here is quite high. Normally it is up to two to three hundred volts. By using an optimal bottom-plate structure presented here, this actuating voltage can be reduced to 120V. However, this is still such a high voltage that special attention should be paid.

In response to this demand, some companies have already developed high voltage driver devices and made them commercially available. For example, there is a 16 channel high voltage driver from Agere System [41]. That device has 16 independent channels. Each channel has two independent outputs up to 295 volts. It also has 16-bit digital control signals to select the two outputs of each channel. A 1024 by 1024 optical switch in $2N$ structure needs 128 such driver devices, just for high voltage driving. This driving architecture makes the whole system very complex and contradicts the requirement of compact size for optical switches. Thus it motivates us to introduce a new simple driving circuit to overcome this complexity.

In addition, a MEMS based large channel count optical switch can be composed of a large number of mirrors. For example, in a $2N$ structure, a 1024 by 1024 optical switch has 2048 mirrors and needs 4096 analog voltages as well as 4096 bits of digital control signals. Because the repetition nature of the same driving circuits for hundreds or even thousands of mirrors, any effort to reduce the complexity of the driving control circuits can result in great benefits for the system as a whole. We will answer this call by providing simple driving-circuit architecture.

The control loop shown in Figure 1-7 belongs to an embedded system for mirrors. The embedded system, which is popularly used today for an optical switch, features a fixed number channels, targeting specific channel numbers [3] [12]. As each DAC needs a control digital bit for selection, normally, a line decoder or cascaded line decoders are used to control the DACs [36], as shown in Figure 1-8. When there is a need for an increase in the number of channels, more DACs are in needed. The microprocessor provides more control digital bits correspondingly. However, there is a limit on the number of digital control bits a microprocessor can provide.

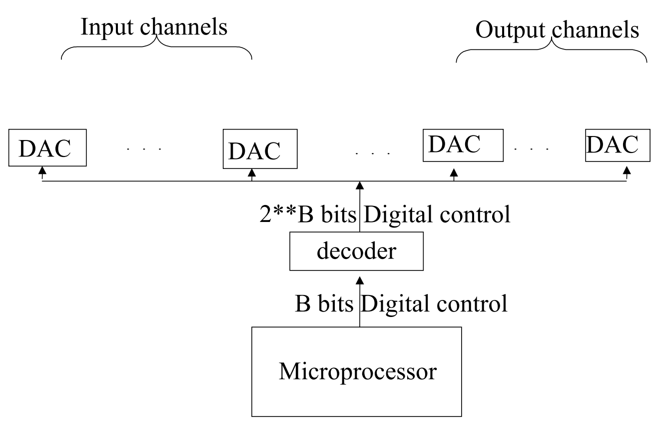

Figure 1-8 One popular embedded system using a decoder in controlling DACs

For example, B bits digital output ports from the microprocessor are needed to drive the decoder. That is the decoder has B bits input, which has 2^B bits output to drive the DACs. The DAC selection is made by keeping one of the 2^B bits high and all the others low [36]. With more DACs to be controlled as a result of an increased channel numbers in an optical switch, the required number of digital ports, B, should be increased. However, the microprocessor has a limited capability to support the required number of digital ports. And this capability will quickly be exhausted as the demand in the number of DACs to drive more channels increases.

Each time, when the need arises to increase the channel numbers by using different decoders, duplicate hardware and software are involved. However, for a large channel count optical switch, scalability is desired, which means that the system can be scaled up or down based on current system. Due to the narrow design margin in large channel count optical switch, scalability provides us the ability to reuse the system if more or less channels are needed. Thus a lot of design effort can be saved, so the system is low in cost. Further, reliability and easy maintenance can also be achieved through scalability. Our solution to obtain scalability is based on using a shift register to solve this lack of enough control bits from the microprocessor.

1.4 Overview of the dissertation

With the motivations to solve the problems and improve MEMS mirror performance in large channel count optical switch applications, this dissertation focuses on reducing the mirror actuation voltage and optimal control. An optimal mirror plate structure to minimize the required actuating voltage is introduced along with a design methodology. Its equilibrium and transient analyses are performed. Its stability is confirmed by the control theory. Its optimal control in view of the control methodology, the position sensing method, the high voltage driving circuit and the embedded system are investigated.

The outline of this dissertation is listed as the following. Chapter 1 is an introduction chapter, giving the motivation and contributions. Chapter 2 is the background review on MEMS applications to optical switches. Special attention is given to the structure of a MEMS mirror actuator in large channel count optical switch applications.

Chapter 3 discusses an optimal actuator with a tilted bottom plate structure. By presenting a design methodology, the equilibrium status of the system is analyzed. Ways to calculate the spring stiffness are given. A design example is presented on the optimal actuator with a simulation in ANSYS, which is compared with a design example using a standard horizontal plate structure.

Chapter 4 focuses on the transient responses of this presented optimal actuator. A transient response equation is set up and solved with the consideration of the squeeze damping effect. An analytic solution to the transient response is obtained from linearization of the transient equation. There is a comparison between the transient responses of optimal actuator and that of the standard horizontal plate actuator.

Chapter 5 discusses the stability and optimal control of the optimal actuator. The stability of the system is confirmed and the optimal control algorithm to improve the system performance is discussed. Architecture to implement these control methodologies with a sensing capacitor is presented. This chapter also introduces a high voltage driving circuit suitable for large channel count optical switch applications. In the last sub-section, a modular embedded system is presented. The last chapter is Chapter 6, which makes a review of the whole dissertation and points out future work.

1.5 The main contributions

In this dissertation, the research efforts are focused on reduction of the high voltage value involved in actuating a MEMS mirror and on its optimal control. A mirror actuator with an optimal plate structure is introduced. Its equilibrium analysis is performed with the development of a design methodology.

The stability of the system is confirmed by a Lyapunov function and the Routh-Hurwitz test. Two optimal control methodologies, one being bang-bang control and the other being Kalman closed loop feedback control, are discussed to improve the system performance. The feedback control architecture is investigated using a sensing capacitor in a bridge circuit. This position sensing method does not have any limitation on the position of the output light beam.

A high voltage driving circuit is given by considering a special feature in actuating two bottom-electroplates related to single-axis rotation of each mirror. A simple circuit implementation is presented, which is low in cost and power consumption and benefits the idea of the system on a chip. By introducing a shift register, a modular embedded system is presented to provide the scalability of the system, when there is need to increase the channel numbers.

The contributions of this dissertation are the following:

1. A mirror actuator with an optimal plate structure

A mirror actuator with an optimal plate structure is presented, which can reduce its voltage requirement from the industry standard one of 250V to 120V to approach the same maximum tilt angle of the mirror.

A design method of such an optimal plate actuator in large channel count optical switch applications is given. A design example is discussed, which is confirmed by ANSYS simulation. A four-level stage bottom plate is discussed as an example of a Multi-step approximation of such an optimal plate structure. By considering the squeeze film damping effect, the system's transient analysis is set up in Chapter 4. This transient response is obtained by PSpice simulation from its analogous electrical circuit.

2. Optimal control on the mirror actuator

Feedback control architecture is presented in Chapter 5. Two optimal control methodologies can be used in such architecture. One methodology is bang-bang control to achieve minimum switching time. The other methodology is the Kalman closed loop control to achieve the stability of the mirror. The position sensing is accomplished by is a sensing bridge with a sensing capacitor in this architecture. This sensing method can detect any position of the mirror without any limitation. A variable resistor made from a MOSFET is used to balance this sensing capacitor inside the bridge.

A new high voltage driving circuit architecture is introduced. Featuring very simple architecture, this circuit saves resources significantly in large channel count optical switch applications. It reduces by one-half the number of the required actuating voltages and eliminates the digital control bit, which is used to distinguish between the two bottom electroplates associated with single-axis rotation of the mirror. A bipolar transistor implementation of such architecture is presented with design analysis. Further this high voltage driving circuit benefits the idea of the system on a chip design, which answers the call of the trend of integrating electronic circuits with MEMS components.

By using a shift register, modular embedded system architecture is presented to achieve the scalability of the system in the requirement of more channel counts. This benefits cost reduction, design simplification and future maintainability.

Chapter 2: Background

Abstract

In this chapter, we first give a brief review on optical switches including their functions and available technologies. Specifically we review the architecture of MEMS based optical switches. We then explain the structure of an electrostatic actuated MEMS mirror actuator, as well as its operation mechanism and system considerations.

2.1 Concept of an optical switch

Before giving the analysis of an optimal plate actuator as well as its control and driving circuits, a review of the optical switch concept including its system architecture and available technologies is beneficial to understand the requirements for such a plate actuator. Also a review of the structure of an electrostatic actuated MEMS mirror actuator and its operating mechanism is necessary to understand the problems and their solutions outlined in this dissertation. This chapter serves as foundations for the later chapters.

With the growth in network capacity as a result of WDM and IP technology, optical switches have become important components in layered networks. The functions of an optical switch include restoring connections and provisioning new connections in a layered network. In case of a connection failure, an optical switch should have the ability to reconnect the failed connection in reasonable time. In case of network system load rescheduling, an optical switch should provide the new connections in the required time frame without interruption of any other connections [26], [57].

Several optical switch technologies have been investigated in recent years, which mainly are categorized into two types, free space switches and waveguide switches depending on how the optical signal propagates [26].

Waveguide switches can be based on optical interference, total internal reflection [51], thermo-optic effects and electro-optic effects. An Agilent lab has investigated a bubble actuated total internal reflection optical switch, which has a very fast switching time of 100μs. [52] [53]. A NTT lab has worked on a silica-based thermo-optic switch, which is very easy to make fiber attachment [54]. By using electro-optic effects, the electro-optical switch has fast switching speed [55] [56] [57]. However, these waveguide optical switches suffer from very poor scalability and high power consumption [26] [57]. These have made them poor candidates for the large channel count optical switch applications.

In the free-space switch category, there are MEMS switches and liquid crystal switches. A liquid crystal switch is based on controlling the polarization of the light by an electro-optic effect inside the liquid crystal. It has constant insertion loss when the channel count increases. However, it is poor for scalability [26], [57].

A MEMS based optical switch belongs to the class of free space switches. This technology has distinguished itself over other technologies for its scalability and low power consumption, most suitable for the demands in the large channel count optical switch applications [26] [51] [52] [53] [57]. Because of free-space traveling of the light beam, this kind of optical switch has very low insertion loss, low cross-talk between signals and is transparent to signal data rate, protocol, wavelength and polarization. Though its switching time is not that fast among all the optical switches, this switching time is still within a reasonable range for large channel count optical switch applications [2][3][12][13][21][57][58]. More details about the architecture of the MEMS based optical switches will be given in the following sections.

2.2. Architecture of MEMS based optical switches

An $N_1 \times N_2$ optical switch means that there are N_1 input channel fibers and N_2 output channel fibers in the system. Normally, $N_1 = N_2 = N$. There are two kinds of architectures for MEMS based optical switch systems. One is the N^2 architecture, also called two dimensional. The other is the $2N$ architecture, also called three dimensional [21] [26] [28].

In the N^2 structure, the light beam always resides in the same plane before and after the reflection (from which the name two-dimensional comes). The position of the micro-mirror has only two states, namely, up or down. When one mirror is in the up state, directing the light beam signal from the input fiber to the output, all the other mirrors are in the down state, as shown in Figure 2-1.

As each mirror only involves two states, its driving voltage and circuits are quite simple and straightforward. However, the price for this simplicity is the potential optical loss for the traveling beams when a large number of mirrors are involved.

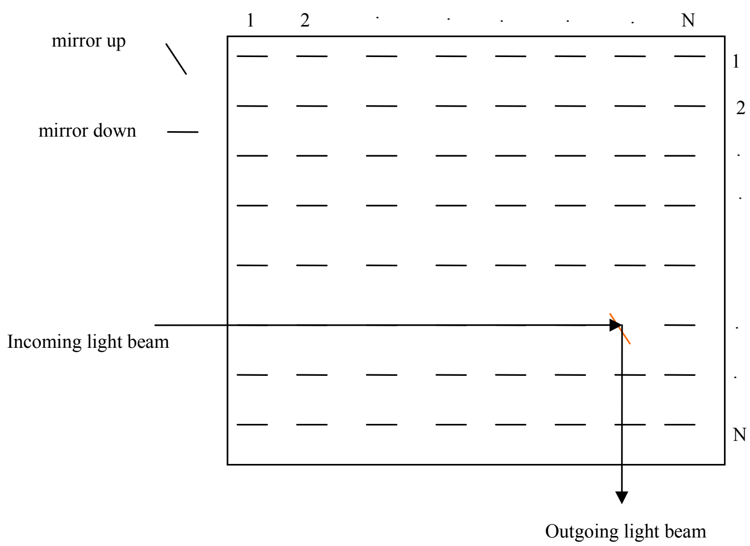

Figure 2-1 The optical path in N^2 architecture

For a $N \times N$ switch, the required number of mirrors is N^2 in this N^2 structure. This is not a big number if N is small, and the insertion loss might be tolerable in terms of system requirements. However, the mirror numbers increase quadratically when more channels are needed, making this approach uneconomical for large channel counts. At the same time due to the optical path increase with the increasing channel number, the insertion loss becomes intolerable for the system requirement [12]. The maximum N is 32 limited by the light beam diffraction loss [29].

In conclusion, the N^2 architecture is preferable for small optical switch systems because of its simple control. It is not a good choice for large channel count optical switches when $N > 32$.

In the $2N$ architecture, the light beam can travel in three-dimensional space before and after it is being reflected. There are two mirror arrays. One is an input mirror array and the other is an output mirror array. Schematics of these two arrays are shown in Figure 2-2. The mirror array can be one $1 \times N$ array as shown in Figure 2-2 (a); or it can take a matrix format, as shown in Figure 2-2 (b), with I columns and J rows ($N = I \cdot J$) [3].

For a $N \times N$ switch, the required number of mirrors is $2N$. Instead of availability of two positions in the N^2 architecture, each mirror in the $2N$ architecture can occupy one of N positions. Figure 2-2 (b) shows a complete optical path in the $2N$ architecture, including the optical input lens arrays and output lens arrays.

The optical path length in the $2N$ structure is proportional to the square root of N , while the optical path length in the N^2 architecture is proportional to N . Correspondingly, with the same N , the light beam travels a longer distance in the N^2 configuration compared to the case in the $2N$ architecture. This results in much better optical performance when N is a large number for the $2N$ architecture than for the N^2 architecture.

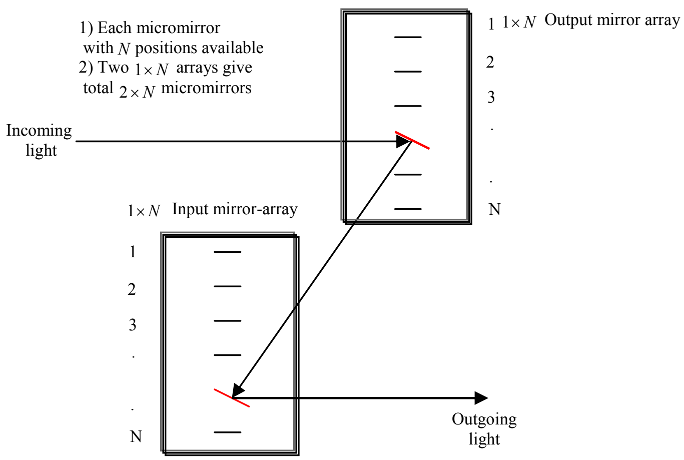

(a) $1\times N$ mirror arrays

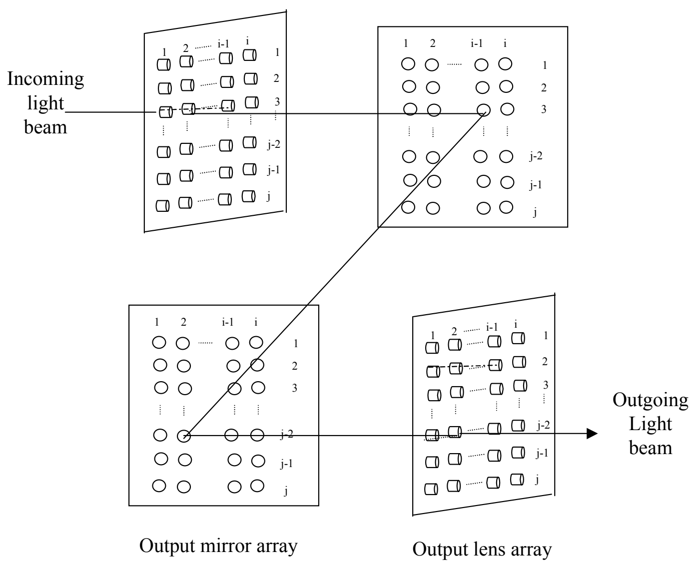

(b) $I\times J$ input and out mirror matrix

Figure 2-2 The optical path in $2N$ architecture

For large channel count optical switch systems, usually when N is larger than 32, the $2N$ architecture is preferred. Unfortunately, as the position of the mirror needs to have N states, the $2N$ architecture achieves this super optical performance at the expense of complexity in controlling these mirrors [21]. Usually this involves high voltage control when the electrostatic actuation is used, as outlined in Chapter 1.

Since we investigate the MEMS in large channel count optical switch applications, where N is much greater than 32, in the following of this dissertation, all our discussion will be based on the 2N architecture except what is explicitly mentioned.

2.3 The electrostatic actuated MEMS mirror system

Having introduced the architecture of the MEMS based optical switches, we will study the MEMS mirror actuator system's physical structure and find out how these mirrors can perform their switching functions. Here we will review a popular MEMS structure for large channel count optical switch applications [29].

2.3.1 The optical path in the 2N architecture

Before reviewing a common structure of an electrostatic actuated MEMS mirror actuator systems in the $2N$ architecture, let us take a close look at the optical path shown in Figure 2-2 (b). The incoming light beam, from one input channel fiber, is first collimated by a prepossessing input lens and then travels in free space to hit one of the N input mirrors in the input mirror array. In turn, the reflected beam hits one of the N MEMS output mirrors in the output mirror array, where it is redirected to the corresponding output lens, then it goes out of the output channel fiber.

For example, let us study the switching process when there is a command to switch the light beam from the input fiber k to the output fiber. The input channel k and the output channel j will be selected and their related voltage control circuits will apply the corresponding voltage to tilt the input mirror k and output mirror j individually to some desired tilt angle. In this way, first the input light beam is reflected by the input mirror k. Then it is again reflected by the output mirror j. Thus it is switched from the input fiber k to the output fiber j.

By tilting the input mirror in three dimensions and the corresponding output mirror, the input light beam from any one input channel can be reflected to any one of the output channels as desired. Here, single-axis rotation can be used to tilt the mirror when the mirror arrays are aligned as in Figure 2-2(a). Two-axis rotation can be used when the mirror arrays are aligned as in Figure 2-2(b).

2.3.2 The structure of an electrostatic actuated MEMS mirror with one rotation axis

A single-axis mirror actuator structure is shown in Figure 2-3 [7]. A two-axis mirror actuator structure is shown in Figure 2-4. The research in this dissertation is mainly based on a single-axis mirror structure. The same methodology and similar results are held to the two-axis structure.

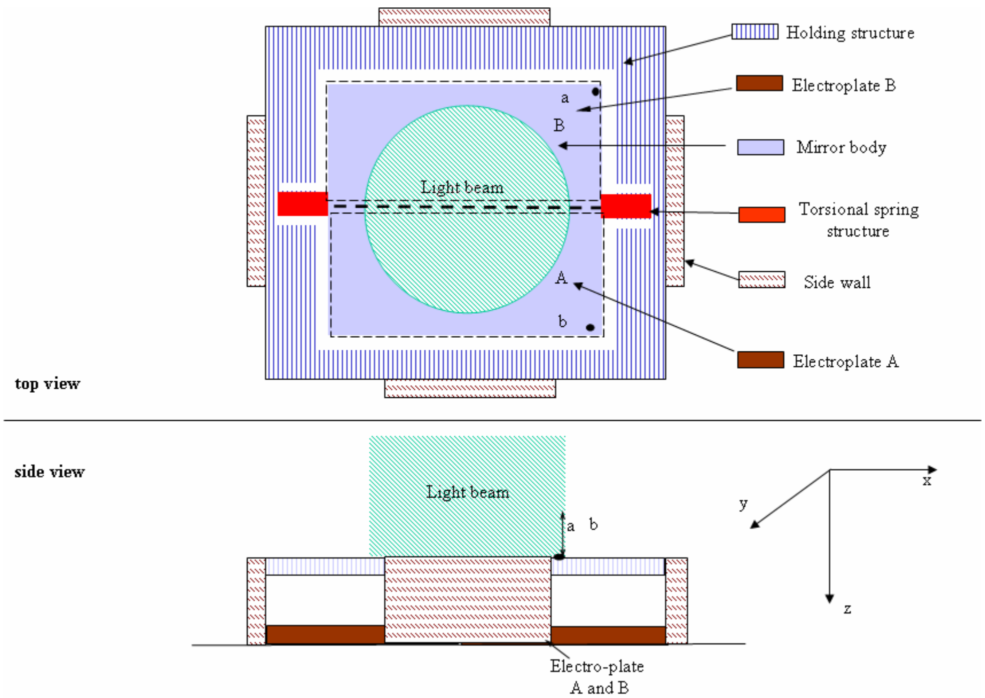

Figure 2-3 The structure of a MEMS mirror with one rotation axis

As shown in Figure 2-3, the mirror and its holding structure are made of the same material and originally they are one part. The mirror is etched out from this holding structure. This holding structure again is held by the four side walls. Two torsion springs are attached to the two ends of the mirror separately. There are two bottom plates (labeled A and B) under the mirror, which are electro-isolated from each other.

The top surface of the mirror body is flat with high reflective index, used to reflect the light beam. The edge points are labeled ‘a’ and ‘b’.

A parallel plate actuator is formed between the mirror body, and one of the two bottom electro-plates. When there is a voltage difference between one of the bottom plates and the mirror, the mirror tilts. For example, there is a potential difference between the mirror and Bottom-plate A, then the edge point labeled ‘a’ on the mirror will move toward this Bottom-plate A. In this way, the mirror will reach an angle of α to the horizontal line when it is in equilibrium status. Here we will assume that the whole mirror structure is symmetric along the rotation axis.

2.3.3 The structure of an electrostatic actuated MEMS mirror with two rotation axes

Figure 2-4 presents a schematic view of the four bottom-electroplate structure for an electrostatic actuated MEMS mirror system according to Aksyuk [29]. This is also a popular mirror structure in the $2N$ structure [22]. It consists of a mirror body, four bottom electro-plates A, B, C, D (fixed in position), and additional suspension structures of a gimbal mount.

This gimbal mount has two frames. The inner frame is movable, while the outer frame is fixed. The mirror body is suspended by two torsional springs inside the inner frame in the X direction. This frame is suspended by another two torsional springs in the Y direction inside the fixed outer frame. Additionally, the outer fixed frame is held in position by four holding sidewalls, (right and left, up and down).

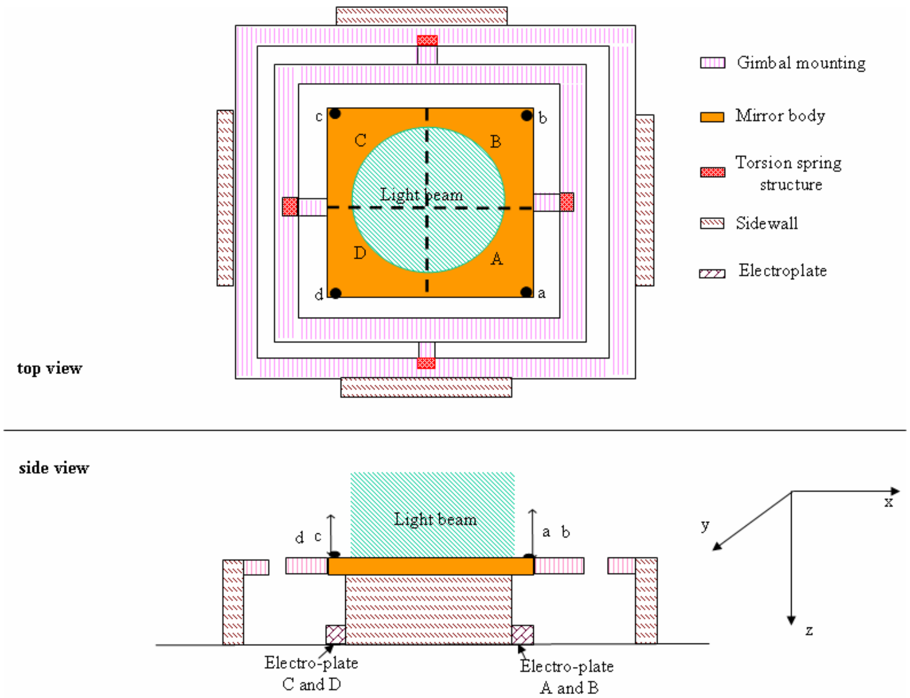

Figure 2-4 The schematic of a two-axis structure of a MEMS mirror system

The four electro-isolated bottom electro-plates are just underneath the mirror body. These four bottom electro-plates, labeled A, B, C, and D in Figure 2-4 and Figure 2-5, are electrically isolated. They are used to actuate two-axis tilting. The electrostatic torque can tilt the mirror in three-dimensions to allow the four edge points labeled 'a', 'b', 'c','d' on the mirror to move up and down, as shown in Figure 2-5. Here, we assume that the suspension structures make the mirror body perfectly symmetrical in the right-left and in the up-down directions. Here again the whole mirror structure is assumed to be symmetric along its two-axis.

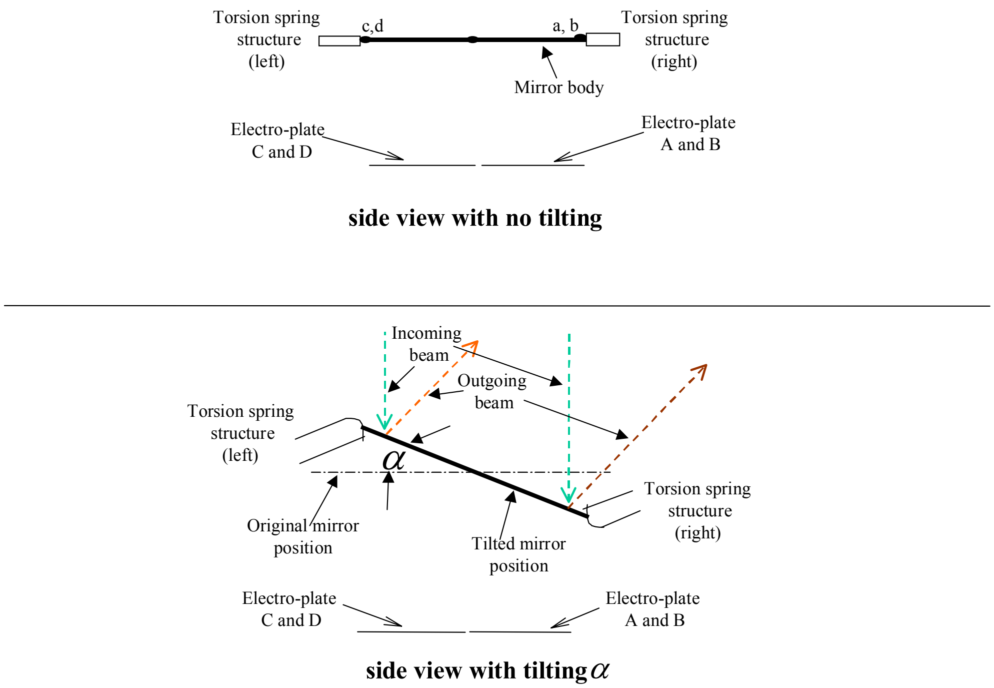

Figure 2-5 A side view of the mirror structure with and without tilting

2.3.4 Restrictions to actuate a MEMS mirror actuator

In fact, the mirror actuation is solely dependent on the relative voltage difference between the mirror body (top electro-plate) and the bottom electro-plate. Therefore, the sign of the external voltage applied does not really matter. This gives us great freedom in actual analog high voltage control circuit design when this principle is implemented. We will see that in Chapter 5.

So far, we have observed that each bottom electro-plate can be treated as an analog component individually in the view of circuit control. Each of them needs to be controlled accurately to redirect the light beam.

To reach a tilt angle, in the case of a single-axis rotation, the two bottom plates can not be actuated simultaneously. In the case of a two-axis rotation, one bottom plate can be actuated or *only* two adjacent bottom electro-plates out of the four can to be actuated at the same time. Other cases to actuate the bottom plates are forbidden in order to void bending the mirror. For example the two diagonally located bottom plates can not be actuated simultaneously. Another example is that three of the four bottom plates can not be actuated. These rules will result in a unique driving circuit architecture, which will be covered in more detail in Chapter 5.

2.4 Process of light beam switching and its maximum tilt angle requirement

A review on the light beam switching process inside the MEMS based optical switch will be helpful to study the control on the MEMS mirror actuator system. As discussed in the previous sections, the light beam path is shown in Figure 2-2 and redrawn in Figure 2-6. In a $N \times N$ MEMS optical switch, by actuating both input mirror and the output mirror correspondingly, the input light beam from one channel can be routed to any one of the output channels as needed, which is the process of "switching". To accomplish this, one applied voltage is needed to control one rotation-axis motion of each mirror.

Normally, the mirror is applied a fixed electrical potential. The bottom-electroplates are fixed in position with external variable voltage applied. In order to control the angular position of the mirror, a desired actuated voltage is applied on the corresponding bottom-plate. When there is a potential difference between the mirror body and the fixed bottom-electroplate, the actuating electrostatic torque is generated on the mirror. When the bottom plate and the mirror have the same potential, there is no actuating on the mirror. The suspensions hold the mirror body (or called mirror plate), and provide the spring torque on the mirror to balance the actuated electrostatic torque in equilibrium.

The maximum tilt angle needed to reflect the incoming beam to the farthest output fiber position is shown in Figure 2-6. As shown in Figure 2-6, every mirror needs to be able to tilt a variable angle α to redirect the beam from any input to any output fiber. The mirror tilts the maximum angle $\alpha_{\max}$ when it redirects light beam from the input channel number 1 to the farthest output channel number N.

The maximum title angle will determines the maximum channel count N and itself is determined by the actuation torque, normally is less than ±10 degree [26][29] [73]. The tilt angle along with the mirror size will determine the effective light beam size and eventually influence the optical performance, such as optical loss and crosstalk. Normally the mirror has a size around several hundreds of micrometers.

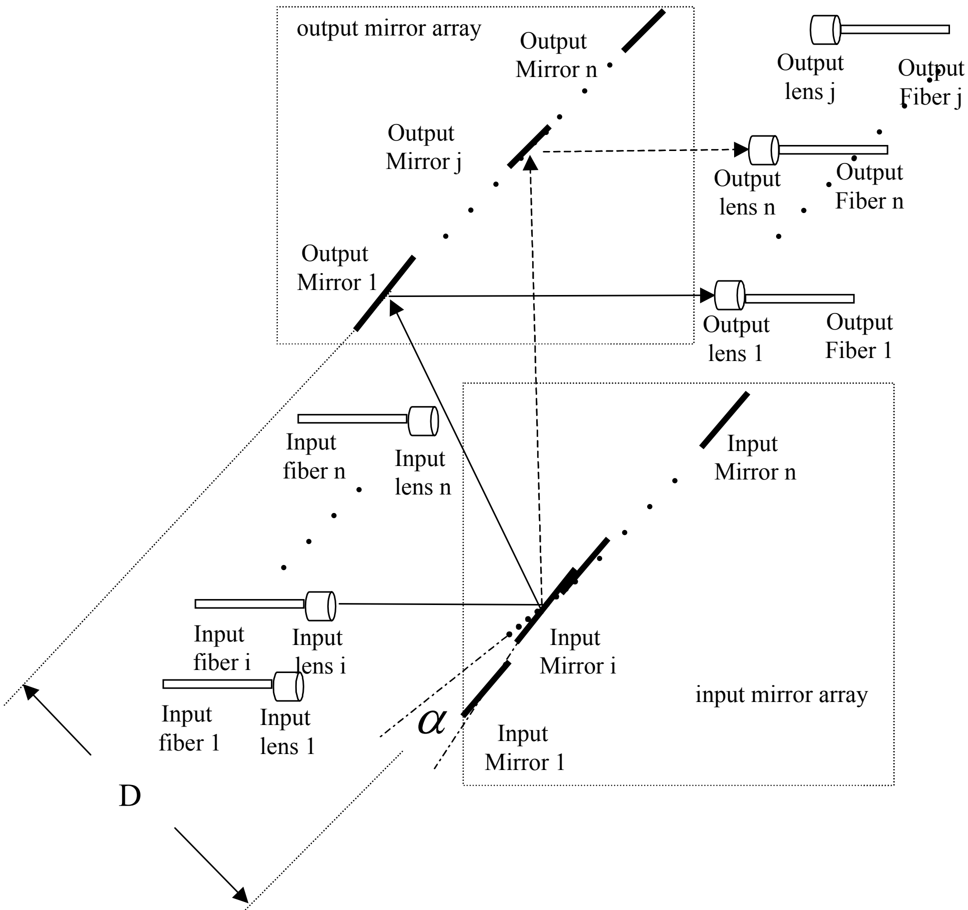

Figure 2-6 The maximum mirror tilt angle determination criteria

Although the required mirror tilt angle α and α_{max} can be reduced by increasing beam travel distance D, the parameter D is normally limited by the working distance of other optical components and/or system requirements, such as working distance of the collimating lenses and overall system size, etc.

2.5 The embedded system for MEMS actuators

From the switching process described above, we can tell that a MEMS mirror actuator demands its embedded system to have the following control abilities: 1) be able to switch the mirror from one angular position to another as soon as a switching command is received. The mirror position can be one out of the N multiple available positions to accommodate the large channel count requirement. 2) be able to hold at that specific angular position after this switching command before the next switching command is received. Based on these considerations, there are several points to be observed.

First, the architecture of the optical switch should be in 3D instead of 2D, as discussed in the previous sections. Because the mirror has to be able to locate in multiple positions instead of only two positions [9]. This requires a complex control circuits to drive the mirror. A carefully selected control methodology needs to control the mirror accurately and instantly. The insertion loss of the optical switch is quite sensitive to the stability of the mirror. Thus a closed loop feedback control algorithm is necessary when any perturbation appears. The hardware control heart is the microprocessor or FPGA.

Second, digital to analog converters (DACs) are used. This is because the microprocessor handles digital numbers internally. Inside the microprocessor, the feedback position information and other control signals are processed digitally according to the control methodology used. These DACs convert the digital values out of the microprocessor into analog values to actuate the mirrors.

Third, as the mirror actuator is composed of a two charged plate, an analog voltage with continuous value is needed to drive them. Because the computer can only output digital voltages in low values (normally less than 5V), accordingly, an amplification circuit is needed to amplify these low values to the required voltage level (more than 100V). Due to the repetition of the mirror structure in large channel count optical switch applications, large number of amplification circuits and DACs are in use.

It takes a lot of design efforts to have a successful MEMS based optical switch, and even greater effort to maintain it in the future. Thus we want the embedded system to have scalability, so that more modules can be added on to the present system when more channel number requirement comes. Scalability is one of the goals for the embedded system.

2.6 Objectives for MEMS mirror control

From the above illustration, MEMS actuators benefit the optical switch system in optical performance due to the nature of free space light beam traveling during switching. In order to make MEMS mirror actuator to be successful, the actuator system should achieve two objectives basically. One is that the mirror should be tilted to the desired angular position after it receives a switch command from the system. The other objective is that the mirror should be staying in the required angular position before the next switch command is received. This time period can be as short as several seconds or as long as twenty years. The system should provide super-optical performance with little optical degradation to the reflected light beam during this time interval [26].

To fulfill the task of switching function, the MEMS mirror system needs to have the ability to address the input and output mirrors of each channel individually and to control their tilting in a reasonable switching time. This translates to requirements on the MEMS mirror as parameters such as maximum tilt angle, mirror size, reflectivity and power dissipation, which contain both electrical and mechanical parameters.

2.7 Other design considerations for MEMS mirror actuators

In addition to the optimal mirror structure and its optimal control we focus on, to make the mirror perform its function, there are many considerations and trade-offs in the system design. These considerations can be on the mechanical ones, optical ones as well as electrical ones. In this dissertation, we will mainly answer the questions such as how to reduce the high driving voltage and how to control the mirror.

We have discussed the structure of MEMS mirror actuator system along with its switching requirement, the maximum tilt angle requirement and the embedded system requirement. We will briefly discuss some other related design considerations. The mirror length L_M and the required tilt angle α are determined by applications. L_M must be larger than the size of the light beam to be reflected.

The reflectivity of the mirror will impact the optical parameters such as optical insertion loss. A metal (such as gold) deposited surface is used to achieve the required reflectivity [26] [29]. Low heat dissipation is also necessary in a large mirror array.

2.8 Summary

We have briefly reviewed the concept of optical switches, with focus on MEMS based optical switches. We have reviewed the requirements of mirror structure, control, driving circuit and embedded system in large channel count optical switch applications.

To analyze and design the MEMS mirror system, the mirror body and bottom electro-plates can be treated as conductive plates [26]. The mirror body with the suspension torsional springs can be treated as a spring–mass system [7], where the spring stiffness is characterized by a spring constant k. Keeping these models in mind, we will begin our discussion on the optimal electrostatic actuated MEMS plates.

Chapter 3: An Optimal Plate Actuator Design

Abstract

In this chapter, a design methodology of a plate actuator optimized for minimal actuation voltage is developed, along with the analysis of three different plate actuator structures. The electrostatic parallel plate actuator structure and its pull-in phenomena are reviewed first. Then the performance of an optimal tilted bottom plate actuator is analyzed and compared with the traditional horizontal bottom plate actuator. A design example is presented and simulated using the ANSYS simulation tool. Based on these, a methodology for multi-step approximation to the optimal plate actuator is developed after a brief review of characteristic MEMS mirror system requirements.

3.1 Introduction

As described in Chapter 1, among the different MEMS actuators, electrostatic actuation is the most suitable candidate for large channel count optical switch applications because of its super-low power consumption, small size, and scalability. In this chapter, three kinds configuration of electrostatic plate actuators are discussed, including one with both plates paralleling each other, one with a fixed horizontal bottom plate with the top plate tilting and the third one with both bottom and top plates tilting.

A design methodology is presented along with the force and torque analyses applied to these three cases. The conclusion is that the configuration with a tilted bottom plate is the optimal one in terms of the lowest voltage requirement. Then a design is illustrated by a simple example with a confirmation from an ANSYS simulation. Next, we apply this methodology to an optimal plate actuator as an optical MEMS mirror actuator system. The special characteristics of an optical MEMS mirror actuator system are reviewed and an actuator design meeting the three dimensional tilting requirement is developed. Based on a planar fabrication process, this design implementation uses multi-step approximation to this optimal tilted bottom plate. Its ANSYS simulation results are also presented.

In principle, a simple electrostatic plate actuator is a system consisting of two parallel plates, one fixed at the bottom and one movable at the top. The movable plate is suspended by a spring with a spring constant k. When an actuation voltage V is applied across the two parallel plates, an electrostatic force is generated to move the movable plate toward the fixed plate while the spring is extended. The equilibrium status is reached when the electrostatic force equals the spring force. The movable plate then stops moving and the system is balanced. This status is called actuated. The principle of an electrostatic actuator is illustrated in Figure 3-1.

Assume: 1) the area of both plates is A; 2) the downward movement amount of the movable top plate around equilibrium at H is y; 3) the permittivity of the homogenous medium between the plates is ε; 4) neglecting fringe effect [44], [20], which is reasonable when the size of the plates is much bigger than the gap distance;

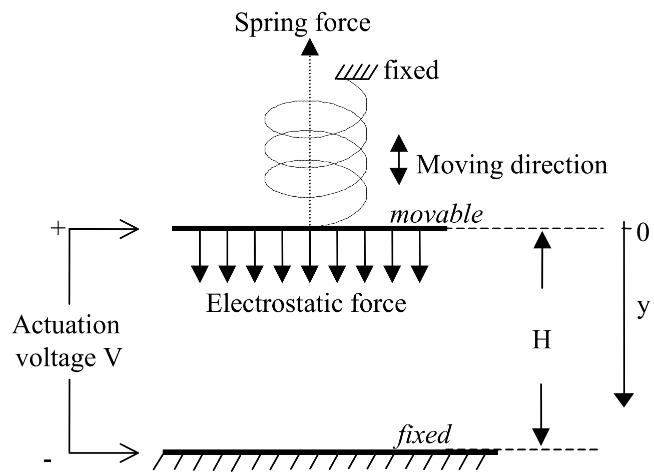

Figure 3-1 The principle of an electrostatic plate actuator

The upward force from the spring is

$$F_{spring} = k \cdot y \tag{3-1}$$

The downward force from the electrostatic force is the following.

$$F_{static} = \frac{\varepsilon \cdot A \cdot V^2}{2 \cdot (H - y)^2} \tag{3-2}$$

In the dimensions of micrometers, as what is being discussed in this dissertation, the force due to gravity is very small and it is ignored. When the system is balanced in equilibrium, the spring force and the electrostatic force are the same in value and opposite in direction. That is

$$F_{spring} = F_{static} \tag{3-3}$$

Substitute (3-1) and (3-2) into (3-3), we get:

$$k \cdot y = \frac{\varepsilon \cdot A \cdot V^2}{2 \cdot (H - y)^2} \tag{3-4}$$

Or

$$y \cdot (H - y)^2 = \frac{\varepsilon \cdot A \cdot V^2}{2 \cdot k} \tag{3-5}$$

In practical systems, among the system parameters in (3-5), the spring constant k can be adjusted since it is determined by the spring structure and the material used. If a desired spring constant k is needed, it can be achieved by choosing a suitable material and the mechanical parameters, such as the spring shape, size and number of turns used, etc. In order to reach the same amount of the top plate movement, the larger the k value is, the higher the actuation voltage that will be needed; the larger the area of the actuator A is, the larger electrostatic force will be and the desired actuation voltage will be smaller.

But this parameter will be limited by the overall system size and at the same time determined by the functions of the system. For example, the top plate size will be determined by the beam size if it is used to reflect or block a light beam. Gap distance H is the initial gap distance between the two plates. It must be large enough to allow enough space for the movable plate to move in order to accomplish desired system functions, for example, to block or reflect a light beam. In order to achieve the same amount of movement, from Equation (3-5), it can be seen that the larger the H is, the higher the actuation voltage will be needed.

What a system designer needs to do is to make a best design so that all the system requirements are met and the lowest possible actuation voltage is achieved. Very often, the actuation voltage V can go as high as several hundred volts. This brings a lot of problems, including driving circuit design, dielectric material selection and special power supply design, etc.

One of the main goals of this research is to develop a method to design a plate actuator structure with which the maximum possible displacement can be reached with a minimum voltage possible. Because the top plate needs to be horizontal and movable to redirect the light beam in the optical switch, the main focus will be on the bottom plate, which is fixed in position. This means that our goal is to find the optimal bottom plate to meet the minimum voltage required.

3.2 A plate actuator with two parallel plates

In Equation (3-5), for any given constant actuation voltage V, the maximum obtainable equilibrium movement of the movable plate can be calculated by taking the first order derivative with respect to y on both sides of (3-5) and let $\frac{dV}{dy} = 0$. We get:

$$(H - y)^2 + 2 \cdot y \cdot (H - y) \cdot (-1) = 0 \tag{3-6}$$

Or

$$(H - y)(H - y - 2 \cdot y) = 0 \tag{3-7}$$

The solutions to (3-7) are $y = H$ and $y = \frac{H}{3}$. When $y = H$, it means that the top plate and the bottom plate occupy the same y position, which results in the system collapse with no physical meaning. This solution needs to be neglected. Then we have the solution to (3-6) is

$$y = \frac{H}{3} \tag{3-8}$$

By substituting (3-8) into (3-5) we get

$$V_{pull-in} = (H - y) \cdot \sqrt{\frac{2 \cdot k \cdot y}{\varepsilon \cdot A}}\Bigg|_{y=\frac{H}{3}} = \frac{2}{3} \cdot H \cdot \sqrt{\frac{2 \cdot k \cdot H}{3 \cdot \varepsilon \cdot A}} \tag{3-9}$$

The voltage corresponding to (3-8) is called the pull-in voltage $V_{pull-in}$, meaning that the actuation voltage can not increase beyond $V_{pull-in}$. If the actuation voltage is greater than $V_{pull-in}$, the movable plate with the initial gap distance of H will snap toward the fixed plate and the system collapses. When that happens, the top plate fails to perform its function such as to redirect a light beam in our case. The range $y > H$ has no physical meaning, as the bottom plate serves as a stopper to the top plate.

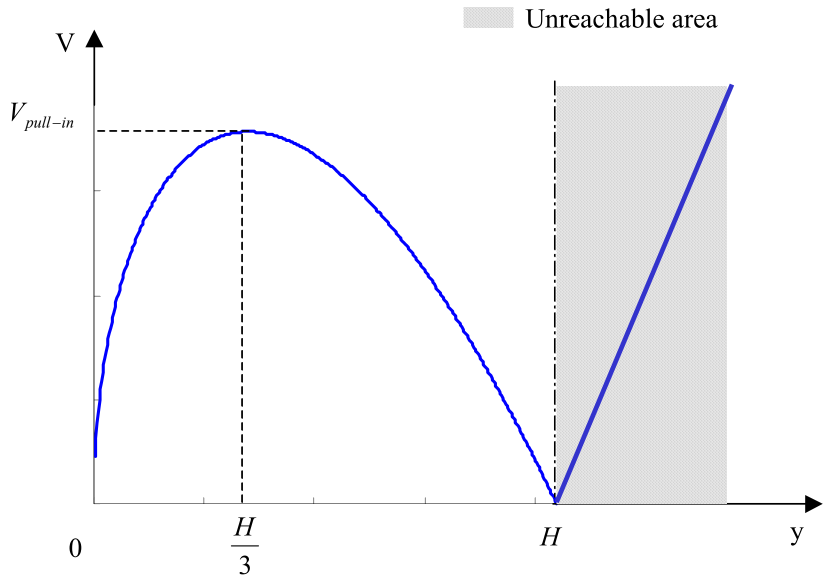

Figure 3-2 The relationship between the top plate moving distance and its actuating voltage

According to (3-5), the relationship between the displacement of the top plate and the actuation voltage applied is shown in Figure 3-2. From Figure 3-2, we can notice that in the range $0 \le y \le \frac{H}{3}$, the voltage has a maximum point at $y = \frac{H}{3}$. Beyond this point, the actuator system is unstable. It can also be observed from Figure 3-2 that the displacement of the top plate is first increased with the increase of the actuation voltage applied within the range $0 < y < \frac{H}{3}$. When the actuation voltage reaches $V_{pull-in}$, the movable plate has reached a critical point, where $y = \frac{H}{3}$. Then the distance y increases in an unstable manner during range $\frac{H}{3} > y > H$ until the top plate hits the bottom plate where $y = H$. This is the pull-in phenomenon.

Comment: v_x_plot.m

Therefore, the maximum displacement of the top plate in the equilibrium status can not exceed one third of the original gap width H, and this value has nothing to do with other system parameters, such as the spring constant k, and the plate size A, etc. However, from (3-9), $V_{pull-in}$ is dependant on these parameters. Specially, we observe that $V_{pull-in}$ is a monotonic function of H. So in order to reduce the actuation voltage needed, we need to reduce H. However, the reduction of H is limited by the pull-in point $y = \frac{H}{3}$, which determines the maximum range of displacement of the top plate. Therefore, the parallel plate actuator design procedure will be the following: based on the application, we need to decide how much displacement the movable top plate needs to have. It can be denoted as y_0. Then the initial gap distance between the two actuator plates will be $H = 3 \cdot y_0$. This system will have the lowest actuating voltage as expressed by

$$V = \frac{2}{3}\sqrt{\frac{2k}{3\varepsilon \cdot A}} \cdot \sqrt{H^3} = \sqrt{\frac{k}{\varepsilon \cdot A}} \cdot (2 \cdot y_0)^{\frac{3}{2}} \qquad (3\text{-}10)$$

In a practical design, some safety margin is needed to the theoretical value $H = 3 \cdot y_0$. It is not only because we need some design tolerance, but also because of a desired controllability. From Figure 3-2 we observe that in the region where V is close to $V_{pull-in}$, the curve is very horizontal. That means a very small voltage change will cause a relatively large change in y. This makes the y displacement very sensitive to a very small voltage change, including the noise related to the control voltage signal. Thus for this controllability reason, we want to move our system working region to some region where the V-y curve is not that horizontal; that is to the region where $0 \le y < \frac{H}{3}$.

3.3 A plate actuator with a tilting top plate and a horizontal bottom plate

3.3.1 Torque analysis

Now, we expand our plate actuator concept in Section 3.1 further to the case similar to MEMS mirror actuator system. In a tilting mirror system, the movable top plate in Figure 3-1 is replaced by a rotational top plate, which is fixed at one end, freely tilting at the other end. At the fixed end, there is a torsion spring providing spring torque. Such a tilting top plate actuator system is shown in Figure 3-3.

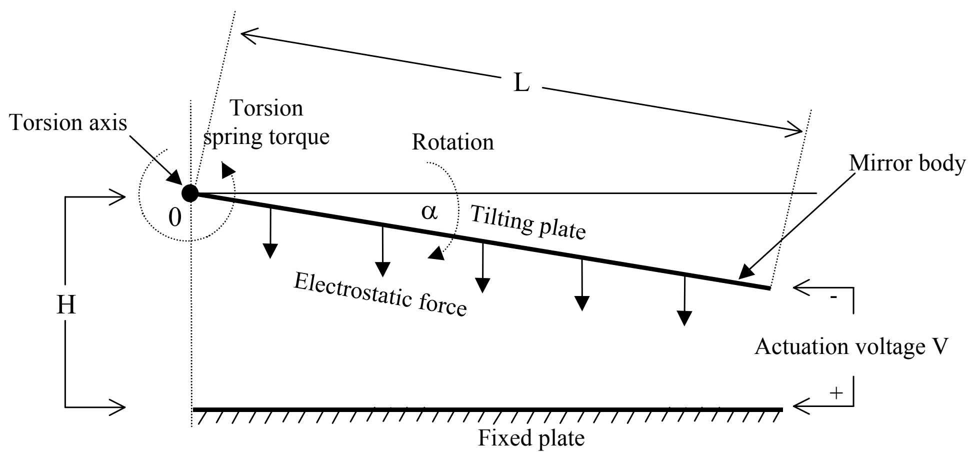

Figure 3-3 The plate actuator system with a tilting top plate

Assume: 1) the area of both plates is A, $A = W \cdot L$ with width W and length L. 2) one plate is on top of the other initially, with initial gap distance of H; 3) the tilting top plate is fixed at point 0 and is attached to a torsion spring at 0. When the actuating voltage is applied, the tilting top plate can rotate by angle α around the axis passing through point 0; 4) $0 \le \alpha \le \alpha_M$, where α_M is the maximum tilt angle; 5) neglecting the fringe effects

To analyze the forces in such a top plate tilting actuator system, a torque analysis is illustrated in Figure 3-4.

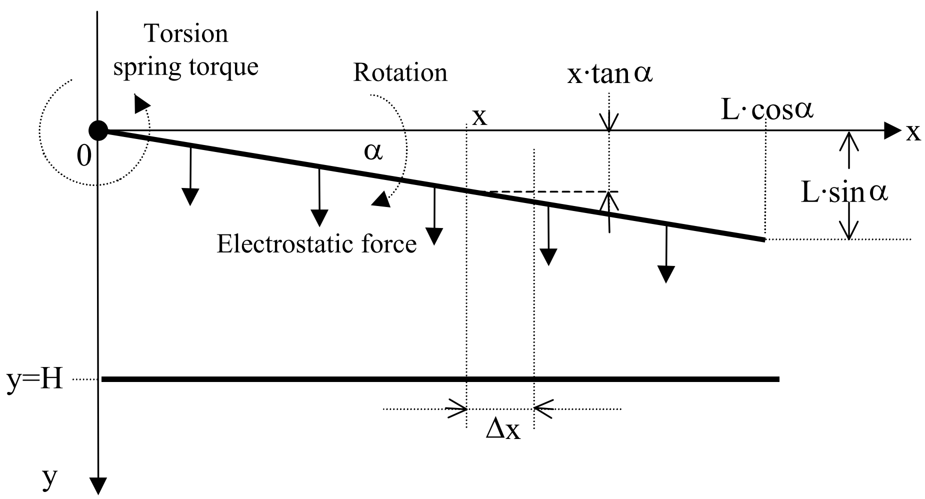

Figure 3-4 Force analysis of the tilting plate actuator system

The upward torque from the spring is:

$$T_{spring} = k \cdot \alpha \tag{3-11}$$

The downward torque from the actuation voltage V is:

$$T_{static} = \int_0^{L\cdot\cos\alpha} x \cdot \frac{\varepsilon \cdot W \cdot V^2}{2 \cdot (H - \tan\alpha \cdot x)^2} dx \tag{3-12}$$

In order to solve (3-12), let:

$$y = H - \tan\alpha \cdot x \tag{3-13}$$

So
$$x = \frac{H-y}{\tan\alpha}, \qquad dx = \frac{-1}{\tan\alpha}dy \tag{3-14}$$

when $x \in [0, L\cdot\cos\alpha]$, $\qquad y \in [H, H - L\cdot\sin\alpha]$ (3-15)

Substitute (3-14) and (3-15) into (3-12), we get:

$$T_{static} = \int_{H}^{H-L\cdot\sin\alpha} \frac{H-y}{\tan\alpha}\cdot\frac{\varepsilon\cdot W\cdot V^2}{2\cdot y^2}\cdot\frac{-1}{\tan\alpha}dy \tag{3-16}$$

$$T_{static} = \frac{\varepsilon\cdot W\cdot V^2}{2\cdot\tan^2\alpha}\int_{H}^{H-L\cdot\sin\alpha}\frac{y-H}{y^2}dy = \frac{\varepsilon\cdot W\cdot V^2}{2\cdot\tan^2\alpha}\cdot(\ln y + \frac{H}{y})\Big|_{H}^{H-L\cdot\sin\alpha}$$

$$= \frac{\varepsilon\cdot W\cdot V^2}{2\cdot\tan^2\alpha}(\ln\frac{H-L\cdot\sin\alpha}{H} + \frac{H}{H-L\cdot\sin\alpha} - 1) \tag{3-17}$$

When the system is balanced, $T_{spring} = T_{static}$, we have

$$k\cdot\alpha = \frac{\varepsilon\cdot W\cdot V^2}{2\cdot\tan^2\alpha}\cdot\left(\ln\frac{H-L\cdot\sin\alpha}{H} + \frac{H}{H-L\cdot\sin\alpha} - 1\right) \tag{3-18}$$

That is:
$$V = \tan\alpha\sqrt{\frac{2\cdot k\cdot\alpha}{\varepsilon\cdot W\cdot\left(\ln\frac{H-L\cdot\sin\alpha}{H} + \frac{H}{H-L\cdot\sin\alpha} - 1\right)}}$$

$$= \tan\alpha\sqrt{\frac{2\cdot k\cdot\alpha}{\varepsilon\cdot W}}\cdot\left(\ln\frac{H-L\cdot\sin\alpha}{H} + \frac{H}{H-L\cdot\sin\alpha} - 1\right)^{-\frac{1}{2}} \tag{3-19}$$

For a desired mirror tilt range, $R \in [0, \alpha_M]$, where α_M is the maximum tilt angle, we want to find the minimum actuating voltage needed.

From the discussion in Section 3.1, we know that the smaller gap H is, the lower the actuating voltage that is needed, as long as H is not too small to let pull-in happen. In order to find the smallest possible H, let us repeat the calculation we did in Section

3.2, that is to take the first order derivative to H on both sides of (3-19) and let $\frac{dV}{dH} = 0$. We get

$$\frac{dV}{dH} = \tan\alpha \cdot \sqrt{\frac{2 \cdot k \cdot \alpha}{\varepsilon \cdot W}} \cdot \frac{\frac{-H}{H - L \cdot \sin\alpha} \cdot \frac{L \cdot \sin\alpha}{H^2} - \frac{1}{H - L \cdot \sin\alpha} + \frac{H}{(H - L \cdot \sin\alpha)^2}}{2 \cdot \sqrt{\left(\ln\frac{H - L \cdot \sin\alpha}{H} + \frac{H}{H - L \cdot \sin\alpha} - 1\right)^3}}$$

$$= \tan\alpha \cdot \sqrt{\frac{2 \cdot k \cdot \alpha}{\varepsilon \cdot W}} \frac{\frac{L \cdot \sin\alpha}{H - L \cdot \sin\alpha} \cdot \frac{-1}{H} + \frac{L \cdot \sin\alpha}{(H - L \cdot \sin\alpha)^2}}{2 \cdot \sqrt{\left(\ln\frac{H - L \cdot \sin\alpha}{H} + \frac{H}{H - L \cdot \sin\alpha} - 1\right)^3}}$$

$$= \tan\alpha \cdot \sqrt{\frac{2 \cdot k \cdot \alpha}{\varepsilon \cdot W}} \frac{(L \cdot \sin\alpha)^2}{(H - L \cdot \sin\alpha)^2 \cdot H} \frac{1}{2 \cdot \sqrt{\left(\ln\frac{H - L \cdot \sin\alpha}{H} + \frac{H}{H - L \cdot \sin\alpha} - 1\right)^3}} \quad (3\text{-}20)$$

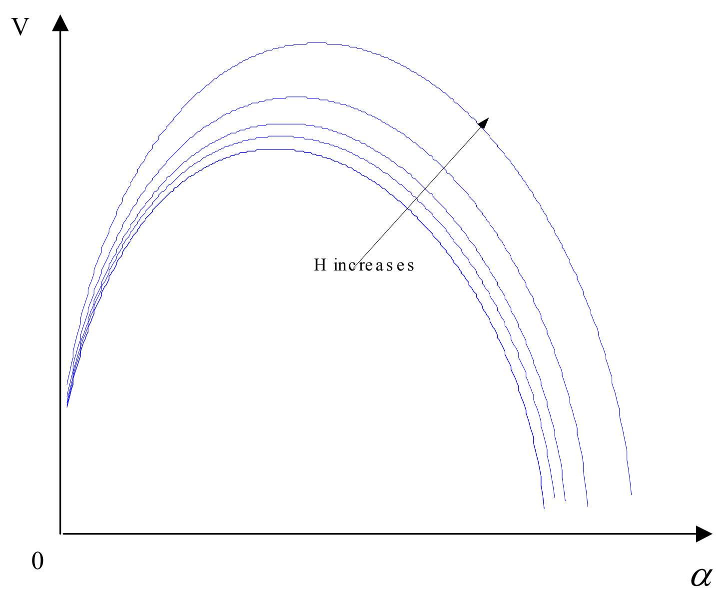

(a) V-α relationship at different H using Equation (3-15)

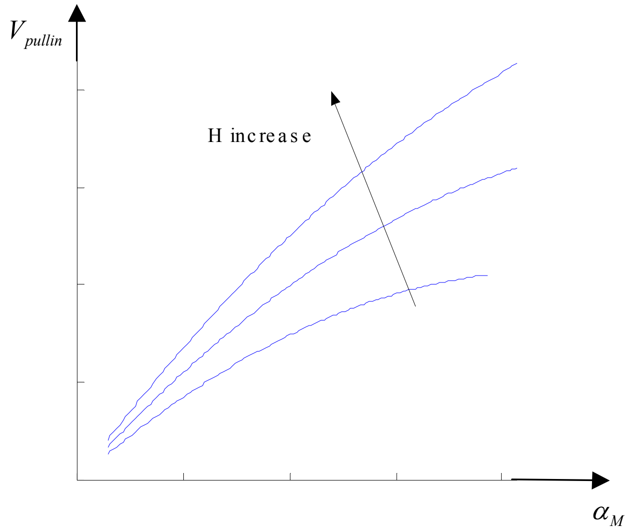

(b) V_{pullin} - α_M using Equation (3-28)

Comment: horizontal_V_pullin_alfa.m

Figure 3-5 The V-α relationship at different H

As k, W, α, L, H and $(\ln\frac{H-L\cdot\sin\alpha}{H}+\frac{H}{H-L\cdot\sin\alpha}-1)$ need to be positive to have physical meaning, the right side of Equation (3-20) is always greater than 0. Therefore, V is a monotonic-rising function of H and the required actuating voltage will drop with the decrease of H, until H is limited by the pull-in phenomena, as shown in Figure 3-5.

Comment: fla_V_alfa_mtplot.m

A MATLAB simulation result for Equation (3-19) is shown in Figure 3-5(a), to illustrate the angular displacement of the tilting top plate vs. the actuating voltage with different H values. Similar to what we observed in Section 3.2, we can see from Figure 3-5, the angular displacement increases first with the increase of actuating voltage. Then it reaches one critical point. The system moves to the unstable range if the angular displacement increases any further. Again here the pull-in phenomena appear. Another observation from Figure 3-5 is that the higher the H value the higher the pull-in voltage and the maximum tilt angle.

3.3.2 The pull-in condition: the relationship between H and $L \cdot \sin\alpha_M$

Now, let us find the pull-in condition in the electrostatic plate actuator system. In Equation (3-19), for any given actuating voltage V, the maximum obtainable equilibrium angular position of the tilting top plate can be calculated by the first order derivative with respect to α on both sides of (3-19) and let $\frac{dV}{d\alpha} = 0$ at $\alpha = \alpha_M$. We have

$$\frac{dV}{d\alpha} = \sqrt{\frac{2k}{\varepsilon \cdot W}} \cdot \frac{\frac{d}{d\alpha}\left(\frac{\alpha \cdot \tan^2 \alpha}{\ln \frac{H - L \cdot \sin\alpha}{H} + \frac{H}{H - L \cdot \sin\alpha} - 1} \right)}{2 \cdot \sqrt{\frac{\alpha \cdot \tan^2 \alpha}{\ln \frac{H - L \cdot \sin\alpha}{H} + \frac{H}{H - L \cdot \sin\alpha} - 1}}} = 0 \tag{3-21}$$

That is

$$\frac{d}{d\alpha}\left(\frac{\alpha \cdot \tan^2 \alpha}{\ln \frac{H - L \cdot \sin\alpha}{H} + \frac{H}{H - L \cdot \sin\alpha} - 1} \right) = 0 \tag{3-22-a}$$

Or

$$\frac{\frac{d}{d\alpha}\left(\alpha\cdot\tan^2\alpha\right)}{\ln\frac{H-L\cdot\sin\alpha}{H}+\frac{H}{H-L\cdot\sin\alpha}-1}-\frac{\alpha\cdot\tan^2\alpha\cdot\frac{d}{d\alpha}\left(\ln\frac{H-L\cdot\sin\alpha}{H}+\frac{H}{H-L\cdot\sin\alpha}-1\right)}{\left(\ln\frac{H-L\cdot\sin\alpha}{H}+\frac{H}{H-L\cdot\sin\alpha}-1\right)^2}=0 \tag{3-22-b}$$

Or

$$\left(\tan^2\alpha+2\cdot\alpha\cdot\frac{\sin\alpha}{\cos^3\alpha}\right)\cdot\left(\ln\frac{H-L\cdot\sin\alpha}{H}+\frac{H}{H-L\cdot\sin\alpha}-1\right)$$
$$=\frac{\alpha\cdot\sin^2\alpha}{\cos^2\alpha}\cdot\left(\frac{H}{H-L\cdot\sin\alpha}\cdot\frac{-L\cdot\cos\alpha}{H}+\frac{-H\cdot(-L\cdot\cos\alpha)}{(H-L\cdot\sin\alpha)^2}\right) \tag{3-22-c}$$

Or

$$\left(\frac{\sin\alpha}{\cos\alpha}+\frac{2\cdot\alpha}{\cos^2\alpha}\right)\cdot\left(\ln\frac{H-L\cdot\sin\alpha}{H}+\frac{H}{H-L\cdot\sin\alpha}-1\right)$$
$$=\alpha\cdot\sin\alpha\cdot L\cdot\left(\frac{-1}{H-L\cdot\sin\alpha}+\frac{H}{(H-L\cdot\sin\alpha)^2}\right) \tag{3-22-d}$$

Or

$$\left(\frac{\sin\alpha}{\cos\alpha}+\frac{2\cdot\alpha}{\cos^2\alpha}\right)\cdot\left(\ln\frac{H-L\cdot\sin\alpha}{H}+\frac{H}{H-L\cdot\sin\alpha}-1\right)=\alpha\cdot\frac{\sin^2\alpha\cdot L^2}{(H-L\cdot\sin\alpha)^2} \tag{3-22-e}$$

Or replacing $\alpha=\alpha_M$,

$$\left(\ln\frac{H-L\cdot\sin\alpha_M}{H}+\frac{H}{H-L\cdot\sin\alpha_M}-1\right)=\frac{L^2\cdot\sin^2\alpha_M}{(H-L\cdot\sin\alpha_M)^2}\frac{\alpha_M\cdot\cos^2\alpha_M}{(\sin\alpha_M\cdot\cos\alpha_M+2\alpha_M)} \tag{3-22}$$

(3-22) can be written in another form with H normalized to $L\cdot\sin\alpha_M$. That is:

$$\left(\ln \frac{\frac{H}{L \cdot \sin\alpha_M} - 1}{\frac{H}{L \cdot \sin\alpha_M}} + \frac{\frac{H}{L \cdot \sin\alpha_M}}{\frac{H}{L \cdot \sin\alpha_M} - 1} - 1 \right) = \frac{\cos^2 \alpha_M}{\left(\frac{H}{L \cdot \sin\alpha_M} - 1 \right)^2} \frac{\alpha_M}{(\sin\alpha_M \cdot \cos\alpha_M + 2\alpha_M)}$$

(3-23)

From (3-22) or (3-23), we can obtain the maximum equilibrium angular position of the tilting top plate. From (3-23) we can tell that α_M is a function of the plate actuator parameters H/L. That is

$$\alpha = \alpha_M = \alpha_M (H/L) \tag{3-24}$$

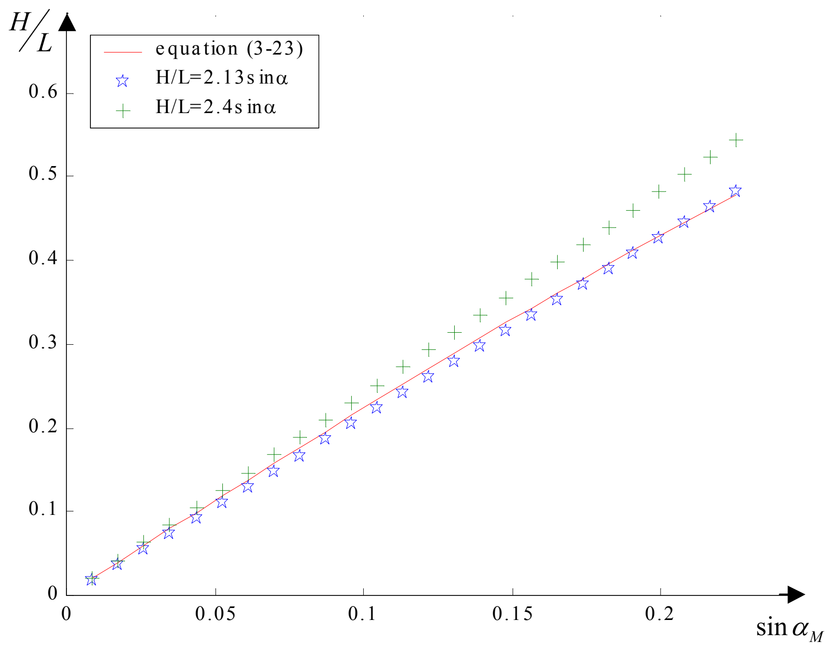

Figure 3-6 The relationship between H/L and $\sin\alpha_M$

This relationship between $\sin\alpha_M$ and H/L is shown in Figure 3-6 as the red line. From this figure, it is very interesting to notice that there is almost a liner relationship between $\sin\alpha_M$ and H/L. For comparison, $\sin\alpha_M = 2.13(H/L)$ is also shown in Figure 3-6 as the starred line. This straight starred line coincides well with the red one pretty. This also agrees well with $0.46\sin\alpha_M = (H/L)$, which is $\sin\alpha_M = 2.1739(H/L)$, according to the measurements from Buhler [69].

Comment: horizontal_H_alfa_plot.m

We can proceed further to prove that this linear relation between $\sin\alpha_M$ and H/L does exist. As mentioned in Chapter 2, the mirror angular displacement is less than 10 degrees (about 0.17 radians). which is a small number compared to 1. Thus for any $\alpha \in [0,\alpha_M]$, $\sin\alpha \approx \alpha$ and $\cos\alpha \approx 1$. Then (3-23) can be written as the following:

$$\left(\ln\frac{\dfrac{H}{L\cdot\sin\alpha_M}-1}{\dfrac{H}{L\cdot\sin\alpha_M}}+\frac{\dfrac{H}{L\cdot\sin\alpha_M}}{\dfrac{H}{L\cdot\sin\alpha_M}-1}-1\right)=\frac{1}{\left(\dfrac{H}{L\cdot\sin\alpha_M}-1\right)^2}\frac{\alpha_M}{(\alpha_M+2\alpha_M)}$$

$$=\frac{1}{3}\frac{1}{\left(\dfrac{H}{L\cdot\sin\alpha_M}-1\right)^2} \qquad (3\text{-}25)$$

The solution to (3-25) will be

$$\frac{H}{L\cdot\sin\alpha_M}=m \qquad (3\text{-}26)$$

where m is some constant satisfying:

$$\left(\ln\frac{m-1}{m}+\frac{m}{m-1}-1\right)=\frac{1}{3}\frac{1}{(m-1)^2} \qquad (3\text{-}27)$$

In (3-27) m must be greater than 1 to keep (3-27) to have a solution; $m > 1$. This is consistent with the physical picture that H should be greater than $L \cdot \sin\alpha_M$. At this point, we have finished the proof that a linear relationship holds between $\sin\alpha_M$ and H/L. This simplifies our design if we want to reach some specified α_M with the minimum actuating voltage. We can simply set $H = mL \cdot \sin\alpha_M$ without going through a very complex math calculation if we choose a reasonable m. $m = 2.4$ is such a reasonable number, as shown in Figure 3-6 with the straight crossed line. $m = 2.4$ is higher than 2.13, because we want to have some design margin.

3.3.3 The pull-in voltage

If we substitute (3-24) back into (3-19), we get the pull-in voltage.

$$V_{pull-in} = \tan\alpha_M \cdot \sqrt{\frac{k \cdot 2\alpha_M}{\varepsilon \cdot W \cdot \left(\ln\frac{H - L \cdot \sin\alpha_M}{H} + \frac{H}{H - L \cdot \sin\alpha_M} - 1 \right)}}$$

$$= \tan\alpha_M \cdot \sqrt{\frac{k \cdot 2\alpha_M \cdot (H - L \cdot \sin\alpha_M)^2 \cdot (2\alpha_M + \sin\alpha_M \cdot \cos\alpha_M)}{\varepsilon \cdot W \cdot \sin^2\alpha_M \cdot L^2 \cdot \cos^2\alpha_M}}$$

$$= (H - L \cdot \sin\alpha_M) \cdot \frac{1}{L \cdot \cos^2\alpha_M} \cdot \sqrt{\frac{k \cdot 2}{\varepsilon \cdot W}} \cdot \sqrt{\alpha_M \cdot (2\alpha_M + \sin\alpha_M \cdot \cos\alpha_M)} \quad (3\text{-}28)$$

One observation from (3-28) is that by reducing H, we can reduce the pull-in voltage, while maintain the same maximum angular displacement of the top plate, as shown in Figure 3-5(b). This also agrees with our intuition that the reduction of the initial gap distance between the two plates will bring down the pull-in voltage. However, the initial gap between the two plates must be greater than $L \cdot \sin\alpha_M$ to allow the rotation of the top movable plate. This is consistent with our previous conclusion that $m > 1$.

These observations also agree with the discussion in Section 3.2, where H reduction has a limit to allow the top plate to have a specified movable range. Here the minimum of H is limited by the angular displacement α_M of the tilting top plate.

To reduce the overall gap distance between the two plates, we can make the bottom fixed plate be tilted. So the overall gap distance between the two plates will become smaller, and the pull-in voltage will be reduced. If we tilt the bottom plate to an optimal angle, we will get the least pull-in voltage, which is the minimum required voltage corresponding to the same maximum tilt angle of the top plate.

3.4 An optimal plate actuator with the tilted fixed bottom plate

In this section, we will discuss the plate actuator with a tilted bottom plate. This actuator has the same movable top plate as discussed in the previous section with a horizontal bottom plate. The difference is the bottom plate. Here, the fixed bottom plate tilts an angle β relative to the horizontal line, as shown in Figure 3-7. The torque analysis of this system is shown in Figure 3-8. The assumptions in Section 3.3 are still held in this section.

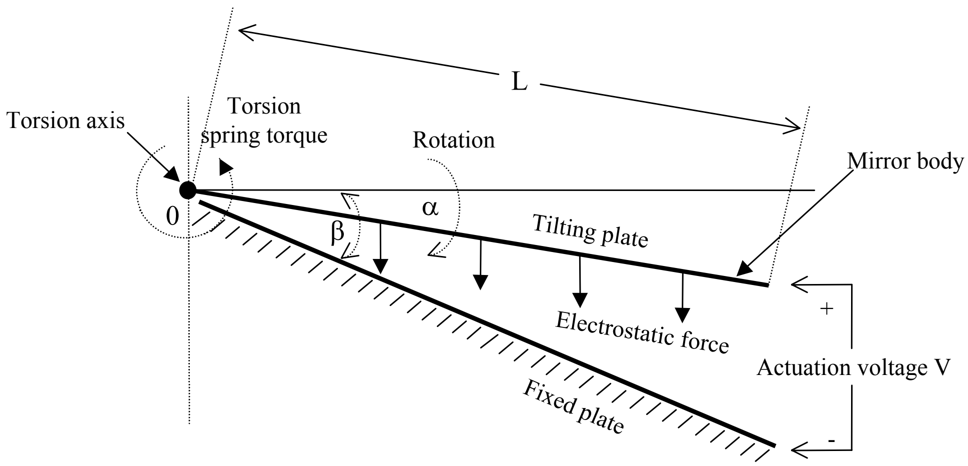

Figure 3-7 A plate actuator with a fixed bottom plate tilted by an angle β

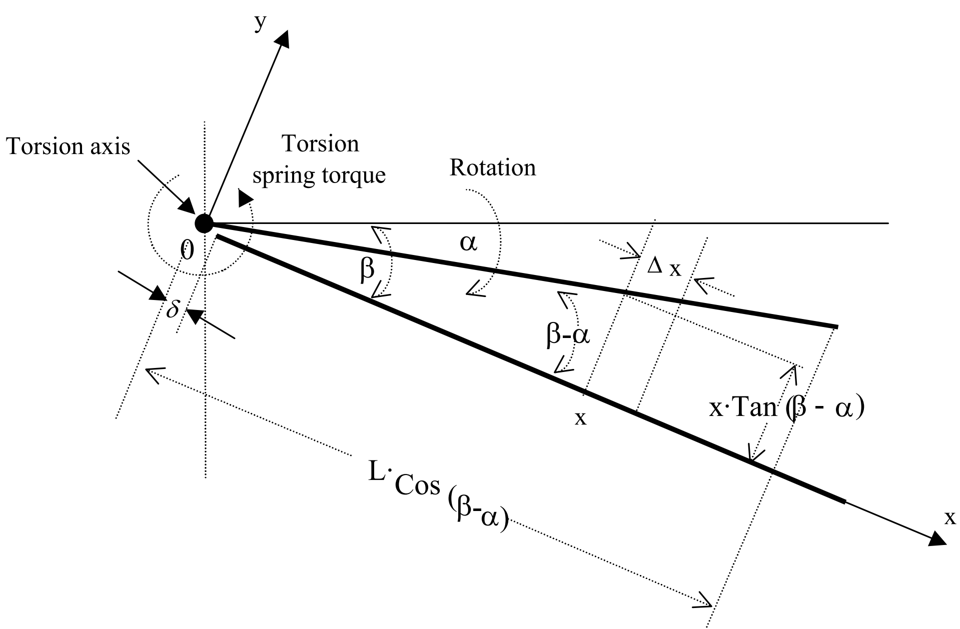

Figure 3-8 The torque analysis of a plate actuator with a fixed bottom plate tilted by an angle β

In this system, the upward torque from the spring is the same as in (3-11) and the downward torque from the electrostatic force is

$$T_{static} = \int_{\delta}^{L\cdot\cos(\beta-\alpha)} \frac{\varepsilon \cdot W \cdot x \cdot V^2 \cdot dx}{2\cdot(x\cdot\tan(\beta-\alpha))^2} = \int_{\delta}^{L\cdot\cos(\beta-\alpha)} \frac{\varepsilon\cdot W\cdot V^2\cdot dx}{2\cdot x\cdot\tan^2(\beta-\alpha)} \tag{3-29}$$

There are a couple of points to be observed from Figure 3-7 and 3-8. First, since the fixed bottom plate and the movable top plate are applied with different electrical potential, they can not electrically contact each other. Thus the fixed bottom plate can not touch the point 0, as the movable top plate does. Therefore, we let it start at $x=\delta$, which is a number with a very small value, very close to but not equal to zero, to keep the two plates electrically isolated. That is why the integration lower limit of (3-29) is δ. Second, the angular displacement of the top plate can not be greater than β. That is $\beta > \alpha$. The bottom plate serves as a physical stopper to the rotation of the top plate.

To solve equation (3-29), we get:

$$\begin{aligned} T_{static} &= \frac{\varepsilon\cdot W\cdot V^2}{2\cdot\tan^2(\beta-\alpha)} \cdot \int_{\delta}^{L\cdot\cos(\beta-\alpha)} \frac{\cdot dx}{x} \\ &= \frac{\varepsilon\cdot W\cdot V^2\cdot\ln\dfrac{L\cdot\cos(\beta-\alpha)}{\delta}}{2\cdot\tan^2(\beta-\alpha)} \end{aligned} \tag{3-30}$$

When the system is balanced, $T_{spring} = T_{static}$, we have

$$k\cdot\alpha\cdot = \frac{\varepsilon\cdot W\cdot V^2\cdot\ln\dfrac{L\cdot\cos(\beta-\alpha)}{\delta}}{2\cdot\tan^2(\beta-\alpha)} \tag{3-31}$$

That is:

$$V=\sqrt{\frac{k\cdot\alpha\cdot 2\cdot\tan^2(\beta-\alpha)}{\varepsilon\cdot W\cdot\ln\frac{L\cdot\cos(\beta-\alpha)}{\delta}}}$$

$$=\tan(\beta-\alpha)\cdot\sqrt{\frac{2\cdot k\cdot\alpha}{\varepsilon\cdot W\cdot\ln\frac{L\cdot\cos(\beta-\alpha)}{\delta}}} \tag{3-32}$$

To obtain the minimum actuation voltage V, let us take the first order derivative to β on both sides of (3-32) and let $\frac{dV}{d\beta}=0$.

$$\frac{dV}{d\beta}=\frac{d}{d\beta}\left(\tan(\beta-\alpha)\cdot\sqrt{\frac{2\cdot k\cdot\alpha}{\varepsilon\cdot W\cdot\ln\frac{L\cdot\cos(\beta-\alpha)}{\delta}}}\right)$$

$$=\sqrt{\frac{2\cdot k\cdot\alpha}{\varepsilon\cdot W}}\cdot\left[\left(\frac{d}{d\beta}\tan(\beta-\alpha)\right)\cdot\sqrt{\frac{1}{\cdot\ln\frac{L\cdot\cos(\beta-\alpha)}{\delta}}}+\tan(\beta-\alpha)\cdot\frac{d}{d\beta}\sqrt{\frac{1}{\cdot\ln\frac{L\cdot\cos(\beta-\alpha)}{\delta}}}\right]$$

$$=\sqrt{\frac{2\cdot k\cdot\alpha}{\varepsilon\cdot W}}\cdot\left[\begin{array}{l}\frac{1}{\cos^2(\beta-\alpha)}\cdot\sqrt{\frac{1}{\cdot\ln\frac{L\cdot\cos(\beta-\alpha)}{\delta}}}+\\ \tan(\beta-\alpha)\cdot\frac{-1}{2}\sqrt{\frac{1}{\left(\ln\frac{L\cdot\cos(\beta-\alpha)}{\delta}\right)^3}}\frac{\delta}{L\cdot\cos(\beta-\alpha)}\cdot\frac{-L\cdot\sin(\beta-\alpha)}{\delta}\end{array}\right]$$

$$=\sqrt{\frac{2\cdot k\cdot\alpha}{\varepsilon\cdot W}}\cdot\sqrt{\frac{1}{\left(\ln\frac{L\cdot\cos(\beta-\alpha)}{\delta}\right)^3}}\cdot\left[\frac{\ln\frac{L\cdot\cos(\beta-\alpha)}{\delta}}{\cos^2(\beta-\alpha)}+\frac{1}{2}\cdot\tan^2(\beta-\alpha)\right] \tag{3-33}$$

Since $\beta>\alpha$, Equation (3-33) tells that $\frac{dV}{d\beta}\geq 0$ in the range of $\alpha\in[0,\beta]$ and $\beta\in[0,90^\circ]$. Thus V is a monotonic function of β. And because V is proportional to

$\tan(\beta-\alpha)$, the actuating voltage V will be reduced when β is reduced. Again, reducing β is limited by the happening of pull-in with the maximum angular displacement α_M. Next, we will find the relationship between α_M and β.

Repeat the same calculation we did to get equation (3-23) in Section 3.3, which is to keep β fixed and take the first order derivative to α on both sides of (3-32) and let $\frac{dV}{d\alpha}=0$. We can get the pull-in voltage $V=V_{pull-in}$ and the corresponding maximum equilibrium rotation position α_M of the top plate in the balanced electrostatic plate actuator system.

$$\frac{dV}{d\alpha}=\frac{\frac{d}{d\alpha}\left(\frac{k\cdot\alpha\cdot 2\cdot\tan^2(\beta-\alpha)}{\varepsilon\cdot W\cdot\ln\frac{L\cdot\cos(\beta-\alpha)}{\delta}}\right)}{2\cdot\sqrt{\frac{k\cdot\alpha\cdot 2\cdot\tan^2(\beta-\alpha)}{\varepsilon\cdot W\cdot\ln\frac{L\cdot\cos(\beta-\alpha)}{\delta}}}}=0 \tag{3-34}$$

that is
$$\frac{d}{d\alpha}\left(\frac{\alpha\cdot\tan^2(\beta-\alpha)}{\ln\frac{L\cdot\cos(\beta-\alpha)}{\delta}}\right)=0 \tag{3-35}$$

or
$$\frac{\frac{d}{d\alpha}\left(\alpha\cdot\tan^2(\beta-\alpha)\right)}{\ln\frac{L\cdot\cos(\beta-\alpha)}{\delta}}-\frac{\left(\alpha\cdot\tan^2(\beta-\alpha)\right)\cdot\frac{L}{\delta}\sin(\beta-\alpha)}{\frac{L\cdot\cos(\beta-\alpha)}{\delta}\cdot\left(\ln\frac{L\cdot\cos(\beta-\alpha)}{\delta}\right)^2}=0 \tag{3-36}$$

Or

$$\left(\frac{\tan(\beta-\alpha)}{\left(\ln\frac{L\cdot\cos(\beta-\alpha)}{\delta}\right)^2}\right)\left[\left(\tan(\beta-\alpha)-\frac{2\cdot\alpha}{\cos^2(\beta-\alpha)}\right)\cdot\ln\frac{L\cdot\cos(\beta-\alpha)}{\delta}-\alpha\cdot\tan^2(\beta-\alpha)\right]=0$$

Or

$$\left(\tan(\beta-\alpha)-\frac{2\cdot\alpha}{\cos^2(\beta-\alpha)}\right)\cdot\ln\frac{L\cdot\cos(\beta-\alpha)}{\delta}=\alpha\cdot\tan^2(\beta-\alpha)$$

That is:

$$\frac{4\cdot\alpha_M}{\sin 2(\beta-\alpha_M)}=1-\alpha_M\cdot\frac{\tan(\beta-\alpha_M)}{\ln\frac{L\cdot\cos(\beta-\alpha_M)}{\delta}} \tag{3-37}$$

Equation (3-37) gives the relationship between the tilt angle β of the bottom fixed plate and the maximum tilt angle α_M of the top movable plate. It tells that α_M is a variable determined by β. This suggests that if we want to design a plate actuator with a maximum tilt angle of α_M, the tilt angle β for the bottom plate must be no less than the value β that satisfies (3-37).

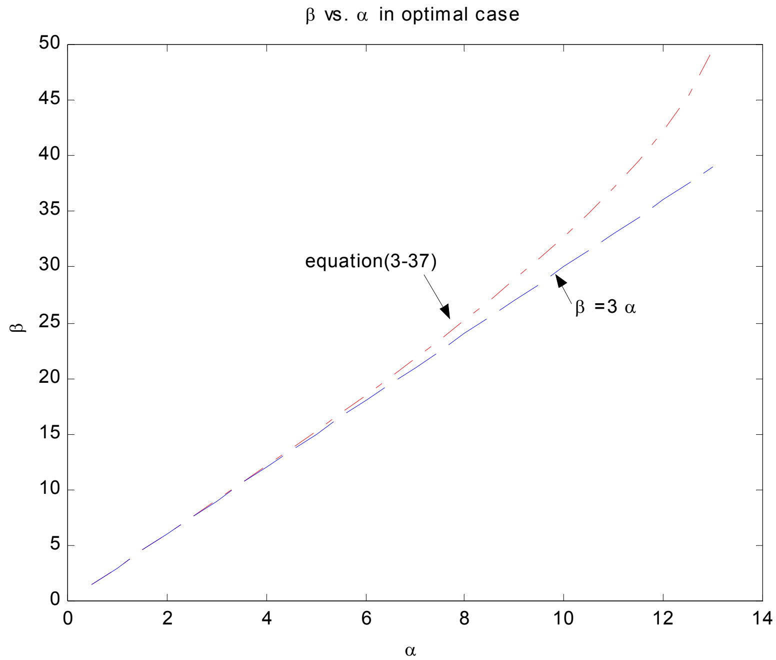

(a) The relationship between α_M (mirror tilt angle) and β (the angle of the bottom plate) in the tilted bottom plate actuator. The unit for both α_M and β is degree.

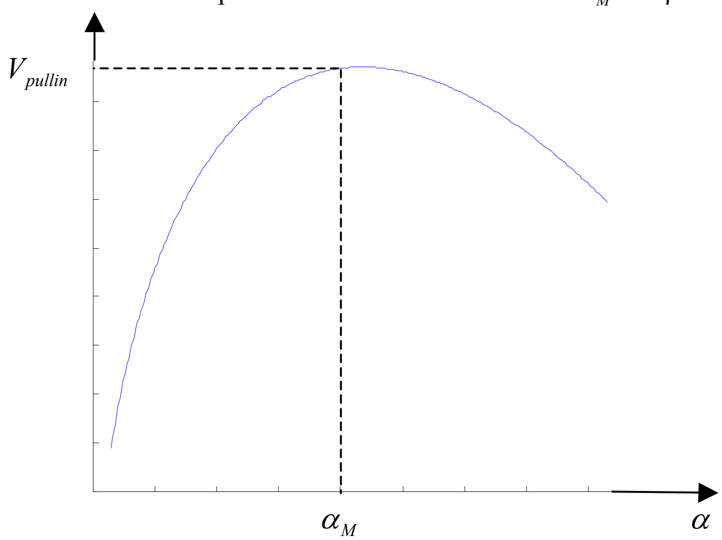

(b) The relationship between V and α as in Equation (3-32)

Figure 3- 9 The relationships about α which hold in the fixed tilted bottom plate

Combining (3-32) and (3-37), we can obtain the corresponding pull-in voltage at equilibrium. The relationship between β and α_M as expressed in (3-37) is illustrated in Figure 3-9 (a). The unit of both α and β is degree, with $\delta = 4$ and $L = 125$. Figure 3-9 (b) shows the relationship between V and α as in Equation (3-32).

Therefore, after the top plate's maximum tilt angle α_M is determined by the specific application, the fixed bottom plate's tilt angle β can be determined by Equation (3-37). This tilted bottom plate structure will result in a minimum actuating voltage $V_{pull-in}$ according to Equation (3-32). A detailed design example will be given in the next two sections.

Until to this point, we have studied three cases of plate actuator systems. One has two parallel plates; one has a tilting top plate and the fixed horizontal bottom plate; and the other one has a tilting top plate and the fixed tilted bottom plate. For comparison, the relationships between V and α for both the last two cases are shown in Figure 3-10. This comparison is based on to achieve the same α_M, the maximum angular displacement of the top plate as well as the same top plate and the same torsion spring in the systems. The data used to obtain Figure 3-10 are shown in Table 3-1. The conclusion is that for a tilting top plate actuator, the tilted bottom plate structure has less voltage requirement than the horizontal bottom plate structure.

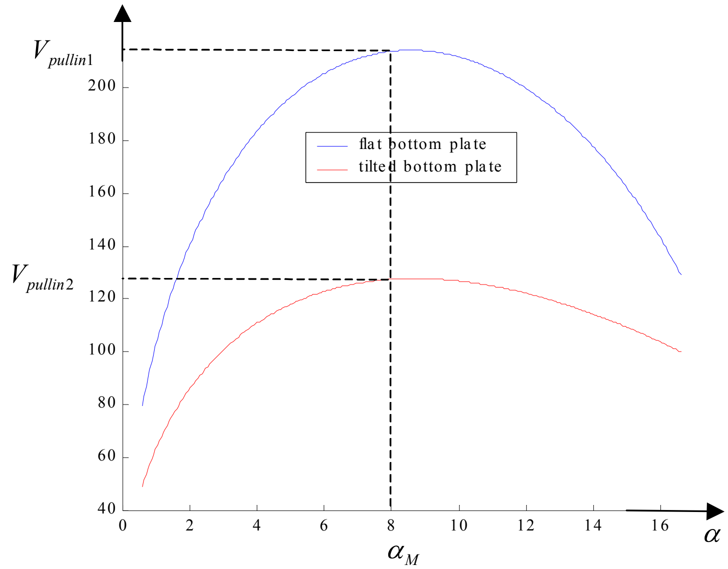

Figure 3-10 The comparison between the horizontal bottom plate and the tilted bottom plate

A horizontal fixed bottom plate	A tilted fixed bottom plate
$\alpha_M = 8$ degrees $k = 3.3901\times10^{-9}$ N/m, $\varepsilon = 8.854\times10^{-12}$ $L = 125$ µm, $W = 250$ µm $H = 40.235$ µm according to (3-23) $V_{pullin1} = 208.1$ V	$\alpha_M = 8$ degrees $k = 3.3901\times10^{-9}$ N/m, $\varepsilon = 8.854\times10^{-12}$ $L = 125$ µm, $W = 250$ µm, $\delta = 4$ µm, $\beta = 27.7179$ degrees according to (3-37) $V_{pullin2} = 127.8$ V

Table 3-1 The data used to compare the horizontal bottom plate structure and the tilted bottom plate structure

3.5 Design examples

In this section, two design examples will be presented, after the methodology to use an optimal bottom plate was developed. For comparison, in both examples, they have the same top plate as well as the torsion spring. One of the examples has a fixed horizontal bottom plate as shown in Figure 3-3. The other example has a fixed tilted bottom plate as shown in Figure 3-7. The schematic of the structure shown in Figure 3-11 is developed from Figure 3-3 and the schematic of the structure shown in Figure 3-12 is developed from Figure 3-7. The top plate is made of gold with width of 250μm, thickness of 2μm and length of 125 μm. The torsion spring, too made of gold, has width of 2μm, thickness of 2μm, and length of 35μm. That is

$$L_M = 125 \ \mu\text{m},\ W = 250\,\mu\text{m},\ t = 2\,\mu\text{m} \tag{3-38}$$

$$l_t = 35 \ \mu\text{m},\ W_t = 2\,\mu\text{m},\ t = 2\,\mu\text{m} \tag{3-39}$$

Because the torsion axis is located at the center of the torsion spring, L corresponding to what shown in Figure 3-3 and Figure 3-7 is

$$L = L_M - \frac{W_t}{2} = 125 - 1 = 124\ \mu\text{m}. \tag{3-40}$$

The structure of this section is the following. First the methods to calculate the spring stiffness constant k are presented. Then an example is given using a tilted bottom plate, followed by another example using a horizontal bottom plate for comparison. ANSYS simulations are presented in each example. The conclusion will be that lower voltage is obtained in the tilted bottom example than in the horizontal bottom example to reach the same tilt angle of the top movable plate.

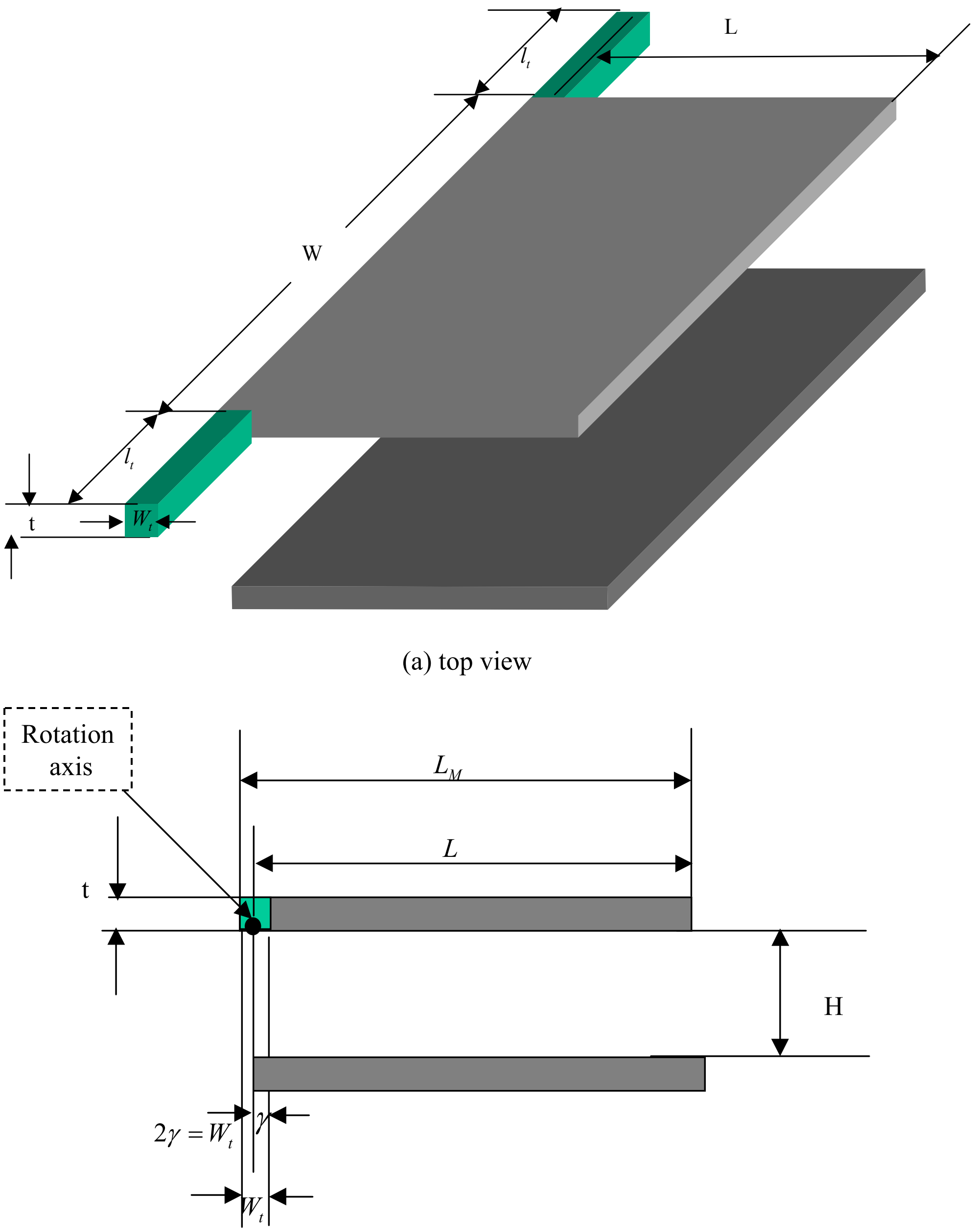

(a) top view

(b) side view

Figure 3-11 The schematic of the parallel plate structure

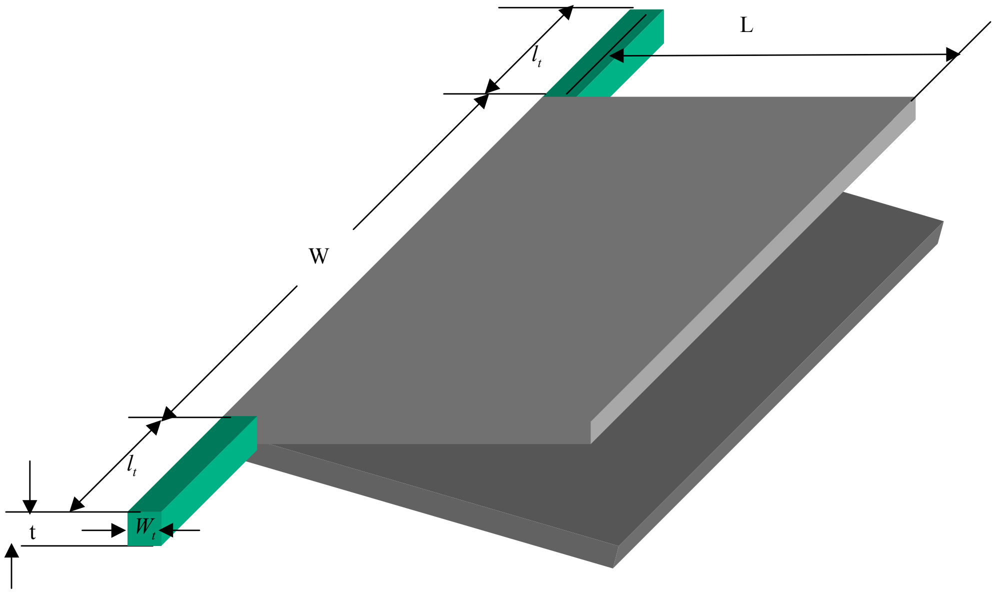

(a) top view

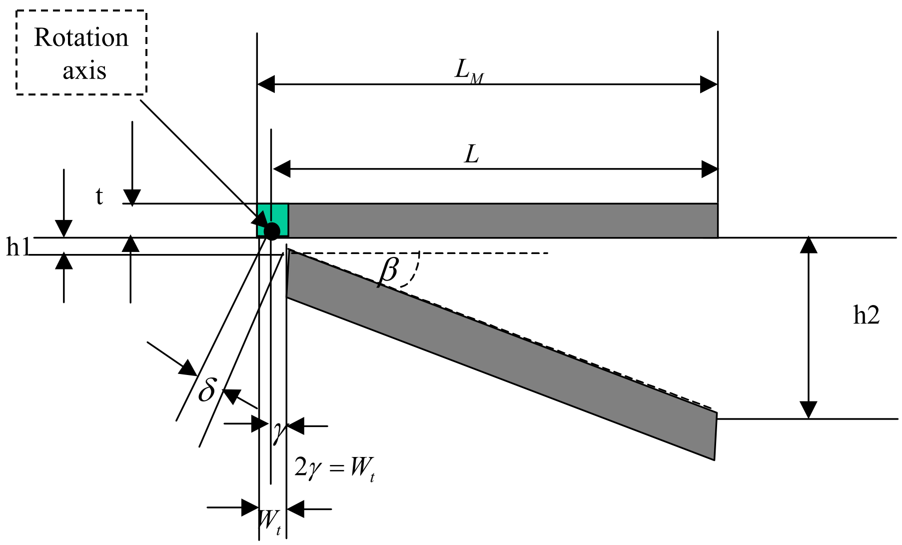

(b) side view

Figure 3-12 The structure of a design example

3.5.1 Calculation of the torsion stiffness

To proceed with our design, we need to know the torsion stiffness k related to the specific torsion spring. Two methods are used to calculate k here. One of the methods is to obtain k by using the mechanical structure data of the torsion spring directly. The other method is to obtain k according to Equation (3-32) based on ANSYS simulation. These methods can achieve two purposes here. One purpose is to obtain k to pursue our design. Another purpose is to check the correctness of (3-32) by calculating the torsion stiffness k through it.

The torsion spring, as shown in Figure 3-11 and Figure 3-12, has a cross section shown in Figure 3-13. One end of the torsion spring is connected with the top plate, while the other end is fixed in position. For a torsion spring using isotropic material with a rectangular cross-section, according to Young [66], its stiffness can be expressed approximately as:

$$k = \frac{G \cdot a \cdot b^3}{l_t}\left(\frac{16}{3} - 3.36 \cdot \frac{b}{a} \cdot \left(1 - \frac{b^4}{12a^4}\right)\right) \tag{3-41}$$

$$G = \frac{E}{2 \cdot (1+\nu)} \tag{3-42}$$

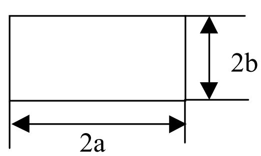

Figure 3-13 A cross-section of the flexure hinge suspension

where G is the shear modulus for the material; E is the Young's modulus of the material; ν is the Poisson's ratio of the material; l_t is the length of the torsion spring; a is the half of the hinge width, b is the half of the hinge thickness.

Equation (3-41) suggests that several ways can be implemented to change the stiffness k, such as the change of the material or the size of the flexure hinge. For example, we can increase the length l or decrease the thickness t to decrease k.

With the structure data here for the torsion spring as shown in Figure 3-11 or Figure 3-12, using (3-39), we have

$$l_t = 35\ \mu\text{m},\ W_t = 2a = 2\ \mu\text{m},\ t = 2b = 2\ \mu\text{m} \tag{3-43}$$

The material of the hinge is gold, with parameters

$$E = 7.7\times10^{10}\ \text{Pa},\ \nu = 0.42 \tag{3-44}$$

Combined (3-41), (3-42), (3-43), and (3-44), the stiffness constant k is

$$k = 3.9146\times10^{-9}\ \text{Nm/radian} \tag{3-45}$$

So far, the stiffness constant k has been calculated on the basis of its mechanical structural data. Another way to get the stiffness constant k is from an ANSYS simulation result. We can rewrite (3-32) as

$$k = \left(\frac{V}{\tan(\beta-\alpha)}\right)^2 \cdot \frac{\varepsilon\cdot W}{2\alpha}\cdot \ln\frac{L\cdot\cos(\beta-\alpha)}{\delta} \tag{3-46}$$

If we know the applied voltage V and the resulting tilt angle α from ANSYS simulation along with other structure parameters such as β, W and L, k can be calculated using (3-46). Two cases of ANSYS simulation results are listed in the Table 3-2, based on the structure shown in Figure 3-12.

$\beta = 0.4838$, $W = 250\,\mu$m, $L = 124\,\mu$m, $\delta = \gamma / \cos\beta = 2/\cos(0.4838)\,\mu$m		
Case number	Applied voltage V	Tilting displacement μm
1	111	11.66
2	125	14.77

Table 3-2 ANSYS simulation results with a tilted bottom plate

In the first case, the tilt displacement of the top plate is $d_m = 11.66$ μm, the tilt angle α is $\alpha = a\sin(d_m / L) = a\sin(11.66/124) = 5.3525$ degrees. Putting all these parameters into (3-46), the calculated k is ,

$$k = 3.9031 \times 10^{-9} \tag{3-47}$$

To check this, we recalculate k by using the second case in Table 3-1. This time, the tilt displacement at the end of $d_m = 14.77\,\mu$m, using the k just calculated from (3-47) into (3-32), the calculated V is 124.7409, a very good approximation to 125V from the ANSYS simulation.

The error between the k calculated from theoretical Equation (3-41) and the one calculated from the ANSYS simulation along with (3-46) is

$$error = \frac{3.9146\times10^{-9} - 3.9031\times10^{-9}}{3.9146\times10^{-9}}\times100\% \approx 0.29\% \qquad (3\text{-}48)$$

This shows a good agreement between Equation (3-41) and (3-46). As Equation (3-46) is obtained from Equation (3-32), this agreement verifies the correctness of our Equation (3-32).

3.5.2 A design example of an optimal plate actuator with the tilted bottom plate

Our first design example is based on the structure shown in Figure 3-12. Assume that the system requirement is to have the maximum tilt angle to be 8 degrees. To give some design margin, the maximum tilt angle is set to be 8.7 degrees, which is $\alpha_M = 0.1517$ radians.

$$\alpha_M = 0.1517 \text{ radians} \qquad (3\text{-}49)$$

To find the needed tilt angle β for the bottom plate, using (3-37), (3-38), (3-40)

$$\frac{4\cdot 0.1517}{\sin 2(\beta - 0.1517)} = 1 - 0.1517\cdot\frac{\tan(\beta - 0.1517)}{\ln\frac{124\cdot\cos(\beta - 0.1517)}{4}} \qquad (3\text{-}50)$$

Solving (3-50),

$$\beta = 0.4833 \text{ radians} \qquad (3\text{-}51)$$

This is $\beta = 27.71$ degrees, which means that the bottom fixed plate for the optimal plate actuator has an angle of 27.71 degrees with the horizontal line. To design such a tilted bottom plate, we can use Figure 3-12(b):

$$\beta = a\tan\left(\frac{h_2 - h_1}{L - \gamma}\right) \qquad (3\text{-}52)$$

If we choose $h_1 = 1.9$ μm, $h_2 = 66$ μm, γ=2μm, then

$$\beta = a\tan\left(\frac{h_2 - h_1}{L - \gamma}\right) = a\tan\left(\frac{66 - 1.9}{124 - 2}\right) = 0.4838 \qquad (3\text{-}53)$$

Equation (3-53) shows that the bottom plate does have the desired angle.

Using this β value and the structure shown in Figure 3-12, we can write an ANSYS simulation program with a simulation result shown in Figure 3-14. The ANSYS simulation shows that When $V = 118$ V, a tilt displacement at the free end of the top plate of $d_m = 18.134$ um. This corresponds to a tilt angle of $\alpha = a\sin(d_m / L) = a\sin(18.134/124) = 0.1468$ radians, which is 8.411 degrees. This result meets our expectation to tilt the top plate to 8 degrees.

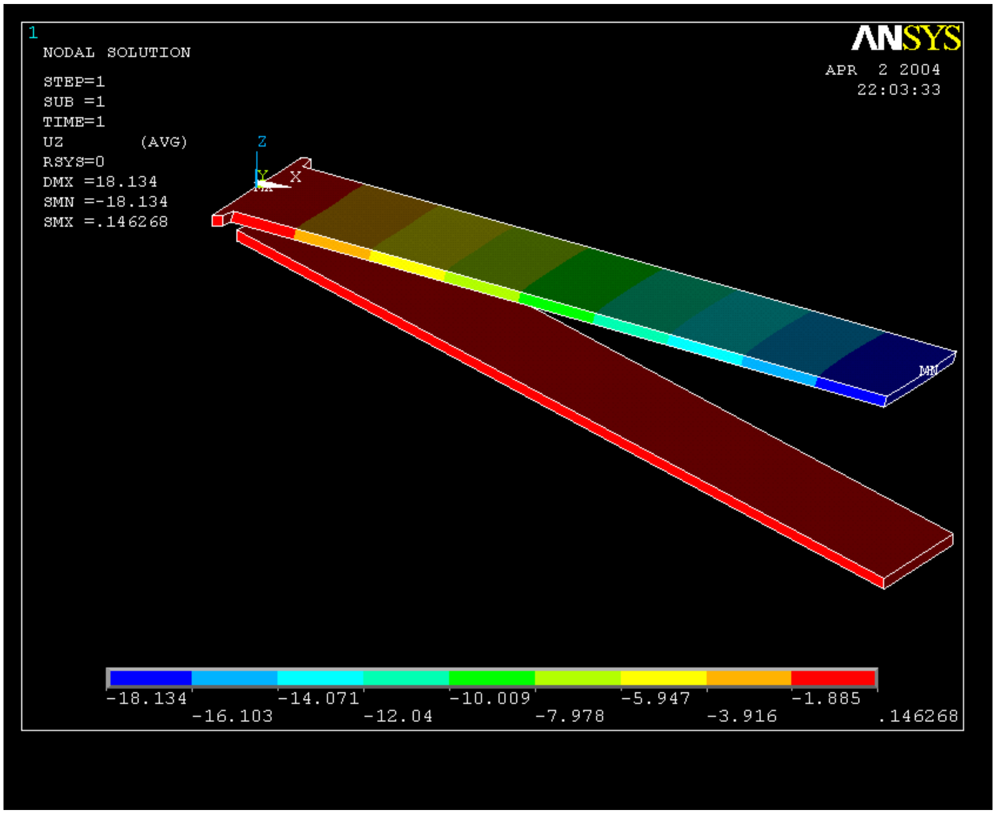

Figure 3-14 The ANSYS simulation of a plate actuator with a tilted bottom plate When $V = 118$ V, the tilt displacement at the free end of the top plate of $d_m = 18.134$ um

To this point, we have finished our design of an optimal plate actuator with a fixed bottom plate with a tilt angle of 0.4838 radians (27.7197 degrees). Next we compare this fixed tilted bottom structure with the structure of a fixed horizontal bottom plate, in order to emphasize the benefits of using a tilted bottom plate to reduce the driving voltage in the plate actuator systems.

3.5.3 A design example with the horizontal bottom plate structure

In this subsection, our design example is based on the structure shown in Figure 3-11. Our target is the same as before, to have the top plate to achieve a desired maximum tilt angle of 8 degrees. Again by taking some design margin, the designed maximum tilt angle is set to be 8.7 degrees; that is $\alpha_M = 0.1517$ radians. To find the needed H for this horizontal bottom plate, using (3-22), (3-38), (3-40), that is

$$\left(\ln\frac{H-124\cdot\sin 0.1517}{H}+\frac{H}{H-124\cdot\sin 0.1517}-1\right) = \frac{124^2\cdot\sin^2 0.1517}{\left(H-124\cdot\sin 0.1517\right)^2}\frac{\alpha 0.1517\cos^2 0.1517}{\left(\sin 0.1517\cdot\cos 0.1517+20.1517\right)} \tag{3-54-a}$$

Or

$$H = 41.25\,\mu\text{m} \tag{3-54-b}$$

We can also use (3-26) with $m = 2.4$, $\alpha = 8$ degrees, which is 0.1396 radians to calculate H.

$$H = m\cdot L\cdot\sin\alpha = 2.4\cdot 124\cdot\sin 0.1396 = 41.4179\,\mu\text{m} \tag{3-55}$$

(3-55) and (3-54) agrees very well. One point to be mentioned is that in using (3-55), because we put margin in choosing m, α is the desired maximum value of 8 degrees without adding any margin.

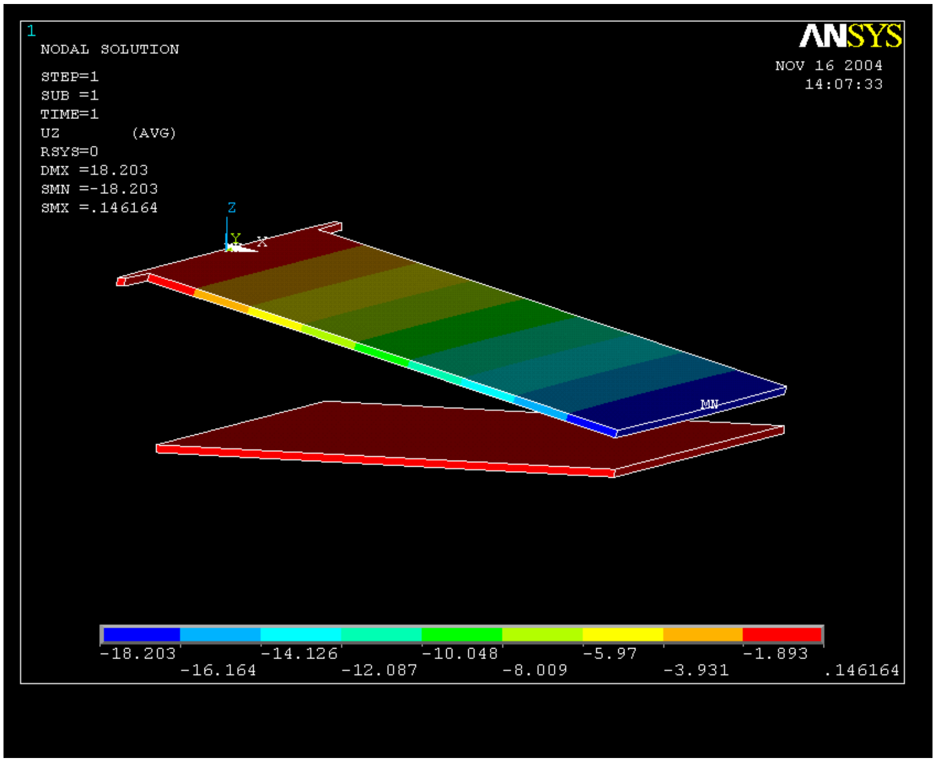

Figure 3-15 The ANSYS simulation of a plate actuator system with a horizontal fixed bottom plate.

When $V = 226.8$ V, the tilt displacement at the free end of the top plate of $d_m = 18.203$ um.

Based on the above calculations, the bottom fixed plate will be at H=42µm below the top plate, as shown in Figure 3-11. Using the structure in Figure 3-11 to run an ANSYS simulation, when V=226.8V, the ANSYS simulation presents a tilting displacement at the free end of the top plate of $d_m = 18.203$ um, as shown in Figure 3-15. This corresponds to a tilt angle of

$\alpha = a\sin(d\_\max/L) = a\sin(18.203/124) = 0.147$ radians, which is 8.45 degrees.

Compared the data we have for the tilted bottom plate, where a tilt angle of 0.14368 radians when V=118V, here for a horizontal bottom plate, we achieve a tilt angle of 0.147 radians when V=226.8V. From these simulations, we get the conclusion that the tilted fixed bottom plate structure reduces by about half of the required voltage over that required by the horizontal bottom structure.

3.5.4 Summary of the comparison of three plate-actuator configurations

So far, beginning with the concept of pull-in phenomena in electrostatic actuated plate actuators, we have developed a methodology to design a tilted fixed bottom electrostatic plate actuator in an effort to reduce the actuating voltage. This has been confirmed by the ANSYS simulation. We have found that there is a very simple linear approximation between the initial gap distance H and $L\sin\alpha$, which holds for the horizontal bottom plate. Bearing all these in mind, we will begin our next section to design the optimal plate actuators in MEMS mirror actuator system for the optical switch applications.

3.6 Multi-step approximation to an optimal tilted bottom plate

In this section, we apply the plate actuator optimization method developed in previous sections to design and implement actual MEMS mirror actuators in optical switch applications. First we need to review some of the special characters of these optical MEMS actuators to make sure that our design will meet all those requirements. Second, our design should be able to be implemented using the available planar fabrication technologies, so implementation limitations need to be considered and some trade-offs need to be made to balance the performance and implementation cost. The goal is to use current matured silicon planar processes to implement the designed optimal actuators using the least number of process steps, which means the lowest cost.

3.6.1 A half-mirror structure analysis for a MEMS mirror actuator

We implement the optimal tilted bottom plate discussed in the previous sections with a Multi-step (N-steps) approximation. As discussed in Chapter 2, each mirror in the MEMS actuator can have one rotation-axis or two-rotation axis. Because it is easy to analyze one rotation-axis case and the same methodology can be applied on the two rotation-axis case, here we will focus on the analysis of the mirror structure with one rotation-axis.

A one rotation-axis has two independent electroplates. Recall Equation (3-2), which shows that the electrostatic force is proportional to the area of the actuator plate; so a two- electro-plate design occupying the full area is made and shown in Figure 3-16 (a). A two electro-plate actuator occupies as much area as the entire mirror plate occupied to get the maximum actuation force. This translates into minimum actuation voltage needed.

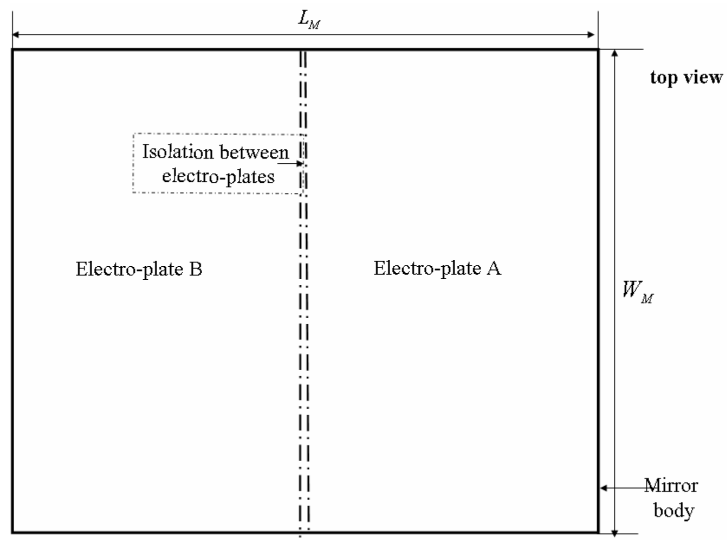

Figure 3-16 The top view of an MEMS actuator with one rotation-axis and the maximum area usage

Thus if we ignore the isolation area width, which normally is very small, for each electro-plate shown in Figure 3-16, its width is W_m and its length is $L = {L_m}/{2}$

As pointed out in Chapter 2, when actuating the mirror, only one of two electro-plates will be actuated. This means that these two bottom electroplates A and B can not be actuated simultaneously.

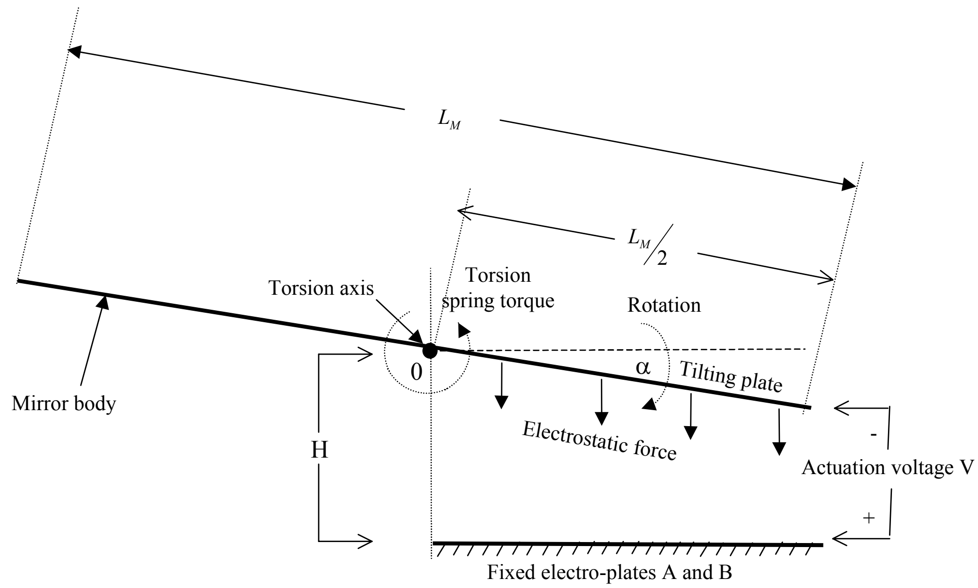

(a) with the horizontal bottom plate

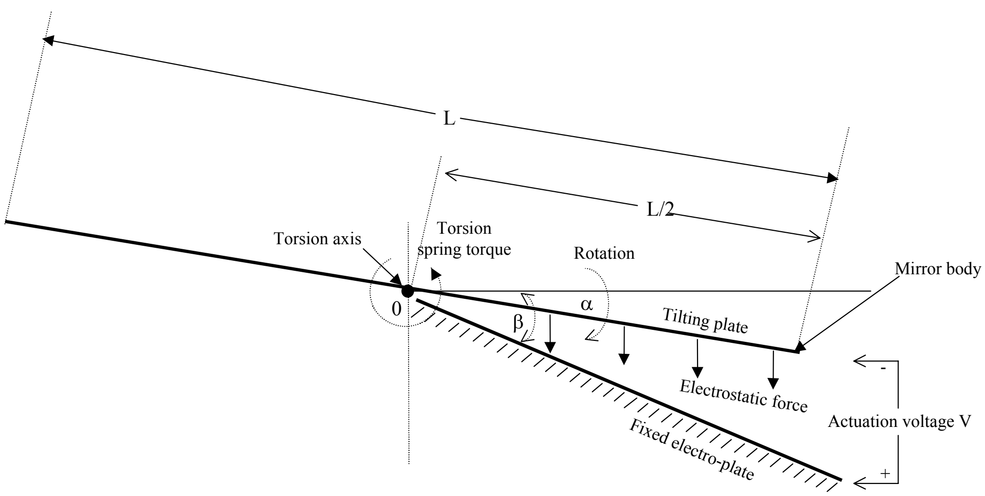

(b) with the fixed bottom plate tilted by angle β

Figure 3-17 The schematics of a MEMS mirror actuator (side view)

Comparing Figure 3-16(a) with Figure 3-3, the similarity is straightforward. We will get the same results for our MEMS mirror actuator as in Section 3.3 for the structure with a horizontal bottom plate. The only difference is the integral upper limit, which is $L = {L_m}/{2}$ here. All the equations in Section 3.3 hold with a replacement of $L = {L_m}/{2}$.

This is the same as the case with Figure 3-16(b). Comparing Figure 3-16(b) with Figure 3-7, the similarity is also straightforward. We will get the same results for our MEMS mirror actuator as in Section 3.4 for the structure with a tilt bottom plate with a fixed tilted angle of β. The only difference is the integral upper limit, which is $L = {L_m}/{2}$ here. All the equations in Section 3.4 hold with a replacement of $L = {L_m}/{2}$. Thus to simplify our analysis of a MEMS mirror actuator system, a half-mirror structure such as the one in Figure 3-7 can be used. We will still use this half-mirror structure to discuss the multi-level bottom plates.

3.6.2 Multi-stage implementation of the optimal tilted bottom plate

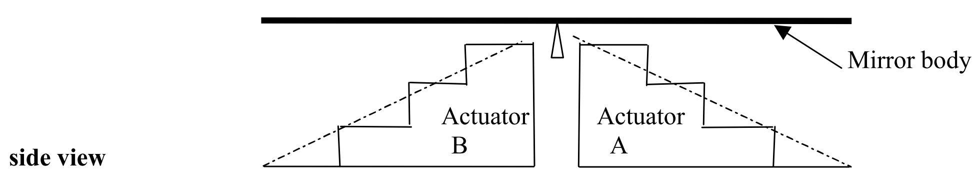

Figure 3-18 Side view of Multi-step approximation of tilted plate actuators

As described in Chapter 2, a real MEMS based mirror system in large channel count optical switch applications normally consists of a large number of mirrors. When considering the implementation of these tilted bottom plates in fabrication, we are facing a difficult task to make such a large quantity of independently tilted plates on a substrate. In order to use the matured planar silicon process technologies widely used in the semiconductor industry today, it is quite natural to consider multi-steps to approximate this tilted bottom surface, as shown in Figure 3-18.

Theoretically, if an infinite numbers of levels are used, the multi-step approximation will be the same as the optimal tilted plate. In practice, only limited levels of multi-steps can be manufactured. As a result, the actuator with a multi-step electro-plate may be different from the optimal tilted plate actuator in voltage requirement. This brings an issue of trade-off between the number of multi-steps used and its voltage requirement. More levels of the bottom plate will achieve better approximation with less required voltage while making the fabrication more complex.

The force and torque analyses of this multi-step bottom plate system, basically, are exactly the same as what was discussed in the Section 3.3 and Section 3.4. The difference will be in the integral limit L and the width W in the formulas such as (3-12) and (3-26), etc., which are determined by the size of the individual electro-plate. However, care must be taken about the fringe effects. In the discussion of Section 3.3 and Section 3.4, the fringe effects have been ignored as the mirror size is large compared with the gap distance or the angular gap. However, when the size of the electro-plates is not much bigger than the gap distance or the angular, the fringe effects can not be ignored any more. Numerical analysis based on Laplace's equation should be pursued. According to Nishiyama [67] , Nemirovosky [68] , there will be an error of about 10%.

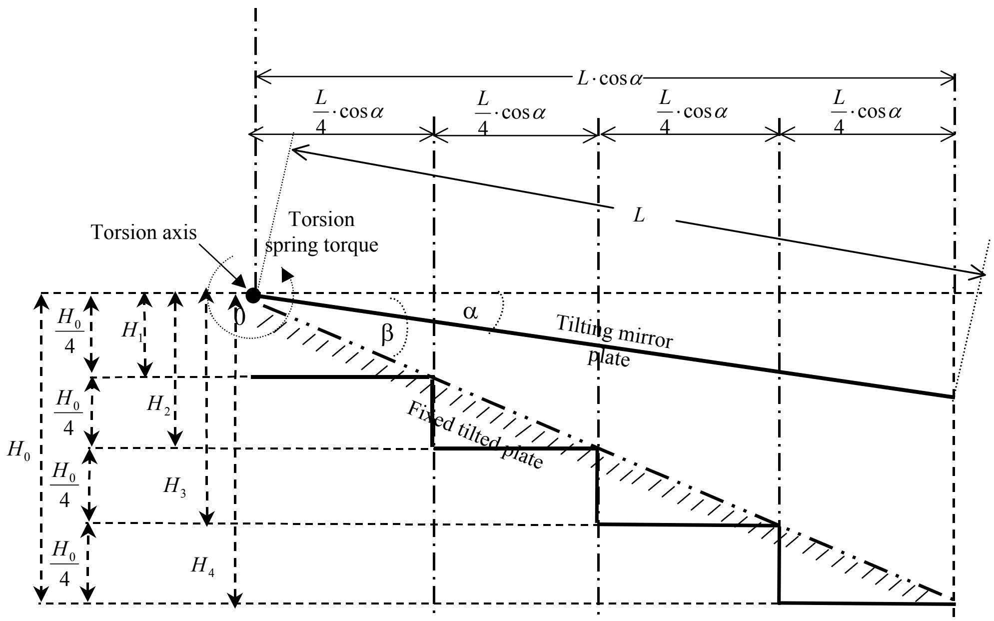

Figure 3-19 Four-stage implementation of an optimal tilted bottom plate

Figure 3-18 is a four-level implementation example. Altogether four stages are used to approximate the tilted bottom plate with an angle of β relative to the horizontal line. The length of each stage is $\frac{L \cdot \cos\alpha}{4}$ and the width of each stage is still W. The distance between each stage is $i \cdot \frac{H_0}{4}$, where i is the sequence number of the stage.

3.7 Conclusions

We have discussed the methodology to develop an optimal plate actuator based on three different configurations of the plate actuator system. By using force or torque analysis at equilibrium status, it is shown that the optimal tilted bottom plate results in the minimum driving voltage required compared with the horizontal bottom plate. In order to fabricate such an optimal tilted bottom plate using planar silicon processes, multi-steps are implemented and a four-stage design is given.

Chapter 4: Transient Analysis

Abstract

The transient response of the top plate movement for the actuator in the optimal plate structure is discussed in this chapter. The transient response equation is developed with consideration of damping effects, especially the squeeze film damping. It is solved both in a numerical way by using PSpice and in an analytical way by linearizing the equation. A comparison is performed between the transient response of this same top plate in the optimal plate structure and that in a standard horizontal plate structure.

4.1 Introduction

After the equilibrium analysis in Chapter 3, the transient analysis of the movement of the top plate in this optimal plate actuator system will be discussed in this chapter. The structure of this chapter is the following: First a system definition is given for this optimal plate structure based on the study in Chapter 3. Then by applying Newton's law for a rotational rigid body on the top plate, a second order differential equation to describe the transient response is developed taking account of damping effects.

In order to solve this non-linear differential equation, an analogous electrical circuit is set up in PSpice using GVALUE components. Based on this analogy, this non-linear equation is solved by a PSpice transient simulation. By using the same analogous concept, a transient response of the top plate of a standard horizontal plate structure is obtained as a comparison to the optimal bottom plate structure. In the last section, since the tilt angle is small, by using linearization of the nonlinear equation, an analytical solution is obtained for the transient response. From this solution, we can directly have the relationship between the applied step voltage and the transient switching time or the damping amplitude.

4.2 System definition

In the actuator system with the optimal bottom plate structure, the bottom plate is fixed. So we describe the transient response of the top plate after there is a voltage applied between the two plates.

To describe the transient response of the top plate, we recall the Newton's law to describe rotation in a rigid body:

$$J \cdot \frac{d^2\alpha}{dt^2} = \sum \tau(t) \tag{4-1}$$

where J is the moment of inertia; α is the angular displacement of J with respect to a frame of reference; τ is the torque applied on J with respect to the same frame of reference. The right side of (4-1) includes all the torque applied on J [61, pages 53-68].

When the top plate rotates along its axis, there are three noticeable rotation toque. One is the torque τ_e due to the electrostatic force, one is the torque τ_m due to the torque spring and the other one τ_B is due to damping effects of the system.

By using (4-1), the transient response of this top plate is:

$$J \cdot \frac{d^2\alpha}{dt^2} = \tau_e + \tau_m + \tau_B \tag{4-2}$$

When writing (4-2), we assume that the top plate is a rigid body and again due to the small size of the whole system, the torque due to gravity force is ignored.

Before we proceed on the study of the transient analysis of the top movable plate in the optimal plate actuator system, the system we are going to study is defined as the following. Its structure is based on the same example of the optimal bottom plate structure, which is given in Figure 3-11. Here we redraw it as Figure 4-1 with the following structure data. W, the width of the top mirror, is 250μm; L, the half length of the mirror, is 125μm; and t , its thickness, is 2μm; γ as labeled is 3μm.

In order to reach a design goal of 8 degrees tilt angle for the top mirror, for such a fixed bottom plate structure, by using (3-37), the optimal angle β can be calculated as the following.

Here, $\delta = \dfrac{\gamma}{\cos\beta}$, $L = 125$, with some design margin, the $\alpha_M = 8.7$ degrees, which is 0.1518 radian.

$$\frac{4 \cdot \alpha_M}{\sin 2(\beta - \alpha_M)} = 1 - \alpha_M \cdot \frac{\tan(\beta - \alpha_M)}{\ln \frac{L \cdot \cos(\beta - \alpha_M) \cdot \cos \beta}{\gamma}} \tag{4-3}$$

Solving (4-3), the optimal angle of β is: $\beta = 0.4839$ radians (or 27.7254 degrees).

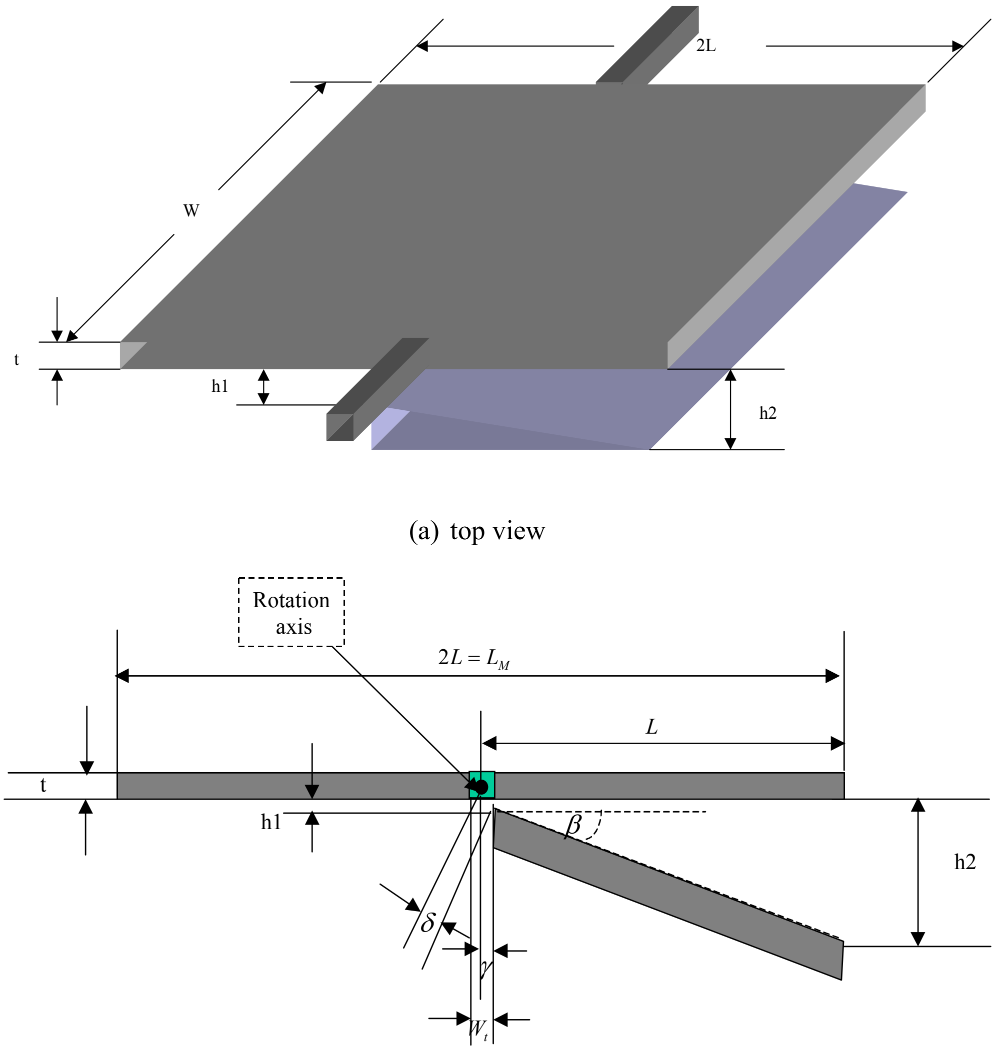

(a) top view

(b) side view

Figure 4-1 The schematic of the system with the optimal bottom plate structure

4.3 The transient equation to describe the top movable plate

For such a system with the optimal structure defined in Figure 4-1, Equation (4-2) applies to its top movable plate. Its electrostatic torque τ_e has been described in Chapter 3 as in Expression (3-30). The mechanical restoring torque τ_m , for a first order of approximation, holds a linear relationship with the angular displacement α. The damping torque τ_B is complex to describe, which includes several factors that contribute to the energy loss during the transient process.

When the plate rotates, there can be acoustic radiation to transfer energy from the mechanical rotation to sound energy and this energy can propagate in the air. The rotation can also introduce the internal friction due to the thermal energy flowing out of the compressed region to the tensile region. In addition, a third factor is the squeeze damping due to the compression of the air gap between the movable top plate the fixed bottom plate. However, this last term contributes to the main energy loss [75] [64] [65]. We will consider this dominant damping in our analysis.

4.3.1. The moment of inertia

With a cube shape, the moment of inertia J for the top plate is:

$$J = \int_{-L}^{L} r^2 \cdot \rho W t dr$$

$$= \rho W t \frac{2 \cdot L^3}{3} \tag{4-4}$$

Where ρ is the density of the top plate; W is the width of the top plate, L is the half-length of the plate; and t is the thickness of the plate.

For this example of the optimal plate structure, we assume that its top plate is made of gold with density ρ, $\rho = 19.3 g/cm^3 = 19.3 \times 10^3 kg/m^3$. When we can put additional structural parameters inside (4-4), the moment of inertia of the plate is

$$J = 19.3 \times 10^3 \cdot \left(250 \times 10^{-6}\right) \cdot \left(2 \times 10^{-6}\right) \cdot \frac{2 \cdot \left(125 \times 10^{-6}\right)^3}{3} \\ = 1.2565 \times 10^{-17} Kg \cdot m^2 \tag{4-5}$$

4.3.2 The electrostatic torque and the mechanical torque

As described in Chapter 3, the torque due to the electrostatic force is expressed in (3-30), which is rewritten here as (4-6)

$$\tau_e = \frac{\varepsilon \cdot W \cdot V^2 \cdot \ln \frac{L \cdot \cos(\beta - \alpha)}{\delta}}{2 \cdot \tan^2(\beta - \alpha)} \tag{4-6}$$

where V is the applied voltage and β is the tilt angle of the bottom plate.

The torque due to spring

$$\tau_m = -k \cdot \alpha \tag{4-7}$$

where k is the mechanical stiffness constant of the torsion spring, which has been discussed in Section 3.5. Here minus sign is taken because this spring torque is always opposite to the moving direction. We use the same method to calculate k as what we did in Chapter 3 and get $k = 3.9031 \times 10^{-9}$ Nm/radian. This is the number that we will use in the following analysis.

4.3.3 The damping torque: squeeze film damping effect

According to Murray [61], the damping torque τ_B is proportional to the angular velocity of J, that is

$$\tau_B = -B \cdot \frac{d\alpha}{dt} \tag{4-8}$$

Here minus sign is taken because friction is always opposite to the moving direction. As stated earlier, though several mechanisms appeared during damping process, most of them are not significant to be considered. The main dominant factor is the squeeze film damping due to the air gap between the rotational top plate and the fixed bottom electrode. In general, the squeeze film damping contains both the air spring effect and energy loss damping effect, between which the dissipative damping is the more important effect [62], [63].

If the roughness of both plates is neglected, according to Chang et al [47], the damping coefficient related to the air squeeze damping for the top plate is:

$$B = \frac{48}{\pi^6 \left(\eta^2 + 4\right)} \frac{\mu_{air} W (2 \cdot L)^5}{h_0^{\ 3}} \tag{4-9}$$

Here again W is the width of the mirror, 2L is the length of the mirror. $\eta = \frac{2 \cdot L}{W}$. μ_{air} is the air viscosity, a variable with the air pressure. At room temperature, when the air pressure is $P_{air} = 1.013 \times 10^5$ Pa (1 atm), $\mu_{air} = 1.79 \times 10^{-5}$ kg/ m^3 . h_0 is the initial average air gap distance between the top plate and the fixed bottom plate. Here the there is an initial angle β between the fixed bottom plate and the movable top plate. $\beta = 0.4839$ radians. Initially, the air gap distance is separately h_1 and h_2 at the two ends of the plates:

$$h_1 = \gamma \tan \beta = 3 \cdot \tan 0.4839 = 1.5767\ \mu\text{m} \tag{4-10}$$

$$h_2 = L \tan \beta = 125 \cdot \tan 0.4839 = 65.6972\ \mu\text{m} \tag{4-11}$$

So

$$h_0 = \frac{h_1 + h_2}{2} = 33.6369\ \mu\text{m} \tag{4-12}$$

Chang et al [47] also mentioned to consider the roughness factor σ in (4-8). In our case here, both the top and the bottom plate are considered to be a smooth surface.

$$\eta = \frac{2 \cdot L}{W} = \frac{2 \cdot 125}{250} = 1 \tag{4-13}$$

Putting the structure parameters of the example actuator in (4-9), the damping coefficient for this tilted fixed bottom plate B_{tilted} is

$$B_{tilted} = 1.1466 \times 10^{-15} \tag{4-14}$$

Here we assume a constant damping coefficient during the transient periods. We will use a time variable damping coefficient in Chapter 5.

4.3.4 The transient equation to describe the top plate rotation

Combined with equation (4-2), (4-6), (4-7) and (4-8) in (4-1):

$$J \cdot \frac{d^2\alpha}{dt^2} = \tau_e + \tau_m + \tau_B$$

$$= \frac{\varepsilon \cdot W \cdot V^2 \cdot \ln \frac{L \cdot \cos(\beta - \alpha)}{\delta}}{2 \cdot \tan^2(\beta - \alpha)} - k \cdot \alpha - B \frac{d\alpha}{dt} \tag{4-15}$$

That is:

$$J \cdot \frac{d^2\alpha}{dt^2} + B \frac{d\alpha}{dt} + k \cdot \alpha - \frac{\varepsilon \cdot W \cdot V^2 \cdot \ln \frac{L \cdot \cos(\beta - \alpha)}{\delta}}{2 \cdot \tan^2(\beta - \alpha)} = 0 \tag{4-16}$$

If we put all the structure data of the example, such as W, L, k and t, etc into (4-16) and assume that the applied voltage is a step function at time zero, then (4-16) becomes:

$$\frac{d^2\alpha}{dt^2} + 91.2532 \cdot \frac{d\alpha}{dt} + 3.1063 \times 10^8 \cdot \alpha - 88.0812 \cdot V^2 \cdot \frac{\ln(36.8828 \cdot \cos(0.4839 - \alpha))}{(\tan(0.4839 - \alpha))^2} = 0 \tag{4-17}$$

Equation (4-16) is the transient equation to describe the transient response of the top plate. It is a nonlinear differential equation due to the term involved with the electrostatic torque. Its analytical solution is not easy to get. In order to solve (4-16), two approaches are illustrated here. One is to use PSpice simulation directly with an analogous circuit; the other is to linearize (4-16) to develop an analytical expression.

4.4 Transient response by simulation with PSpice

In this section, we solve (4-16) by PSpice using an analogous circuit. We first define a circuit with GVALUE components. Then a second order differential equation about one specific node voltage will be derived, which shares the same format as (4-16). Based on this analogy, if we replace the variables, the transient response for this circuit should be the same as the transient response describe in (4-16). Thus, PSpice simulation tool can be utilized to solve (4-16) and thus the transient response of the top plate is obtained.

4.4.1 An analogous circuit with GVALUE components

GVALUE is a two-port circuit component in PSpice. The output is voltage and the input is the current. There is a defined function between the output voltage and the input current. The analogous circuit is shown in Figure 4-2. It has two GVALUE components, one G component, two capacitors and two resistors. Here the currents flowing through the resistors have been ignored, because the resistors have the value of 10G ohms.

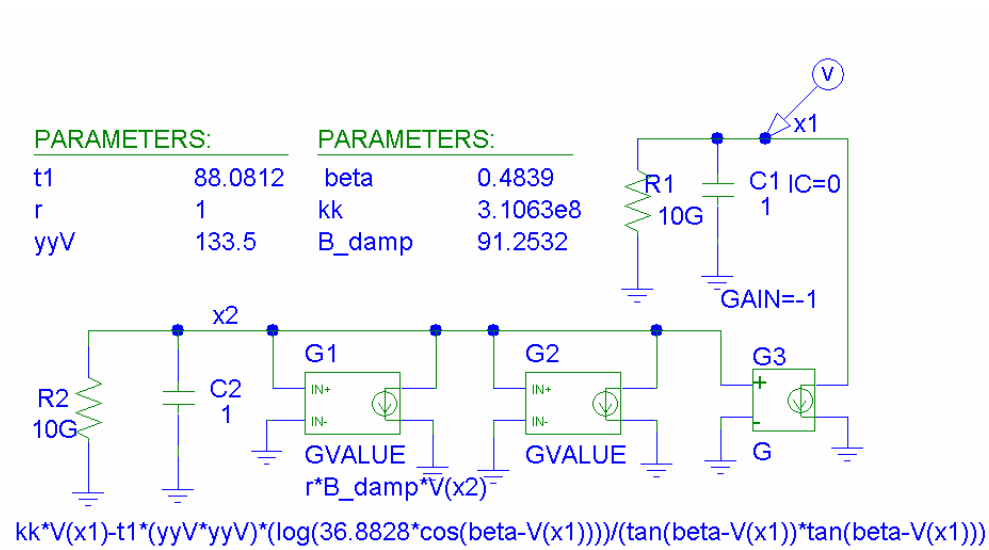

Figure 4-2 An analogous circuit to calculate the transient response

As shown in Figure 4-2, the voltage on node x1 referenced to ground is labeled as $V(x1)$; the voltage on node x2 is labeled as $V(x2)$. Capacitor $C1 = 1$ F with 0 initial charge. Capacitor $C2 = 1$ with 0 initial charge. R1 and R2 are there for convergence purpose, both 10G ohms. G1 and G2 are both GVALUE components, whose current is controlled by the GVALUE expression shown. G3 is a normal ideal voltage controlled current source with the gain of –1.

For G1, its GVALUE expression is

$$i_{G1} = r \cdot B\_damp \cdot V(x2) \tag{4-18}$$

where $r = 1$, and $B\_damp = 91.2532$

For G2, its GVALUE expression is

$$i_{G2} = kk \cdot V(x1) - t1 \cdot V^2 \frac{\ln\left(36.8828 \cdot \cos(\beta - V(x1))\right)}{\left(\tan(\beta - V(x1))\right)^2} \tag{4-19}$$

where $kk = 3.1063 \times 10^8$, $t1 = 88.0812$, $beta = \beta = 0.4839$

For G3, its G value is

$$i_{G3} = -V(x2) \tag{4-20}$$

For C1,

$$i_{C1} = C1 \frac{dV(x1)}{dt} = \frac{dV(x1)}{dt} \tag{4-21}$$

where $C1 = 1$

For C2,

$$i_{C2} = C2 \frac{dV(x2)}{dt} = \frac{dV(x2)}{dt} \tag{4-22}$$

where $C2 = 1$

After we have defined the parameters of the components in Figure 4-2, we will proceed to show that the equation to describe V(x1), which is a second order differential equation, has the same format as (4-16).

4.4.2 The second order differential equation for the node voltage V(x1)

In Figure 4-2, for Node x1, ignoring the current flowing over R1, then

$$i_{C1} = -i_{G3} \tag{4-23}$$

Combined (4-23), (4-20) and (4-21), then

$$V(x2) = \frac{dV(x1)}{dt} \tag{4-24}$$

For node x2, the current flowing to the IN+ pin of G1, G2 and G3 is zero according to the GVALUE model. Again if ignoring the current flowing over R2, then

$$i_{C2} = -i_{G1} - i_{G2} \tag{4-25}$$

Combined (4-25), (4-18), (4-19) and (4-22), then

$$\begin{aligned} i_{C2} &= \frac{dV(x2)}{dt} \\ &= -r \cdot B\_damp \cdot V(x2) - kk \cdot V(x1) + t1 \cdot V^2 \cdot \frac{\ln\left(36.8828 \cdot \cos(\beta - V(x1))\right)}{\left(\tan(\beta - V(x1))\right)^2} \end{aligned} \tag{4-26}$$

Combined (4-24), (4-26) and the parameters shown in Figure 4.2,

$$\frac{d^2V(x1)}{dt^2} + 91.2532 \cdot \frac{dV(x1)}{dt} + 3.1063 \times 10^8 \cdot V(x1) - 88.0812 \cdot V^2 \cdot \frac{\ln\left(36.8828 \cdot \cos(0.4839 - V(x1))\right)}{\left(\tan(0.4839 - V(x1))\right)^2} = 0$$

(4-27)

The similarity between (4-27) and (4-17) is apparent, as long as we set

$V(x1) = \alpha$ (4-28)

That means that the transient response of the system represented in (4-27) is the same as the transient response represented in (4-16) or (4-17). Because PSpice can be used to simulate the circuit described by (4-27), the same result will be obtained for the mechanical system described by (4-16) or (4-17), as long as by using a variable change $V(x1) = \alpha$.

Figure 4-3 is the transient response according to the circuit shown in Figure 4-2. In Figure 4-3(a), V is100V. In Figure 4-3(b) are the transient settling responses when V=130V, 90V and 50V separately. Figure 4-3(b) shows that the higher the voltage applied, the higher the damping amplitude is. These analyses are the same to our mechanic system described by (4-16), when $V(x1) = \alpha$.

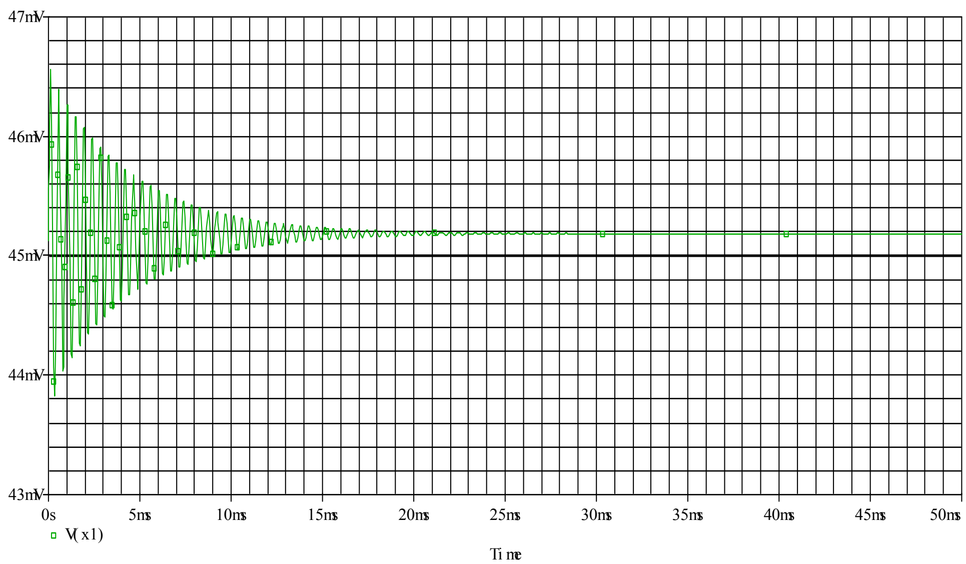

(a) when V=100V

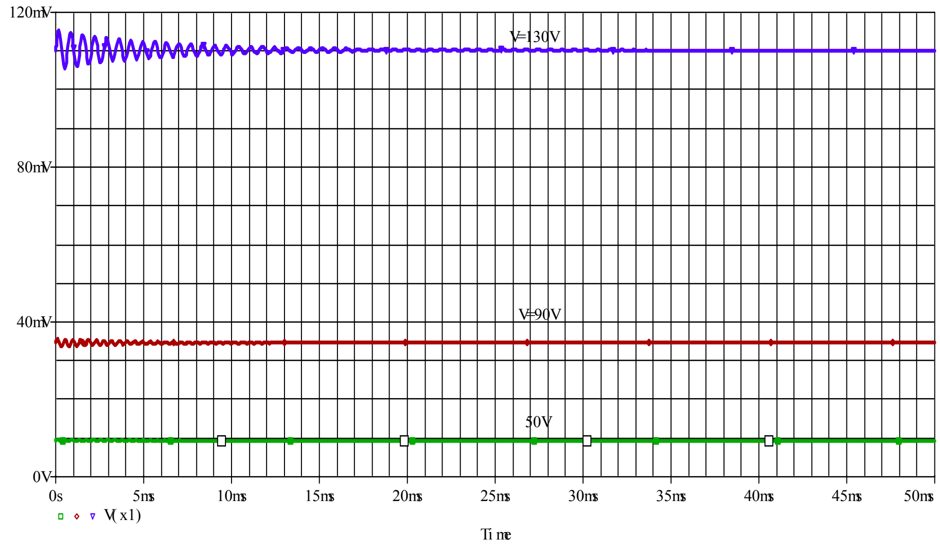

(b) when V=50V, 90V and 130V

Figure 4-3 Transient response for the analogous circuit

4.5 Comparison between the transient response in a horizontal bottom plate actuator and that in the optimal bottom plate actuator

In this section, we will compare the transient response of the top plate in the actuator between the tilted bottom plate structure and the horizontal bottom plate structure. Both these actuators have the same top plates. The schematic of the actuator with the horizontal plate structure is shown in Figure 4-4. The top movable plate is the same in both Figure 4-1 and Figure 4-4. The only difference is the bottom plate structure.

Using the same analogue method, we will begin the comparison by defining the horizontal bottom plate actuator system as shown in Figure 4-4.

This actuator system shown in Figure 4-4 is based on the same example of the horizontal actuator structure, which is given in Figure 3-4 of Chapter 3. Here we redraw it as Figure 4-4 with the following structure data. W the width of the top mirror is 250μm; L the half length of the mirror is 125μm; and t its thickness is 2μm; δ as labeled is 3μm. To obtain a tilt angle of 8 degrees, H is 41.600μm according to Equation (3-23) with $\alpha_M = 8.7$ degrees.

To analyze the transient response of the top plate shown in Figure 4-4, Equation (4-2) again is used. Because both top plates are the same in Figure 4-1 and Figure 4-4, J in Equation (4-7) holds here too. The same mechanical spring torque holds here as in (4-7). $k = 3.9031 \times 10^{-9}$ Nm/radian. As described in Chapter 3, the torque due to the electrostatic force is expressed in (3-17).

For damping torque, (4-8) and (4-9) hold also. However, there is a different damping coefficient B due to the different shape of the horizontal bottom plate between the two structures. In the horizontal bottom plate actuator system, h_0 is the initial air gap distance between the top plate and the fixed bottom plate, which is a constant H. Putting the structure parameters in (4-9), the damping coefficient for a fixed horizontal bottom plate B_{flat} is

$$B_{flat} = 6.0615 \times 10^{-16} \text{ N-s/m} \qquad (4\text{-}29)$$

It is apparent B_{flat} is smaller than B_{tilted} in (4-14)

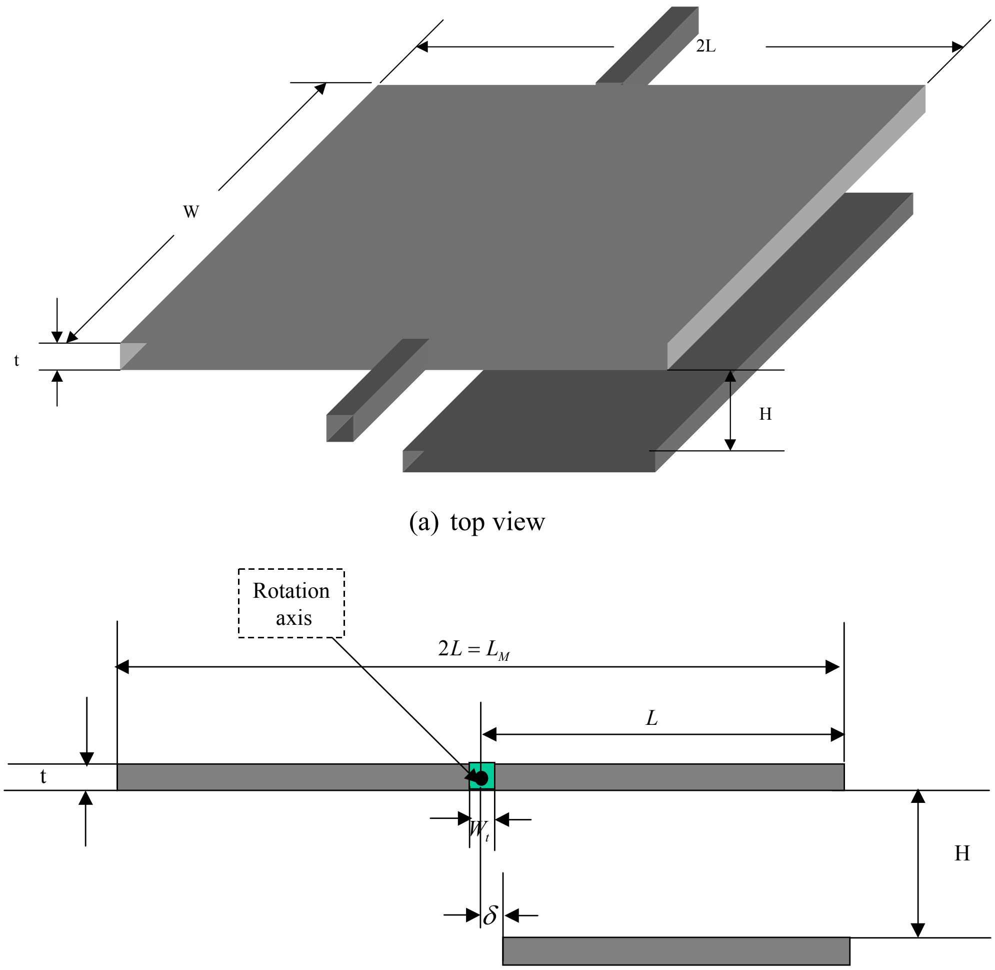

(a) top view

(b) side view

Figure 4-4 A plate actuator with a horizontal bottom plate structure

Combining with Equation (4-2), (3-17), (4-7) and (4-8) in (4-1):

$$J \cdot \frac{d^2\alpha}{dt^2} = \tau_e + \tau_m + \tau_B$$

$$= \frac{\varepsilon \cdot W \cdot V^2 \cdot \left(\ln \frac{H - L \cdot \sin\alpha}{H} + \frac{H}{H - L \cdot \sin\alpha} - 1 \right)}{2 \cdot \tan^2 \alpha} - k \cdot \alpha - B_{flat} \frac{d\alpha}{dt}$$

That is:

$$J \cdot \frac{d^2\alpha}{dt^2} + B\frac{d\alpha}{dt} + k \cdot \alpha - \frac{\varepsilon \cdot W \cdot V^2 \cdot \left(\ln \frac{H - L \cdot \sin\alpha}{H} + \frac{H}{H - L \cdot \sin\alpha} - 1 \right)}{2 \cdot \tan^2 \alpha} = 0 \qquad (4\text{-}30)$$

If we put all the structure data, such as W, L, k and t, into (4-30) and assume that the applied voltage is a step function at time zero, then (4-30) becomes:

$$\frac{d^2\alpha}{dt^2} + 48.2410 \cdot \frac{d\alpha}{dt} + 3.1063 \times 10^8 \cdot \alpha - 88.0812 \cdot V^2 \cdot \frac{\ln \frac{41.6 - 125 \cdot \sin\alpha}{41.6} + \frac{125 \cdot \sin\alpha}{41.6 - 125 \cdot \sin\alpha}}{\tan^2\alpha} = 0$$

(4-31)

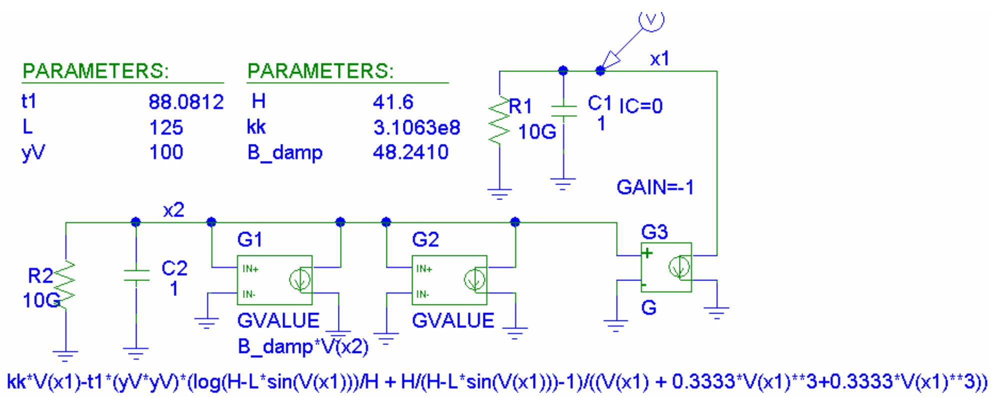

(a) An analogous circuit to describe the transient response of a horizontal bottom plate actuator system

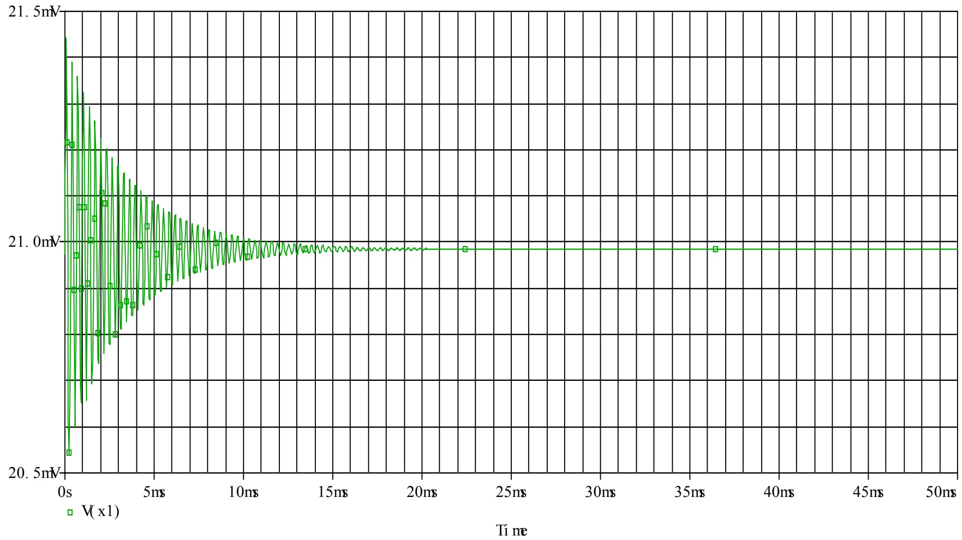

(b) PSpice transient response when V=100V

Figure 4-5 PSpice transient response with an analogous circuit to the horizontal bottom plate actuator system

Equation (4-30) is a nonlinear differential equation also. Its analytical solution is not easy to get. Again we use an analogous circuit and its corresponding PSpice simulation to obtain the result. This analogous circuit is shown in Figure 4-5 (a). Due to the convergence problem involved in PSPICE, the term $\tan\alpha$ is replaced by the two Taylor expansion terms, this is $\tan\alpha = \alpha + \frac{\alpha^3}{3}$. The transient response at V=100V is shown in Figure 4-5(b). Compared with Figure 4-5(b) and Figure 4-3(a). They are almost the same.

4.6 Transient analysis using linearization approximation

In the previous section, we obtain the transient response using an analogous electrical circuit. However, this methodology does not release any detailed analytical discussion, such as the impact of the mechanical structure parameters on the transient responses. In this section, we will focus on an analytical solution to the transient equation (4-16). Linearization is applied on the equation, specifically on the term with electrostatic torque τ_e, which has the nonlinear nature. In this way, analytical discussion can be performed. Because, as mention in Chapter 2, in large channel count optical switch applications, the maximum tilt angle of the top plate is somewhat around 8 degree, which is 0.1517 radians, so this linearization approximation around $\alpha = 0$ degree is reasonable in practice.

For convenience, we rewrite (4-16) here.

$$J \cdot \frac{d^2\alpha}{dt^2} + B\frac{d\alpha}{dt} + k \cdot \alpha - \frac{\varepsilon \cdot W \cdot V^2 \cdot \ln \dfrac{L \cdot \cos(\beta - \alpha)}{\delta}}{2 \cdot \tan^2(\beta - \alpha)} = 0 \qquad \text{(4-16)}$$

Because ε, W and V (if we assume a step voltage function) are in simple format, the term needs linearization is the last term as

$$\frac{\ln\frac{L\cdot\cos(\beta-\alpha)}{\delta}}{\tan^2(\beta-\alpha)}=\frac{\ln\left(\frac{L}{\delta}\cdot\cos(\beta-\alpha)\right)}{\frac{\sin^2(\beta-\alpha)}{\cos^2(\beta-\alpha)}}$$

$$=\frac{\ln\left(\frac{L}{\delta}\cdot(\cos\beta\cos\alpha+\sin\beta\sin\alpha)\right)}{\sin^2(\beta-\alpha)}\cdot\cos^2(\beta-\alpha)$$

$$=\frac{\ln\left(\frac{L}{\delta}\cdot(\cos\beta\cos\alpha+\sin\beta\sin\alpha)\right)}{(\sin\beta\cos\alpha-\cos\beta\sin\alpha)^2}\cdot(\cos\beta\cos\alpha+\sin\beta\sin\alpha)^2 \tag{4-30}$$

As α is sufficiently small as in our case here $\alpha \le 10$ degrees, which is about 0.1745 radians as discussed in Chapter 2, we can use the following approximation:

$$\cos\alpha \approx 1-\frac{1}{2}\cdot\alpha^2 \tag{4-31}$$

$$\sin\alpha \approx \alpha \tag{4-32}$$

Then the right side of (4-30) becomes:

$$=\frac{\ln\left(\frac{L}{\delta}\cdot\left(\cos\beta\cdot\left(1-\frac{\alpha^2}{2}\right)+\sin\beta\cdot\alpha\right)\right)}{\left(\sin\beta\cdot\left(1-\frac{\alpha^2}{2}\right)-\cos\beta\cdot\alpha\right)^2}\cdot\left(\cos\beta\cdot\left(1-\frac{\alpha^2}{2}\right)+\sin\beta\cdot\alpha\right)^2 \tag{4-33}$$

neglecting the higher orders, (4-33) becomes

$$=\frac{\ln\left(\frac{L}{\delta}\cdot(\cos\beta+\sin\beta\cdot\alpha)\right)}{(\sin\beta-\cos\beta\cdot\alpha)^2}\cdot(\cos\beta+\sin\beta\cdot\alpha)^2$$

$$=\frac{\ln\left(\frac{L}{\delta}\cdot\cos\beta\left(1+\frac{\sin\beta}{\cos\beta}\cdot\alpha\right)\right)}{\sin^2\beta\left(1-\frac{\cos\beta}{\sin\beta}\cdot\alpha\right)^2}\cdot\cos^2\beta\left(1+\frac{\sin\beta}{\cos\beta}\cdot\alpha\right)^2$$

$$
=\frac{\ln\left(\frac{L}{\delta}\cdot\cos\beta\right)+\ln\left(1+\frac{\sin\beta}{\cos\beta}\cdot\alpha\right)}{\sin^2\beta\left(1-\frac{\cos\beta}{\sin\beta}\cdot\alpha\right)^2}\cdot\cos^2\beta\left(1+\frac{\sin\beta}{\cos\beta}\cdot\alpha\right)^2 \tag{4-34}
$$

Recall that if x is sufficiently small, using:

$$
\ln(1+x)\approx x \tag{4-35}
$$

$$
\frac{1}{(1-x)^2}\approx 1+2x \tag{4-36}
$$

$$
(1+x)^2\approx 1+2x \tag{4-37}
$$

(4-34) becomes:

$$
\begin{aligned}
&\approx\frac{\ln\left(\frac{L}{\delta}\cdot\cos\beta\right)+\frac{\sin\beta}{\cos\beta}\cdot\alpha}{\sin^2\beta}\cdot\cos^2\beta\left(1+2\cdot\frac{\sin\beta}{\cos\beta}\cdot\alpha\right)\cdot\left(1+2\cdot\frac{\cos\beta}{\sin\beta}\cdot\alpha\right)\\
&=\frac{\cos^2\beta}{\sin^2\beta}\cdot\left[\ln\left(\frac{L}{\delta}\cdot\cos\beta\right)+\left(\frac{\sin\beta}{\cos\beta}\cdot\alpha\right)\right]\cdot\left(1+2\cdot\frac{\cos\beta}{\sin\beta}\cdot\alpha+2\cdot\frac{\sin\beta}{\cos\beta}\cdot\alpha+4\cdot\alpha^2\right)\\
&\approx\frac{\cos^2\beta}{\sin^2\beta}\cdot\left[\ln\left(\frac{L}{\delta}\cdot\cos\beta\right)+\left(\frac{\sin\beta}{\cos\beta}\cdot\alpha\right)\right]\cdot\left(1+2\cdot\frac{\cos\beta}{\sin\beta}\cdot\alpha+2\cdot\frac{\sin\beta}{\cos\beta}\cdot\alpha\right)\\
&\approx\frac{\cos^2\beta}{\sin^2\beta}\cdot\left[\ln\left(\frac{L}{\delta}\cdot\cos\beta\right)\cdot\left(1+2\cdot\frac{\cos\beta}{\sin\beta}\cdot\alpha+2\cdot\frac{\sin\beta}{\cos\beta}\cdot\alpha\right)+\left(\frac{\sin\beta}{\cos\beta}\cdot\alpha\right)\left(1+2\cdot\frac{\cos\beta}{\sin\beta}\cdot\alpha+2\cdot\frac{\sin\beta}{\cos\beta}\cdot\alpha\right)\right]\\
&\approx\frac{\cos^2\beta}{\sin^2\beta}\cdot\left[\ln\left(\frac{L}{\delta}\cdot\cos\beta\right)+\alpha\cdot\left[\left(2\frac{\cos\beta}{\sin\beta}+2\cdot\frac{\sin\beta}{\cos\beta}\right)\cdot\ln\left(\frac{L}{\delta}\cdot\cos\beta\right)+\frac{\sin\beta}{\cos\beta}\right]\right]\\
&\approx\frac{\cos^2\beta}{\sin^2\beta}\cdot\left[\ln\left(\frac{L}{\delta}\cdot\cos\beta\right)+\alpha\cdot\left[\left(\frac{2}{\sin\beta\cos\beta}\right)\cdot\ln\left(\frac{L}{\delta}\cdot\cos\beta\right)+\frac{\sin\beta}{\cos\beta}\right]\right]
\end{aligned} \tag{4-38}
$$

Assume that the applied voltage is a step function at time zero. With (4-38), Equation (4-16) becomes:

$$J \cdot \frac{d^2\alpha}{dt^2} + B\frac{d\alpha}{dt} + k \cdot \alpha -$$
$$\frac{\varepsilon \cdot W \cdot V^2}{2} \cdot \frac{\cos^2\beta}{\sin^2\beta} \cdot \left[\ln\left(\frac{L}{\delta} \cdot \cos\beta\right) + \alpha \cdot \left[\left(\frac{2}{\sin\beta\cos\beta}\right) \cdot \ln\left(\frac{L}{\delta} \cdot \cos\beta\right) + \frac{\sin\beta}{\cos\beta} \right]\right] = 0$$
(4-39)

That is:

$$J \cdot \frac{d^2\alpha}{dt^2} + B\frac{d\alpha}{dt} +$$
$$\alpha \cdot \left[k - \frac{\varepsilon \cdot W \cdot V^2}{2} \cdot \frac{\cos^2\beta}{\sin^2\beta} \cdot \left(\left(\frac{2}{\sin\beta\cos\beta}\right) \cdot \ln\left(\frac{L}{\delta} \cdot \cos\beta\right) + \frac{\sin\beta}{\cos\beta} \right)\right] = \tag{4-40}$$
$$\frac{\varepsilon \cdot W \cdot V^2}{2} \cdot \frac{\cos^2\beta}{\sin^2\beta} \cdot \left[\ln\left(\frac{L}{\delta} \cdot \cos\beta\right)\right]$$

From (4-40), we can observe the "spring softness" effect as mentioned in Senturia [40].

(4-40) can be written

$$\frac{d^2\alpha}{dt^2} + f1\frac{d\alpha}{dt} + \alpha \cdot f2 = f3 \tag{4-41}$$

Using the notation:

$$f1 = \frac{B}{J} = 2\gamma \tag{4-42}$$

$$f2 = \frac{1}{J}\left[k - \frac{\varepsilon \cdot W \cdot V^2}{2} \cdot \frac{\cos^2\beta}{\sin^2\beta} \cdot \left(\left(\frac{2}{\sin\beta\cos\beta}\right) \cdot \ln\left(\frac{L}{\delta} \cdot \cos\beta\right) + \frac{\sin\beta}{\cos\beta} \right)\right] = {\omega_0}^2$$
(4-43)

$$f3 = \frac{1}{J} \cdot \frac{\varepsilon \cdot W \cdot V^2}{2} \cdot \frac{\cos^2\beta}{\sin^2\beta} \cdot \left[\ln\left(\frac{L}{\delta} \cdot \cos\beta\right)\right] \tag{4-44}$$

Where β is selected as in Chapter 3 to give the optimal angle of the bottom plate.

In (4-43), because the last term after k is always greater than 0, so

$$\frac{k}{J} > f2 = \frac{1}{J}\left[k - \frac{\varepsilon \cdot W \cdot V^2}{2} \cdot \frac{\cos^2 \beta}{\sin^2 \beta} \cdot \left(\left(\frac{2}{\sin\beta\cos\beta}\right) \cdot \ln\left(\frac{L}{\delta} \cdot \cos\beta\right) + \frac{\sin\beta}{\cos\beta}\right)\right] > 0$$

(4-45)

The Laplace transform of Equation (4-41) is

$$s^2 + f1 \cdot s + f2 \cdot = 0 \tag{4-46}$$

$$s_{1,2} = -\frac{f1}{2} \pm \frac{1}{2}\sqrt{f_1^2 - 4f_1 f_2}$$

$$= -\frac{B}{2J} \pm \frac{1}{2}\sqrt{\frac{B^2}{J^2} - 4\frac{1}{J}\left[k - \frac{\varepsilon W \cdot V^2}{2}\frac{\cos^2\beta}{\sin^2\beta}\left(\frac{2}{\sin\beta\cos\beta} \cdot \ln\left(\frac{L \cdot \cos\beta}{\delta}\right) + \frac{\sin\beta}{\cos\beta}\right)\right]}$$

$$= -\gamma \pm \sqrt{\gamma^2 - \omega_0^{\ 2}} \tag{4-47}$$

The solution to (4-41) depends on the relation between γ and ω_0. As the damping torque associated with the squeeze damping effect, which is expressed in (4-16), is always small in magnitude compared with the electrostatic torque, γ is a very small number compared with ω_0. Then the solution to (4-41) is

$$\alpha = e^{-\gamma t}\left[A_1 \cos\left(\sqrt{\omega_0^{\ 2} - \gamma^2}\, t + \phi\right)\right] + \frac{f3}{\omega_0^{\ 2}} \tag{4-48}$$

where A_1 and ϕ are constants determined by the initial conditions, which is

$\left.\frac{d\alpha}{dt}\right|_{t=0} = 0$ and $\alpha|_{t=0} = 0$. Also denote

$$\bar{\alpha} = \frac{f3}{\omega_0^{\ 2}} \text{ and } \omega = \sqrt{\omega_0^{\ 2} - \gamma^2} \tag{4-49}$$

These result in

$$\cos\phi = \frac{\omega}{\omega_0} = \frac{\sqrt{\omega_0^2 - \gamma^2}}{\omega_0} \tag{4-50}$$

$$A_1 = -\frac{\omega_0}{\omega}\overline{\alpha} \tag{4-51}$$

$\overline{\alpha}$ is the equilibrium angular displacement for the top plate and ω is the damping oscillator frequency. Then (4-48) becomes

$$\alpha(t) = A_1 e^{-\gamma t}\left(\cos(\omega t + \phi)\right) + \overline{\alpha} \tag{4-52}$$

Using the system parameters in the example, (4-51) becomes

$$A_1 = -\frac{\frac{\varepsilon W \cdot V^2}{2}\frac{\cos^2\beta}{\sin^2\beta}\cdot\ln\left(\frac{L\cos\beta}{\delta}\right)}{\sqrt{J\left(k - \frac{\varepsilon W \cdot V^2}{2}\frac{\cos^2\beta}{\sin^2\beta}\cdot\left[\frac{2}{\sin\beta\cos\beta}\cdot\ln\left(\frac{L\cos\beta}{\delta}\right) + \frac{\sin\beta}{\cos\beta}\right]\right)}}\cdot \frac{1}{\sqrt{\frac{1}{J}\left(k - \frac{\varepsilon W \cdot V^2}{2}\frac{\cos^2\beta}{\sin^2\beta}\cdot\left[\frac{2}{\sin\beta\cos\beta}\cdot\ln\left(\frac{L\cos\beta}{\delta}\right) + \frac{\sin\beta}{\cos\beta}\right]\right) - \frac{B^2}{4J^2}}} \tag{4-53}$$

We can put the inertia moment J from (4-4) and damping coefficient B from (4-9) in (4-53)

$$A_1 = -\frac{\frac{\varepsilon W \cdot V^2}{2}\frac{\cos^2\beta}{\sin^2\beta}\cdot\ln\left(\frac{L\cos\beta}{\delta}\right)}{\sqrt{\frac{2\rho WtL^3}{3}\left(k - \frac{\varepsilon W \cdot V^2}{2}\frac{\cos^2\beta}{\sin^2\beta}\cdot\left[\frac{2}{\sin\beta\cos\beta}\cdot\ln\left(\frac{L\cos\beta}{\delta}\right) + \frac{\sin\beta}{\cos\beta}\right]\right)}}\cdot \left(\frac{3}{2\rho WtL^3}\left(k - \frac{\varepsilon W \cdot V^2}{2}\frac{\cos^2\beta}{\sin^2\beta}\cdot\left[\frac{2}{\sin\beta\cos\beta}\cdot\ln\left(\frac{L\cos\beta}{\delta}\right) + \frac{\sin\beta}{\cos\beta}\right]\right) - \left(\frac{3}{4\rho WtL^3}\frac{48\cdot\mu_{air}W\cdot(2L)^5}{\pi^6\left(\left(\frac{2L}{W}\right)^2 + 4\right)h_0^3}\right)^2\right)^{\frac{-1}{2}} \tag{4-54}$$

Equation (4-53) releases the relationship between the oscillating amplitude A_1 and the mechanical structure data, such as β. L,t,W, ρ, of the system described in Figure 4-1.

The squeeze damping results from Chang [47] is used in getting this relationship. For example, in Figure 4-6, we show the relationship between A_1 and L. The relationship between $\overline{\alpha}$ and L is also plotted for comparison.

Three points are emphasized here in Figure 4-6. First is that A_1 and $\overline{\alpha}$ is almost the same. In (4-50), as γ is pretty small compared to ω_0, we will expect that A_1 and $\overline{\alpha}$ is almost the same. This is confirmed in Figure 4-6. The red line is the relationship between $\overline{\alpha}$ and L while the blue line is the relationship between A_1 and L. They coincide with each other. Second, as $\overline{\alpha}$ is the equilibrium tilt angular position of the top movable plate, it increases with the increase of the applied voltage until the pull-in point is reached. This implies that the higher applied voltage results in higher damping oscillating and we have to pay for larger equilibrium tilt angle.

Third, it is observed in Figure 4-6 that in the structure as in Figure 4-1, A_1 increases when L increases, which implies for the same applied voltage, a bigger length will result in bigger tilt angle of the top plate. This agrees with the discussion in Chapter 1, where larger area of the electrode plate, which is the multiple of L and W, results in lower driving voltage. Table 4-1 is the data used to obtain Figure 4-8.

The top plate width W=250μm, the thickness t =2μm
The top plate is made of gold, with density of 19.3×10^3 kg/m^3
The average gap between the top plate and bottom plate is 33.6369μm
The air viscosity at 1 (atm) air pressure is 1.79×10^{-5} kg/ m^3
The bottom fixed plate has angle $\beta = 0.4839$ radian, with $\delta = 3/\cos\beta = 3.891$ μm
Applied voltage is 50V

Table 4-1 Parameters used to evaluate the transient responses of the top plate.

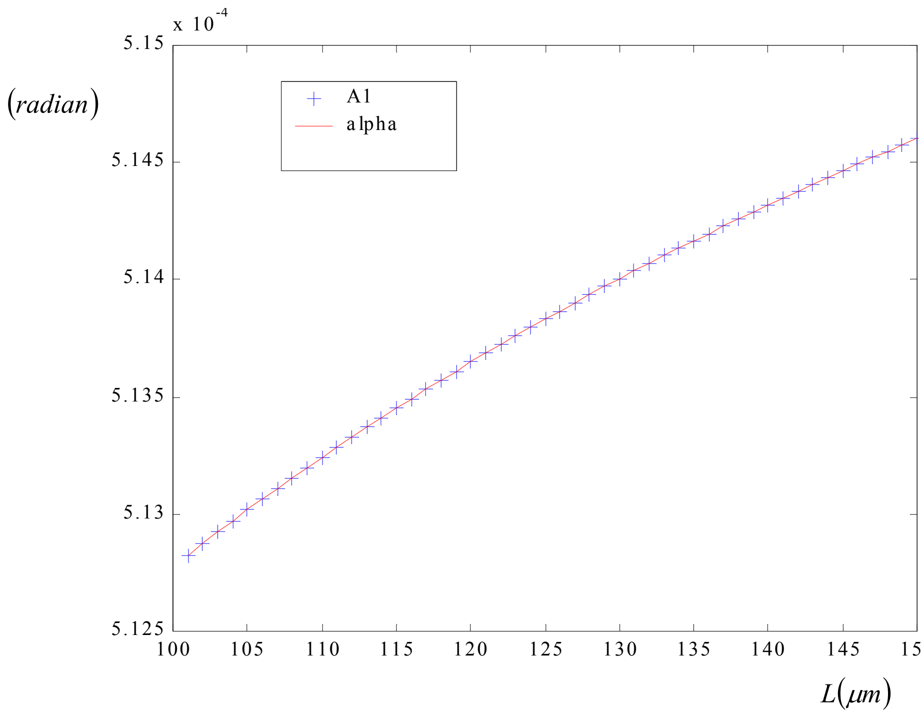

Figure 4-6 The relationship between the damping amplitude of and the length of the top plate

4.7 Conclusions

In this chapter, we have analyzed the transient response of the top plate in the optimal plate actuator system introduced in Chapter 3. The squeeze film damping effect is considered to be dominant. A second order differential equation is set up according to Newton's law. It is solved by an analogous circuit with GVALUE components. We have compared the transient responses of the top plate in an actuator system between the case with our optimal bottom-plate structure and the case with standard horizontal bottom-plate structure. Using linearization approximation to this transient equation, we are able to give an analytic solution. A spring softness effect is observed after an analytical solution is obtained. When a step voltage is applied, the damping oscillation amplitude is proportional to the top plate's final equilibrium position, and the switching time is determined by the damping coefficient. These will help a system designer to trade off between the system parameters to achieve the design goal.

Chapter 5: Stability and Control

Abstract

In this chapter, we study the stability and control of the actuator system with the optimal plate structure. After the state equations are introduced, the stability of the system is discussed. Then two control methodologies to improve the system performance are discussed. In order to implement them, a feedback architecture using a sensing bridge circuit with a position sensing capacitor is introduced. A high voltage actuating circuit is introduced. A design example to implement this circuit is presented with a design analysis. Using a shift register, a modular embedded system is introduced to achieve scalability.

5.1 Introduction

As mentioned in Chapter 2, there are two main objectives for MEMS mirror control. One is to make the mirror tilt to the desired angle as soon as possible after the receipt of the switching command; another is to keep the mirror stable after it has reached its desired angular position until the next switching command. To achieve these two objectives, we study optimal control theory in this chapter.

For our optimal plate actuator system, we have studied its equilibrium status in Chapter 3 by torque analysis and its transient response in Chapter 4 by using Newton's law and circuit analogues. In essence, these treatments can be discussed via control theory by using state equations. Using state variable theory, we will further our discussion of the previous two chapters by considering more complex system configurations. One of the configurations is that the voltage source driving the actuator is not an ideal voltage source. It has an output resistance R_s or internal conductance g_s. The other configuration is that the damping coefficient is no longer to be considered constant. Due to the gap distance change during dynamic motion of the top plate, the variation of the damping coefficient is included in the state equations.

Control theory not only provides another view of the system behavior, but, more importantly, it also provides a theoretical methodology to improve the system behavior. In this chapter we provide the theoretical background of our control methodologies for MEMS mirror in a large channel count optical switch.

A popular control schema for a MEMS mirror actuator in the industry is shown in Figure 1-7 [41]. It is based on light-power detection of the beam to be switched, with limitation of a threshed to detect the position of the outgoing light beam. In this chapter, we introduce a sensor capacitor located on the mirror plate. The capacitance of this sensor capacitor can determine the position of the mirror. A sensing bridge detects this capacitance change when the mirror tilts.

Based on this, two optimal control methodologies are presented, including bang-bang control and Kalman closed loop feedback control. With these methodologies, the mirror can switch fast and can be as stable as desired. Additionally, using this capacitor sensor to detect the mirror position makes it possible to design future systems on a chip.

Another two control implementation topics are also discussed in this chapter; these also improve the possibilities to design a system on a chip. One topic is a featured high voltage driving circuit to reduce the complexity of the driving circuit. The other one is a modular structure for the embedded system.

5.2 System description in state variable forms

5.2.1 System description

In this section, we will study the behavior of this optimal plate actuator system by using state equations in control theory. In this way, we will study the stability of the top movable plate, reviewing the pull-in phenomena and transient responses. Further, and most importantly, we will show the ways to improve the system response by using feedback control theory.

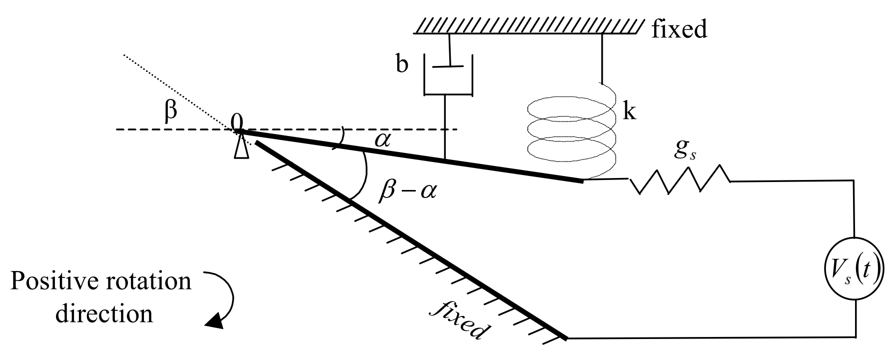

Figure 5-1 A plate actuator system with the optimal plate structure

Same as what did in Chapter 3 and Chapter 4, for simplification, we only consider half of the mirror actuator structure here due to the symmetry in the system. Figure 5-1 represents the same optimal plate actuator as discussed in Chapter 3, which is developed from Figure 3-7. The top plate is the movable mirror plate. Its one end is fixed at point 0 with a fixed rotation axis. A torsion spring is attached to this end. The other end of the top plate can freely rotate.

The position of the torsion spring is at the fixed end of the top plate, it is drawn at the free end for simplification. The bottom plate is fixed with an angle of β to the horizontal line. The difference between Figure 3-7 and Figure 5-1 is the inclusion of the damping effects shown as the dashpot, and the appearance of internal conductance g_s of the voltage source.

Originally, the top plate is in the horizontal position when the applied voltage is zero. Thus the two conducting plates have an angular gap of β initially. We denote β as α_0 in this chapter. The width of the two plates is both W. The length of both plates is L. There is a gap distance of δ between the origin point 0 and the end of the bottom plate, which keeps the two plates electrically isolated from each other.

When the voltage source $V_s(t)$ is applied across the two plates, there is electrostatic torque on the top plate. Because of this electrostatic torque, the top plate rotates toward the bottom plate, making an angle of α to the original horizontal line. This results in an angle of $\beta-\alpha$ or $\alpha_0-\alpha$ between the two plates. The torsion spring attached to the end of the top plate applies an elastically spring torque on the top plate, if the top plate rotates.

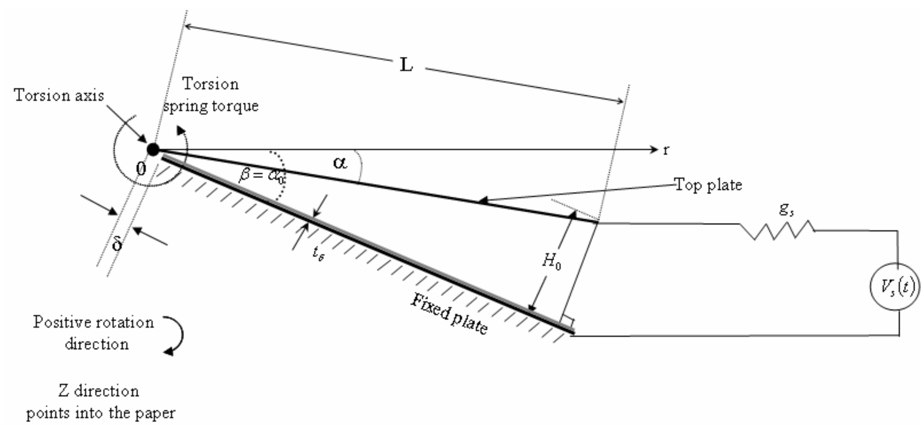

Figure 5-2 The schematic of the optimal plate actuator in cylindrical coordinates

The system is re-plotted in Figure 5-2 to show in cylindrical coordinates. The positive rotation direction is in the clockwise direction. The positive Z direction points into the paper. Additionally, the tip at the end of the top plate has a distance of H_0 referenced to the fixed bottom plate. To keep the top plate electrically isolated from the bottom plate in case it touches the bottom plate, a thin isolation coating of thickness t_δ is covered on the top of the bottom plate. This is the shadowed thin layer shown in Figure 5-2. t_δ is such a small value that it will be ignored in our later discussion for simplification. When $V_s(t)$ is a constant DC value, we denote the final equilibrium angular position of the top plate as $\overline{\alpha}$. Having finished the system definition, we will work on the torque elements involved in the state equations before we introduce these equations.

5.2.2 The electrostatic torque on the top plate in cylindrical coordinates

In Section 3.3, we have derived the torque applied on the top plate by the electrostatic force using Cartesian coordinates. Here to simply the later format of state equations, we derive the same torque using cylindrical coordinates. In essence, they are the same.

If we make an assumption that both of the two plates are semi-infinitely long in our discussion, we can ignore the fringe effects in our analysis. In the case when the size of the plates is much larger than the separated angular gap between them, the assumption is valid. When the size of the plates is comparable with the angular gap, fringe effects have to be considered. According to Nishiyama [67], Nemirovosky [68], there will be an error about 10% if the size of the plate is comparable to the gap.

We denote $\vec{E}$ as the electrical field intensity between the two plates; Q as the charge on either plate. Based on Laplace's equation, according to Shen [48], we have the following:

$$\vec{E} = -\frac{1}{r}\frac{V_s}{\alpha_0 - \alpha(t)}\hat{\phi} \tag{5-1}$$

where $\hat{\phi}$ is the unit vector in cylindrical coordinates.

Because the left side of Gauss's law is

$$\oint_S \vec{E} \bullet d\vec{s} = \iint_S \frac{V_s}{r(\alpha_0 - \alpha(t))}\hat{\phi} \bullet \hat{\phi} drdz = \int_{r=\delta}^{L}\int_{z=0}^{W} \frac{V_s}{r(\alpha_0 - \alpha(t))} drdz$$

$$= \frac{V_s \cdot W}{(\alpha_0 - \alpha(t))}\ln\frac{L}{\delta} \tag{5-2}$$

Using Gauss's Law $\oint \vec{E} \bullet d\vec{s} = \frac{Q}{\varepsilon}$, we have

$$\frac{V_C(t) \cdot W}{(\alpha_0 - \alpha(t))}\ln\frac{L}{\delta} = \frac{Q(t)}{\varepsilon} \tag{5-3-a}$$

Or

$$\frac{Q(t)}{V_C(t)} = \frac{\varepsilon \cdot W}{(\alpha_0 - \alpha(t))}\ln\frac{L}{\delta} \tag{5-3-b}$$

Then the total charge $Q(t)$ on either of the plates is

$$Q(t) = \frac{\varepsilon \cdot W \cdot V_C(t)}{\alpha_0 - \alpha(t)}\ln\frac{L}{\delta} \tag{5-4}$$

As the definition of capacitance C is $C = \frac{Q}{V_C}$, thus we have the capacitance between the two plates as

$$C(t) = \frac{\varepsilon \cdot W}{(\alpha_0 - \alpha(t))}\ln\frac{L}{\delta} \tag{5-5}$$

To simplify, we can denote

$$A = W \cdot L \text{ and } \overline{L} = \frac{L}{\ln \frac{L}{\delta}} \tag{5-6}$$

Then
$$C(t) = \frac{\varepsilon \cdot A}{\overline{L}(\alpha_0 - \alpha(t))} \tag{5-7}$$

The electrostatic energy stored between the two plates is, by Ida [44, page 248]

$$U_e(t) = \frac{1}{2}\frac{Q(t)^2}{C(t)} = \frac{1}{2}\frac{(\alpha_0 - \alpha(t)) \cdot Q(t)^2}{\frac{\varepsilon A}{\overline{L}}} \tag{5-8}$$

The torque $\vec{T}_e$ on the top plate due to the electrostatic force is, by Ida [44, page 254]

$$\vec{T}_e(t) = -\frac{\partial U_e}{\partial \alpha(t)} = \frac{1}{2}\frac{\cdot Q(t)^2}{\frac{\varepsilon A}{\overline{L}}}\hat{\phi} \tag{5-9}$$

So far, we have finished the calculation of the electrostatic torque. Next, we will work on the damping torque.

5.2.3 The damping coefficient–a variable of time

In Chapter 4, according to Chang [47], we have written Equation (4-9) to evaluate the damping coefficient. Squeeze film damping is considered to be dominant. In (4-9) h_0 is the average distance between the two plates. It is calculated as $h_0 = \frac{H_0}{2}$ where H_0 is the distance from the tip point of the top plate to the fixed bottom plate as shown in Figure 5-2. In Chapter 4, to simplify the discussion, the damping coefficient is treated as a constant during the entire transient response because of the usage of a constant h_0. However, in reality, when the top plate is moving toward the bottom plate, H_0 changes, resulting in h_0 decreasing. Thus a time constant damping coefficient seems not enough. With state equations, we consider that h_0 in Equation (4-9) is a variable of time t in this chapter. That is $h_0 = h_0(t)$. Recall the definition of η as $\eta = \frac{2 \cdot L}{W}$. We can rewrite the damping coefficient of Equation (4-9) as

$$
\begin{aligned}
B &= \frac{48}{\pi^6(\eta^2+4)} \frac{\mu_{air} W (2 \cdot L)^5}{h_0(t)^3} \\
&= \frac{48}{\pi^6(\eta^2+4)} \frac{\mu_{air} W (2 \cdot L)^5}{\left(\frac{H_0(t)}{2}\right)^3} \\
&= \frac{\rho_B}{H_0(t)^3}
\end{aligned}
\tag{5-10}
$$

where
$$\rho_B = \mu_{air} W (2 \cdot L)^5 \cdot 2^3 \cdot \frac{48}{\pi^6(\eta^2+4)} \tag{5-11}$$

Thus the damping coefficient B is a variable of the position of the top plate. When the position of the top plate changes with time, it becomes a variable of time. If we denote H_{01} as to the distance between the tip of the top plate and the bottom plate when the top plate is at its original horizontal position with $\alpha(0) = 0$, then

$$H_{01} = L \cos \beta \tag{5-12}$$

When the top plate moves to a position at $\alpha(t)$, $H_0(t) = L \cdot \cos(\beta - \alpha(t))$. Practically in our application, the tilt angle $\alpha(t)$ of the top mirror plate is around 8 degrees, which is about 0.1517 radians. As what has been done in Chapter 4, this means that α is a quite small number, so we can write the first degree approximation as

$$H_0(t) \approx H_{01} - L \cdot \alpha(t) \tag{5-13}$$

Thus the damping coefficient (5-10) becomes

$$B(t) = \frac{\rho_B}{(H_{01} - L\alpha(t))^3} \tag{5-14}$$

Equation (5-14) is a nonlinear damping coefficient which varies with the tilt angle $\alpha(t)$. We then can write the damping torque as

$$\vec{T}_{damp}(t) = -B(t)\dot{\alpha}\hat{\phi} = -\frac{\rho_B}{(H_{01} - L\alpha(t))^3}\dot{\alpha}\hat{\phi} \tag{5-15}$$

Where $\dot{\alpha}(t) = \frac{d\alpha}{dt}$.

5.2.4 State equations for the optimal plate actuator system

Notice that there is a stopper to the position of the top plate, that is $0 \le \alpha(t) \le \beta$. This means that the top mirror cannot move beyond the boundary set by β. Keeping this in mind, with the damping torque and the electrostatic torque developed in the previous sections, we can write the equations to describe the motion of the system as

$$J\ddot{\alpha}(t) = -\frac{\rho_B}{(H_{01} - L\alpha(t))^3}\dot{\alpha}(t) - k\alpha(t) + \frac{Q^2(t)}{2\varepsilon\frac{A}{L}} \tag{5-16}$$

$$\dot{Q}(t) = g_s \cdot \left(V_s(t) - \frac{Q(t)(\beta - \alpha(t))}{\varepsilon \frac{A}{L}} \right) \tag{5-17}$$

Equation (5-16) is the rewritten of Newton's law. On the right side of (5-16), the first term corresponds to the damping torque; the second term corresponds to the spring torsion torque; and the third term corresponds to the electrostatic torque. Basically (5-17) is the Kirchhoff's current law. Its last term in the right side is the applied voltage over the two plates. Based on (5-16) and (5-17), we will construct the state equations in terms of state variables Q, α and $\dot{\alpha}$. To simply the later discussion, we will use $Q(t)$ as Q, $\alpha(t)$ as α and $\dot{\alpha}(t)$ as $\dot{\alpha}$.

In order to obtain a better-behaved matrix later, we will do normalization here. We define constants κ, γ and new variables q, φ to normalize Q and α before the introduction of the state equations,

$$Q = \kappa q \qquad \alpha = \gamma\varphi \qquad \beta = \gamma\varphi_b \tag{5-18}$$

The value of κ and γ will be shown after we have finished this normalization.

Then Equation (5-17) becomes

$$\kappa\dot{q} = g_s V_s(t) - g_s \frac{\kappa\gamma q \varphi}{\varepsilon \frac{A}{L}} \tag{5-19}$$

Or

$$\dot{q} = \frac{g_s}{\kappa} V_s(t) - g_s \frac{\gamma q(\varphi_b - \varphi)}{\varepsilon \frac{A}{L}} \tag{5-20}$$

Again using a constant υ to normalize $V_s(t)$ then

$$\upsilon = \frac{g_s}{\kappa} V_s(t) \tag{5-21}$$

and define

$$\gamma = \frac{\varepsilon \frac{A}{L}}{g_s} \tag{5-22}$$

so that (5-20) becomes

$$\dot{q} = \upsilon - q(\varphi_b - \varphi) \tag{5-23}$$

Put (5-18) (5-22) into (5-16)

$$\ddot{\varphi} = -\frac{\rho_B}{J H_{01}{}^3 \left(1 - \frac{L\gamma}{H_{01}} \varphi(t)\right)^3} \dot{\varphi} - \frac{k}{J} \varphi + \frac{\kappa^2 q^2}{2J\gamma\varepsilon \frac{A}{L}} \tag{5-24}$$

If we set

$$\kappa = \sqrt{\varepsilon \frac{A}{L} J\gamma}\,,\ \frac{k}{J} = \omega_J^2,\ \tau = \frac{\rho_B}{2 H_{01}{}^3 k} \omega_J \tag{5-25}$$

using (5-12), (5-24) becomes our normalized equation of motion

$$\ddot{\varphi} = -\frac{2\tau\omega_J}{\left(1 - \frac{\gamma}{\cos\beta} \varphi(t)\right)^3} \dot{\varphi} - \omega_J^2 \varphi + \frac{q^2}{2} \tag{5-26}$$

So far, we have had system equations as (5-23) and (5-26). In order to analyze the stability of the system, we need to take care of the behavior of the system at $\varphi_b = \varphi_0 = \frac{\beta}{\gamma} = \frac{\alpha_0}{\gamma}$, where the bottom plate located. Referenced to Maithripala [46] and Senturia [40], the system behavior at this boundary can be defined in the following:

1) When the electrostatic torque is higher than the mechanical spring torque, the top plate stays at $\varphi_b = \frac{\alpha_0}{\gamma}$, with zero velocity. It has lost all of its kinetic energy. In this case only Equation (5-17) holds and Equation (5-16) does not hold any more. That is

$$\dot{\varphi}_b = 0 \qquad \text{and } \dot{q} = -q(\varphi_b - \varphi) + \upsilon \tag{5-27}$$

2) When the electrostatic torque is less than the mechanical spring torque, the top plate moves up toward its original position at $\varphi = 0$, and the top plate has zero velocity.

Now we can begin to construct the state equations. From the previous illustration, the state variables are $x_1 = q$, $x_2 = \varphi$, $x_3 = \dot{\varphi}$, with the state space of the system as

$$X = [x_1, x_2, x_3]^T \in R^3, \quad 0 \le x_2 \le \varphi_b \tag{5-29}$$

The output vector is $y = [y_1, y_2]^T$, where y_1 is the normalized voltage across the two plates. y_2 is the normalized angular position of the top movable plate. Then we obtain the state equations of the system are

$$\begin{bmatrix}\dot{x}_1\\ \dot{x}_2\\ \dot{x}_3\end{bmatrix}=\begin{bmatrix}-x_1\left(\varphi_b-x_2\right)\\ x_3\\ \dfrac{-2\tau\omega_J}{\left(1-\dfrac{\gamma}{\cos\beta}x_2\right)^3}x_3-\omega_J^2x_2+\dfrac{x_1^2}{2}\end{bmatrix}+\begin{bmatrix}1\\0\\0\end{bmatrix}\upsilon \tag{5-30}$$

$$y=\begin{bmatrix}y_1\\ y_2\end{bmatrix}=\begin{bmatrix}x_1\left(\varphi_b-x_2\right)\\ x_2\end{bmatrix} \tag{5-31}$$

with (5-27) at $\varphi=\varphi_b$ and $x_1=q$, $x_2=\varphi$ and $x_3=\dot{\varphi}$. We have two output variables. One is y_1, which is the voltage across the two plates. The other is y_2, which is the angular position of the top plate. It is interesting to notice that all the three state variables x_1, x_2, and x_3 are detectable.

5.3 Stability analysis

5.3.1 An equilibrium point solved from state equations

When the system is in an equilibrium state at some given input $V_s(t)$, corresponding to the normalized $\overline{\upsilon}$, we can obtain the corresponding equilibrium state vector, with

$$\overline{x}_3=0 \quad \overline{x}=[\overline{x}_1,\overline{x}_2,0]^T \tag{5-33}$$

From (5-30) or (5-26)

$$\overline{x}_1^{\,2}=2\omega_J^{\,2}\overline{x}_2 \tag{5-34}$$

From (5-30) or (5-23), we have

$$\overline{\upsilon}=\overline{x}_1\left(\varphi_b-\overline{x}_2\right) \tag{5-35}$$

Combining (5-34) and (5-35), we have a cubic order equation related to $\bar{x}_1$ or $\bar{x}_2$.

That is

$$\bar{\upsilon} = \bar{x}_1\left(\varphi_b - \frac{\bar{x}_1^{\,2}}{2\omega_J}\right) \tag{5-36-a}$$

Or

$$\frac{\bar{x}_1^{\,3}}{2\omega_J} - \bar{x}_1\varphi_b + \bar{\upsilon} = 0 \tag{5-36-b}$$

Equation (5-36) has three solutions. From the mathematical handbook by Gui [49], of these three solutions, two of them are complex numbers, only one is a real solution. Because $\bar{x}_1$ is a state variable with real physical meaning; only the real number solution is kept. The other complex-number solutions are discarded. Equation (5-36) is quite similar to what we have in Equation (3-5), which has three equilibria, with only one being a stable state as shown in Figure 3-2.

5.3.2 Linearization around an equilibrium point

Since Equation (5-30) is a nonlinear equation, in order to perform stability analysis, we want to analyze the system around some equilibrium point $\bar{x}$. To do that, we define new variables as $\xi = x - \bar{x}$, that is

$$\begin{bmatrix} \xi_1 \\ \xi_2 \\ \xi_3 \end{bmatrix} = \begin{bmatrix} x_1 - \bar{x}_1 \\ x_2 - \bar{x}_2 \\ x_3 - \bar{x}_3 \end{bmatrix} \tag{5-37}$$

As $\bar{x}_3 = 0$ at equilibrium, (5-37) becomes

$$\begin{bmatrix} \xi_1 \\ \xi_2 \\ \xi_3 \end{bmatrix} = \begin{bmatrix} x_1 - \bar{x}_1 \\ x_2 - \bar{x}_2 \\ x_3 \end{bmatrix} \tag{5-38}$$

Where the new state space is $\Omega = \left\{ [\xi_1, \xi_2, \xi_3]^T \in R^3 \middle| -\bar{x}_2 \le \xi_2 \le -\bar{x}_2 + \varphi_b \right\}$, ($\varphi_b = \dfrac{\beta}{\gamma}$).

Accordingly, the output variable y becomes η, which is $\begin{bmatrix} \eta_1 \\ \eta_2 \end{bmatrix} = \begin{bmatrix} y_1 - \bar{y}_1 \\ y_2 - \bar{y}_2 \end{bmatrix}$; and the

input variable υ becomes μ, which is $\mu = \upsilon - \bar{\upsilon}$. From (5-31)

$$\begin{bmatrix} \bar{y}_1 \\ \bar{y}_2 \end{bmatrix} = \begin{bmatrix} \bar{x}_1 (\varphi_b - \bar{x}_2) \\ \bar{x}_1 \end{bmatrix} \tag{5-39}$$

Using these new definitions and (5-35), Equation (5-30) becomes

$$\dot{\xi}_1 = \xi_1 (\bar{x}_2 - \varphi_b) + \xi_2 \bar{x}_1 + \xi_1 \xi_2 + \mu \tag{5-40}$$

$$\dot{\xi}_2 = \xi_3 \tag{5-41}$$

$$\dot{\xi}_3 = -\xi_3 \frac{2\tau\omega_J}{\left[1 - \dfrac{\gamma}{\cos\beta} (\bar{x}_2 + \xi_2) \right]^3} - \xi_2 \omega_J^2 + \xi_1 \bar{x}_1 + \frac{\xi_1^2}{2} \tag{5-42}$$

And Equation (5-31) and (5-32) becomes

$$\eta_1 = -\xi_1 \xi_2 + \xi_1 (\varphi_b - \bar{x}_2) - \xi_2 \bar{x}_1 \tag{5-43}$$

$$\eta_2 = \xi_2 \tag{5-44}$$

Thus by using these new variables, the state equations (5-30) becomes

$$\dot{\xi} = f(\xi) + gu \qquad \eta = h(\xi) \tag{5-45}$$

where $$f(\xi)=\begin{bmatrix} \xi_1(\bar{x}_2-\varphi_b)+\xi_2\bar{x}_1+\xi_1\xi_2 \\ \xi_3 \\ -\xi_3\dfrac{2\tau\omega_J}{\left[1-\dfrac{\gamma}{\cos\beta}(\bar{x}_2-\xi_2)\right]^3}-\xi_2\omega_J^2+\xi_1\bar{x}_1+\dfrac{\xi_1^2}{2} \end{bmatrix} \quad \text{if } \xi\notin\partial\Omega \qquad (5\text{-}46)$$

and $$f(\xi)=\begin{bmatrix} \xi_1(\bar{x}_2-\varphi_b)+\xi_2\bar{x}_1+\xi_1\xi_2 \\ 0 \\ 0 \end{bmatrix} \qquad \text{if } \xi\in\partial\Omega$$

(5-47)

$$g=\begin{bmatrix} 1 \\ 0 \\ 0 \end{bmatrix} \qquad (5\text{-}48)$$

$$h(\xi)=\begin{bmatrix} -\xi_1\xi_2+\xi_1(\varphi_b-\bar{x}_2)-\xi_2\bar{x}_1 \\ \xi_2 \end{bmatrix} \qquad (5\text{-}49)$$

Using (5-45), we can write the linear approximation of (5-30) around the equilibrium point $\bar{x}$ with a small variation. By the definition of the new variable in (5-38), $\bar{x}$ is the original point in the new variable system, then

$$\delta\dot{\xi}=\frac{\partial f}{\partial\xi}\delta\xi+g\delta\mu \qquad (5\text{-}50)$$

$$\left.\frac{\partial f}{\partial\xi}\right|_{\xi=0}=\left.\begin{bmatrix} \dfrac{\partial f_1}{\partial\xi_1} & \dfrac{\partial f_1}{\partial\xi_2} & \dfrac{\partial f_1}{\partial\xi_3} \\ \dfrac{\partial f_2}{\partial\xi_1} & \dfrac{\partial f_2}{\partial\xi_2} & \dfrac{\partial f_2}{\partial\xi_3} \\ \dfrac{\partial f_3}{\partial\xi_1} & \dfrac{\partial f_3}{\partial\xi_2} & \dfrac{\partial f_3}{\partial\xi_3} \end{bmatrix}\right|_{\xi=0}$$

$$=\begin{bmatrix} (\bar{x}_2-\varphi_b)+\xi_2 & \bar{x}_1+\xi_1 & 0 \\ 0 & 0 & 1 \\ \bar{x}_1+\xi_1 & -\omega_J^2+\xi_3(-2\tau\omega_J)\left(3\frac{\gamma}{\cos\beta}\right)\left[1-\frac{\gamma}{\cos\beta}(\xi_2+\bar{x}_2)\right]^{-4} & \dfrac{-2\tau\omega_J}{\left[1-\frac{\gamma}{\cos\beta}(\xi_2+\bar{x}_2)\right]^3} \end{bmatrix}_{\xi=0}$$

$$=\begin{bmatrix} (\bar{x}_2-\varphi_b) & \bar{x}_1 & 0 \\ 0 & 0 & 1 \\ \bar{x}_1 & -\omega_J^2 & \dfrac{-2\tau\omega_J}{\left(1-\frac{\gamma}{\cos\beta}\bar{x}_2\right)^3} \end{bmatrix} \tag{5-51}$$

where $$\bar{\tau}=\frac{\tau}{\left(1-\frac{\gamma}{\cos\beta}\bar{x}_2\right)^3} \tag{5-52}$$

$$A=\begin{bmatrix} \bar{x}_2-\varphi_b & \bar{x}_1 & 0 \\ 0 & 0 & 1 \\ \bar{x}_1 & -\omega_J^2 & -2\bar{\tau}\omega_J \end{bmatrix} \qquad B=\begin{bmatrix} 1 \\ 0 \\ 0 \end{bmatrix} \tag{5-53}$$

5.3.3 Routh-Hurwitz test

For the linearized equation $\delta\dot{\xi}=A\delta\xi+B\delta\mu$, we can perform the Routh-Hurwitz test to check the stability of the system. In order to make the system to be stable at the original equilibrium point, it should satisfy the following criteria:

All the system's eigenvalues should be in the left half plane. That is all the roots of

$\det(sI_3 - A) = 0$ must be in the left half plane, where $I_3 = \begin{bmatrix} 1 & 0 & 0 \\ 0 & 1 & 0 \\ 0 & 0 & 1 \end{bmatrix}$, s is the

Laplace transform complex.

$$\det(sI_3 - A) = \begin{vmatrix} s-(\bar{x}_2-\varphi_b) & -\bar{x}_1 & 0 \\ 0 & s & -1 \\ -\bar{x}_1 & \omega_J^2 & s+2\bar{\tau}\omega_J \end{vmatrix}$$

$$= s[s-(\bar{x}_2-\varphi_b)](s+2\bar{\tau}\omega_J) - \bar{x}_1^2 + \omega_J^2[s-(\bar{x}_2-\varphi_b)]$$

$$= s^3 + s^2[2\bar{\tau}\omega_J - (\bar{x}_2-\varphi_b)] + s[\omega_J^2 - 2\bar{\tau}\omega_J(\bar{x}_2-\varphi_b)] - \bar{x}_1^2 - \omega_J^2(\bar{x}_2-\varphi_b) \quad \text{(5-54)}$$

For (5-54), the coefficients of this polynomial are listed in Table 5-1.

a_3	a_2	a_1	a_0
1	$2\bar{\tau}\omega_J - (\bar{x}_2-\varphi_b)$	${\omega_J}^2 - 2\bar{\tau}\omega_J(\bar{x}_2-\varphi_b)$	$-\bar{x}_1^2 - {\omega_J}^2(\bar{x}_2-\varphi_b)$

Table 5-1 The coefficients of $\det(sI_3 - A) = 0$

As the coefficient a_3 is 1, which is greater than 0, in order to make the roots of $\det(sI_3 - A) = 0$ lying in the left half plane, all the other coefficients must be greater than 0. To avoid solving (5-55) directly for its roots, we use the Routh-Hurwitz test.

According to the Routh-Hurwitz test, a_i comes from the coefficients of the original polynomial; b_i and c_i have a pattern defined as following:

s^n		a_n	a_{n-2}	a_{n-3}	$\cdots$
s^{n-1}		a_{n-1}	a_{n-3}	a_{n-5}	$\cdots$
s^{n-2}		b_{n-1}	b_{n-3}	b_{n-5}	$\cdots$
s^{n-3}		c_{n-1}	c_{n-3}	c_{n-5}	$\cdots$
$\cdots$		$\cdots$	$\cdots$	$\cdots$	$\cdots$
s^0					

Table 5-2 The Routh Array to determine the stability of the system

$$b_{n-1} = \frac{-1}{a_{n-1}}\begin{vmatrix} a_n & a_{n-2} \\ a_{n-1} & a_{n-3} \end{vmatrix} \tag{5-55-a}$$

$$b_{n-3} = \frac{-1}{a_{n-1}}\begin{vmatrix} a_n & a_{n-4} \\ a_{n-1} & a_{n-5} \end{vmatrix} \tag{5-55-b}$$

$$c_{n-1} = \frac{-1}{b_{n-1}}\begin{vmatrix} a_{n-1} & a_{n-3} \\ b_{n-1} & b_{n-3} \end{vmatrix} \tag{5-55-c}$$

This test confirms the stability of the system if there is no sign change for all the entries of the first column in the Routh Array (blanks or ends of rows are treated as zero values to calculate), as shown in Table 5-2. Using the Routh-Hurwitz test to our case here, we have the Routh Array table as shown in Table 5-3. And we have

$$b_2 = \frac{-1}{a_2}\begin{vmatrix} a_3 & a_1 \\ a_2 & a_0 \end{vmatrix} = \frac{-1}{a_2}\left(a_3 a_0 - a_2 a_1\right) \tag{5-56-a}$$

$$b_0 = 0 \tag{5-56-b}$$

$$c_2 = \frac{-1}{b_2}\begin{vmatrix} a_2 & a_0 \\ b_2 & b_0 \end{vmatrix} = \frac{-1}{b_2}\left(a_2 b_0 - b_2 a_0\right) = a_0 \tag{5-56-c}$$

		First coefficient column

s^3		$a_3 = 1$
s^2		$a_2 = 2\bar{\tau}\omega_J - (\bar{x}_2 - \varphi_b)$
s^1		$b_2 = \dfrac{-1}{a_2}(a_3 a_0 - a_2 a_1)$
s^0		$c_2 = a_0$

Table 5-3 The Routh-Hurwitz test used for the plate actuator system

There are four coefficients in the first coefficient column of the Routh-Array. There are a_3, b_2 and c_2. Because $a_3 = 1 > 0$, in order to keep no sign change in this column, it is required that $a_2 > 0$, $b_2 > 0$ and $c_2 > 0$ in Table 5-3.

Since $a_2 = 2\bar{\tau}\omega_J - (\bar{x}_2 - \varphi) = 2\bar{\tau}\omega_J + (\varphi_b - \bar{x}_2)$, as $\bar{x}_2 < \varphi_b$, $\bar{\tau}$ and ω_J are greater than 0, so $a_2 > 0$ automatically holds.

In order to make $c_2 > 0$, from (5-56-c), we have $a_0 > 0$, that is

$$a_0 = -(\bar{x}_2 - \varphi_b)\omega_J{}^2 - \bar{x}_1{}^2 > 0 \tag{5-57-a}$$

using (5-34) $\bar{x}_1{}^2 = 2\omega_J{}^2\bar{x}_2$, (5-58-a) becomes

$$\bar{x}_2 < \frac{\varphi_b}{3} \tag{5-57-b}$$

Since $\bar{x}_2$ is the normalized angular position of the top plate and it has to be no less than zero to keep its physical meaning, we can write

$$0 \le \bar{x}_2 < \frac{\varphi_b}{3} \tag{5-58}$$

In order to make $b_2 > 0$, that is $b_2 = \frac{-1}{a_2}\left(a_3 a_0 - a_2 a_1\right) > 0$. Because $a_2 > 0$, then it requires that

$$\left(a_3 a_0 - a_2 a_1\right) < 0 \qquad \text{(5-59).}$$

It can be proved that (5-59) does holds for our system. For details, please refer to Appendix 1.

Till this point, we have proved that there is no sign change for all the four coefficients inside the first coefficient column of the Routh Array in Table 5-3 under the constraints of (5-58). Thus we have shown that the system is stable under the condition of (5-58), which is $0 \le \bar{x}_2 < \frac{\varphi_b}{3}$. When $\bar{x}_2 > \frac{\varphi_b}{3}$, at least the last coefficient a_0 is in the Routh-Array is less than 0, the Routh-Hurwitz test fails, so the system is unstable. In reality, when $\bar{x}_2 > \frac{\varphi_b}{3}$, the top plate can no longer hold an equilibrium position on top of the bottom plate. It instantly draws to the bottom plate by the electrostatic torque and then drops onto the bottom plate. If we remember that the derivation so far is based on the assumption of semi-infinite long plates, which is a good approximation when $\bar{x}_2$ is a very small number, then the result that the system is stable under the condition $0 \le \bar{x}_2 < \frac{\varphi_b}{3}$ agrees with the result in Section 3.3 quite well.

5.3.4 Lyapunov function

According to control theory, if we want to check the stability of a system $\dot{x} = f(x(t),t)$, there should exist a scalar function $V(x(t),t)$, which satisfies the following criteria, then the system is asymptotically stable at x_0 ([50, pages 101-102], [70]):

1) The partial derivatives of $\frac{\partial V}{\partial x}$ and $\frac{\partial V}{\partial t}$ are continuous functions

2) $V(x(t),t) \geq 0$ or bounded below

3) $\frac{dV}{dt} < 0$ for all x in the neighborhood of x_0 and $\left.\frac{dV}{dt}\right|_{x=x_0} = 0$

Then $V(x(t),t)$ is the Lyapunov function of the system. Next we will show the existence of a Lyapunov function of our system. In this way we prove the stability of our system.

Using the new vector variable ξ defined by (5-38), we choose the following scalar function:

$$H(\xi) = \frac{1}{2}\xi_3{}^2 + \frac{1}{2}\omega_J^2\xi_2^2 + \frac{1}{2}\xi_1^2(\varphi_b - \bar{x}_2 - \xi_2) - \bar{x}_1\xi_1\xi_2 \tag{5-62}$$

In the following, we want to prove that $H(\xi)$ in (5-62) is a local Lyapunov function under the condition in (5-58), namely $\bar{x}_2 < \frac{\varphi_b}{3}$, when ξ is a very small number,

$-\bar{x}_2 \le \xi_2 \le -\bar{x}_2 + \varphi_b$, ($\varphi_b = \dfrac{\beta}{\gamma}$). If this is confirmed, then the system is locally asymptotically stable around this original equilibrium point.

Apparently, $H(\xi)=0$ ($\xi = 0$).

$H(\xi)>0$ ($\xi \ne 0$) is approved in this way. Because the first two terms in (5-62) are definite greater than zero, $\frac{1}{2}\xi_3{}^2 > 0$, $\frac{1}{2}\omega_J^2\xi_2^2 > 0$, then the 3rd term under the condition of $\bar{x}_2 < \dfrac{\varphi_b}{3}$, will be

$$\frac{1}{2}\xi_1^2(\varphi_b - \bar{x}_2 - \xi_2) - \bar{x}_1\xi_1\xi_2 > \frac{1}{3}\xi_1^2\left(\varphi_b - \frac{\varphi_b}{3} - \xi_2\right) - \bar{x}_1\xi_1\xi_2$$

$$= \frac{1}{3}\xi_1^2\left(\frac{2\varphi_b}{3} - \xi_2\right) - \bar{x}_1\xi_1\xi_2 \qquad \text{(5-63-a)}$$

Notice that from (5-58) $-\bar{x}_2 \le \xi_2 \le -\bar{x}_2 + \varphi_b$

$$\left.\begin{array}{c} -\bar{x}_2 \le \xi_2 \le -\bar{x}_2 + \varphi_b \\ \bar{x}_2 < \dfrac{\varphi_b}{3} \end{array}\right\} \Rightarrow \left(\frac{2\varphi_b}{3} - \xi_2\right) > -\frac{2\varphi_b}{3} \qquad \text{(5-63-b)}$$

Thus both $\left(\dfrac{2\varphi_b}{3} - \xi_2\right)$ and ξ_2 are bounded, there must exit a $\varepsilon_r > 0$, and $|\xi_1| < \varepsilon_r$, such that $\frac{1}{2}\xi_3{}^2 + \frac{1}{2}\omega_J^2\xi_2^2 + \frac{1}{3}\xi_1^2\left(\dfrac{2\varphi_b}{3} - \xi_2\right) - \bar{x}_1\xi_1\xi_2 > 0$. Thus we have the conclusion that $H(\xi)>0$ ($\xi \ne 0$).

Second we want to show that $H(\xi)$'s time derivative is smaller than 0.

$$\frac{dH(\xi)}{dt} = \xi_3 \cdot \dot{\xi}_3 + \omega_J{}^2 \xi_2 \cdot \dot{\xi}_2 + (\varphi_b - \bar{x}_2 - \xi_2)(\xi_1 \dot{\xi}_1) + \left(\frac{1}{2}\xi_1^2\right)(-\dot{\xi}_2) - \xi_1 \dot{\xi}_2 \bar{x}_1 - \bar{x}_1 \xi_2 \dot{\xi}_1$$

$$= \xi_3 \cdot \dot{\xi}_3 + \left(\omega_J{}^2 \xi_2 - \bar{x}_1 \xi_1 - \frac{1}{2}\xi_1^2 - \xi_1 \bar{x}_1\right) \cdot \dot{\xi}_2 + [(\varphi_b - \bar{x}_2 - \xi_2)\xi_1 - \xi_2 \bar{x}_1]\dot{\xi}_1 \qquad (5\text{-}64)$$

To proceed (5-64) further, put (5-40), (5-41) and (5-42). Then (5-64) becomes

$$\frac{dH(\xi)}{dt} = \xi_3 \cdot \left(-\xi_3 2\bar{\tau}\omega_J - \xi_2 \omega_J^2 + \xi_1 \bar{x}_1 + \frac{\xi_1^2}{2}\right) + \left(\omega_J{}^2 \xi_2 - \bar{x}_1 \xi_1 - \frac{1}{2}\xi_1^2\right)\xi_3 +$$
$$[(\varphi_b - \bar{x}_2 - \xi_2)\xi_1 - \xi_2 \bar{x}_1](-[(\varphi_b - \bar{x}_2 - \xi_2)\xi_1 - \xi_2 \bar{x}_1] + \mu)$$

$$\frac{dH(\xi)}{dt} = -\xi_3{}^2 \cdot 2\bar{\tau}\omega_J - [(\varphi_b - \bar{x}_2 - \xi_2)\xi_1 - \xi_2 \bar{x}_1]^2 + \mu[(\varphi_b - \bar{x}_2 - \xi_2)\xi_1 - \xi_2 \bar{x}_1] \qquad (5\text{-}65)$$

For (5-65), if the input μ is zero, then it is apparently that $\frac{dH(\xi)}{dt} < 0$ if $\xi \neq 0$,

$\xi \in \Omega$, ; and $\frac{dH(\xi)}{dt} = 0$ if $\xi = 0$.

If μ is not zero, because the first two terms in $\frac{dH(\xi)}{dt}$ is less than zero, and because

$\frac{dH(\xi)}{dt}$ is a continuous function, so that should exist some ε_u, such that $\mu \in \varepsilon_u$,

satisfies $\frac{dH(\xi)}{dt} < 0$.

So far, we have proved that $H(\xi)$ is the local Lyapunov function of the system. Thus the system is locally asymptotically stable around this original equilibrium point, if $0 \le \bar{x}_2 < \frac{\varphi_b}{3}$.

5.4 Control algorithms

Now that we have introduced the state equations of the optimal plate actuator system, we will work on the control laws to improve the system behavior. As mentioned before, we have two objectives to optimize the system. First is to make the top plate tilt to the desired position as soon as possible. The second objective is to have the top plate be as stable as possible at this desired position under the condition of any perturbation.

Based on these objectives, we present two control algorithms, combining both bang-bang control and Kalman closed loop feedback control. Inside the system, there are two controllers for realize these two algorithms. These two controllers are independent and separate from each other. The system feedback will be switched to either one depending on the value or the estimation of the performance index. This is shown in Figure 5-3

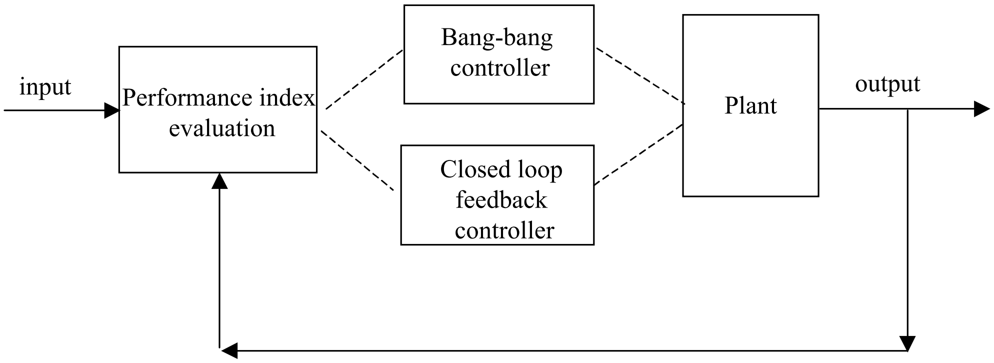

Figure 5-3 Integrating a bang-bang controller and a Kalman closed loop feedback controller

It is known from control theory that a bang-bang feedback control achieves the minimum time response; while a free final state needs Kalman closed loop-control to achieve system stable, (according to Lewis[71, pages 47-53]) . Thus, it is natural to integrate both of them in our optimal plate actuator system control. These two feedback modules are totally independent of each other. The system is monitoring a performance index constantly. The value of this performance index will determine in the next time period to which feedback control the system will go. Specifically, in our case here, the performance index is the following [71, page 161]:

$$J(t) = x(t)^T Px(t) - x_f^{\ T} P(t_0)x_f \tag{5-66-a}$$

where P is the matrix which determines the weight of each state component of $x(t_0)$. x_f is the final desired state with $x_{3f} = 0$. x_{2f} is the desired final position. As the accurately located position is the first control priority, P can be chosen as the following: $P = \begin{bmatrix} 0 & 0 & 0 \\ 0 & 1 & 0 \\ 0 & 0 & 1 \end{bmatrix}$. In this way, (5-66-a) becomes:

$$J(t) = x_2(t)^2 + x_3(t)^2 - x_{2f}^{\ 2} \qquad \text{(5-66-b)}$$

5.4.1 Bang-bang minimum time control

The first control objective is to make the top plate to move as fast as possible to the desired position. We have analyzed the transient response of the top plate in Chapter 4. There we have observed the oscillatory damping at the beginning time period after a step constant voltage is applied. This means that some settling time period is needed until the top plate is in an equilibrium status.

Obviously, these observations conflict with our system requirements to have the mirror tilt the desired position in a smooth and fast way. This introduce bang-bang optimal control to achieve the minimum switching time as mentioned in Elbert [50, pages 289 to 291] and Lewis [70, pages 259-280]. By using this control methodology, the input will be swung from the maximum value to the minimum value to reach a minimum time requirement. Assume that the top plate is at fixed at Vcc, the highest voltage. Then this algorithm suggests that the bottom plate should be driven by the zero (to reach the maximum potential difference) from the initial time t_i to some inter time t_m; and then the bottom plate should be driven by Vcc (to reach the minimum potential difference) from this inter item t_m to the final time t_f.

5.4.2 Kalman closed loop control at an equilibrium position

The objective for the Kalman closed loop control is to make the system stable to track some desired status, [70, pages 185-198]. When any perturbation appears, the system can automatically go back to its desired position by using this closed loop feedback control.

The system state equations (5-30) are nonlinear by nature. The control theory behind the closed loop feedback is based on linearization of the nonlinear system at its equilibrium point, which we have already used in (5-54) to proceed with our stability analysis ([50, pages 125-128]). Thus the system state equations considered here are (5-45) and (5-54), and rewrite here briefly:

$$A = \begin{bmatrix} \bar{x}_2 - \varphi_b & \bar{x}_1 & 0 \\ 0 & 0 & 1 \\ \bar{x}_1 & -\omega_J^2 & -2\bar{\tau}\omega_J \end{bmatrix} \tag{5-53}$$

$$\delta\dot{\xi} = A\delta\xi + B\delta\mu \tag{5-54}$$

The advantage of this method is that there are many optimal control tools available in the literatures of linear systems. The one utilized here is the optimal control law for free-final-state and closed loop control from Lewis [70, pages 170-173] for a linear system $\dot{\xi} = A\xi + B\mu$ with the performance index function:

$$J(t_0) = \frac{1}{2}\xi^T(T)S(T)\xi(T) + \frac{1}{2}\int_{t_0}^{T}\left(\xi^T(T)Q(T)\xi(T) + u^T(T)R(T)u(T)\right)dt \tag{5-67}$$

where T is the final time; $S(T)$ and $Q(T)$ are symmetric and positive semi-definite; $R(T)$ is symmetric and positive definite.

With the definition of Kalman gain K, a time variable.

$$K(t) = R^{-1}B^T S(t) \tag{5-68}$$

then the feedback law is

$$u(t) = -K(t)\xi(t) \tag{5-69}$$

In (5-68),

$$S(t) = S_T(T-t) \tag{5-70}$$

S_T is the solution to the matrix *Riccati* equation:

$$\dot{S}_T = A^T S_T + S_T A - S_T B R^{-1} B^T S_T + Q \tag{5-71}$$

We can use (5-68) to (5-69), (5-70) to find the optimal feedback control law for the system. In our case here, assume that the performance index has the coefficient matrix as the following, we can calculate K(t):

$$S(T) = \begin{bmatrix} 1 & 0 & 0 \\ 0 & 1 & 0 \\ 0 & 0 & 1 \end{bmatrix} \quad R(T) = Q(T) = \begin{bmatrix} 1 & 0 & 0 \\ 0 & 1 & 0 \\ 0 & 0 & 1 \end{bmatrix} \tag{5-72}$$

First, we will find S_T. By using (5-68) and (5-72), (5-71) becomes:

$$\dot{S}_T = A^T S_T + S_T A - {S_T}^2 + Q \tag{5-73}$$

According to Darling [72], the solution to (5-73) is

$$S_T = L^T X^{-1} \dot{X} L + \frac{1}{2}\left(A + A^T\right) \tag{5-74}$$

where L is given by

$$\dot{L} = \frac{1}{2} L\left(A - A^T\right) \text{ when } L(0) = I \tag{5-74-a}$$

and the Jacobi equation

$$\ddot{X} - XL\left(Q + A^T A + \frac{1}{4}\left(A - A^T\right)^2 + \frac{1}{2}\left(A^T + A\right)\right)L^T = 0 \tag{5-74-b}$$

Using the parameters available in our optimal plate actuator system, we can easily get the Kalman gain K(t) with the help of Matlab from the control tool box.

5.5 Feedback control system architecture to implement the optimal control methodologies

Having discussed the two control methodologies to optimally control the mirror actuator system, here we present the feedback control architecture with a microprocessor to implement them. Among the three state variables, the angular position α can be sensed by a sensing bridge circuit. Its velocity can be used as a first degree approximation $\dot{\alpha}(t_0) = \frac{\alpha(t_0) - \alpha(t_0 + \Delta t)}{\Delta t}$. The third state variable Q is obtained by using $Q = CV$, where C is given in Equation (5-5). With a microprocessor serving as the control core, the control methodologies discussed in the previous section can be implemented.

Accordingly, a precisely positioning sensor served in the feedback is critical for the success of this optimal control. As mentioned in Chapter 1, there is a threshed range problem for the position sensors in the light-power detection method. In this dissertation, we solve this sensing threshed problem by introducing a sensing capacitor. This sensing capacitor is located on the mirror. So any mirror position change will result in its capacitance change. By realizing that the Wheatstone bridge can precisely measure small value change in capacitance due to its high sensitivity [34] [43], an electrical sensing bridge is used here to sense the position of the mirror.

In a MEMS actuator system, the bottom plate is fixed in position while only the top mirror plate can tilt. We know that there is a one to one relationship between the position of the top mirror and its capacitance to the substrate. So this capacitance seems to be the candidate to fulfill the job of position sensing at a first thought. However, in order to perform measurement using the bridge circuit, a high frequency signal source is needed to drive the bridge. Thus a separate sensing capacitor for position sensing is utilized in this dissertation.

One pad of this sensing capacitor is located on the mirror and the other pad is located on the substrate right below. The position of the mirror plate can be detected from the capacitance C_s of this sensing capacitor. Different mirror position results in different C_s. There is no position limitation of the outgoing light beam for this sensing capacitor to detect. Thus this detection method successfully eliminates the problem regarding to the threshed position as mentioned in Chapter 1. By using such a sensing capacitor, the feedback control is functional during the full traveling range of the mirror. Without any optical components (such as a top module), this method makes possible systems on a chip in the future.

5.5.1 A sensing capacitor

Before we outline the implementation architecture of the optimal control methodology, we will study in detail the sensing capacitor. We will answer the questions such as what its structure is and how it works.

Because a high frequency signal is needed to a drive a capacitance load during the measurement, in order to avoid the disturbance between the main mirror capacitance and other noise, a separate sensing capacitor C_s is used instead of using the direct capacitance between the top plate and the bottom plate. For this sensing capacitor, one of its pads, which is a narrow strip, is located at the end of the top mirror plate directly. The other pad C_s, which is another narrow metal strip, is located on the substrate, right underneath the top strip. There is electrical isolation between the top mirror plate electrode and the top electrode of this sensing capacitor, while there is electrical isolation between the bottom actuation electrode plate and the bottom pad of this sensing capacitor.

Several points need to be mentioned about Figure 5-4. First, it is not to scale. Second, for simplification purpose, no suspension structure is plotted. Third, for symmetry purpose, four sensing capacitors are plotted. However, only one sensing capacitor is needed to detect the position of the top mirror plate, due to the one rotation axis of the top plate.

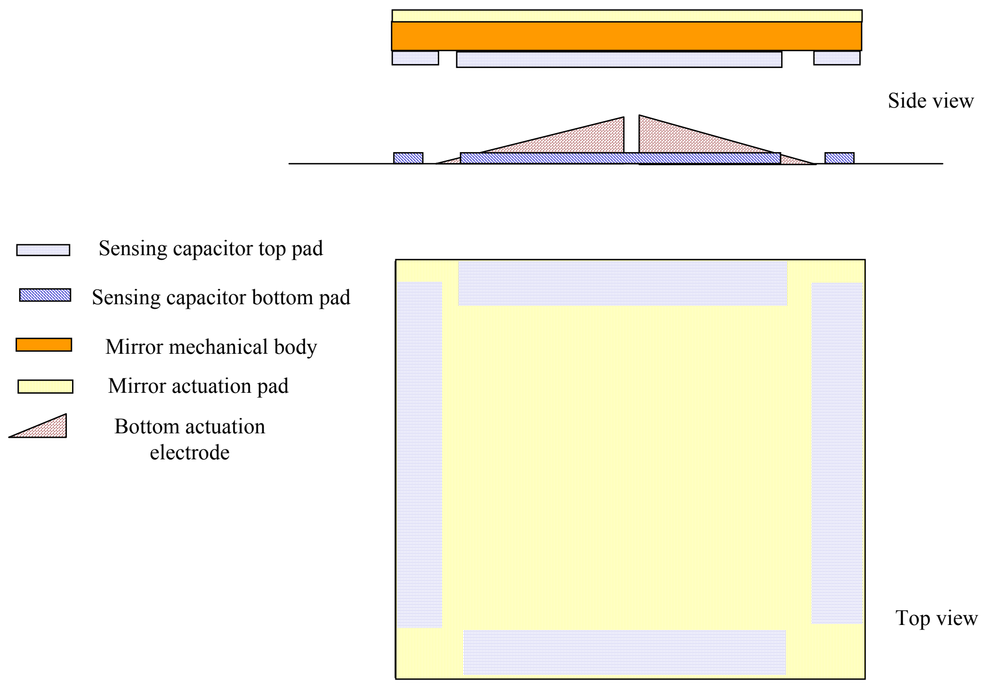

Figure 5-4 The side view and top view of the mirror top plate with the sensing capacitor

The sensing capacitor introduced above has the ability to sense the position of the top plate. However, the magnitude of such sensing capacitance is quite small. For example, for a top pad with dimension of 218μm long and 10μm wide, the calculated capacitance is

$$C_s \approx \frac{\varepsilon \cdot A}{d} = \frac{\varepsilon \cdot W_s \cdot L_s}{d} = \frac{8.854\times10^{-12}\cdot\left(218\times10^{-6}\right)\cdot\left(10\times10^{-6}\right)}{40\times10^{-6}} = 4.83\times10^{-16}\,\mathrm{F}$$

This means that the sensing capacitance is in the order of fF, a small value. To make things worse, there is always some parasitic capacitance in the system. To answer this challenge, a sensing bridge is used in the control system as shown in Figure 5-5. The sensor capacitor forms one arm of the bridge Z_4.

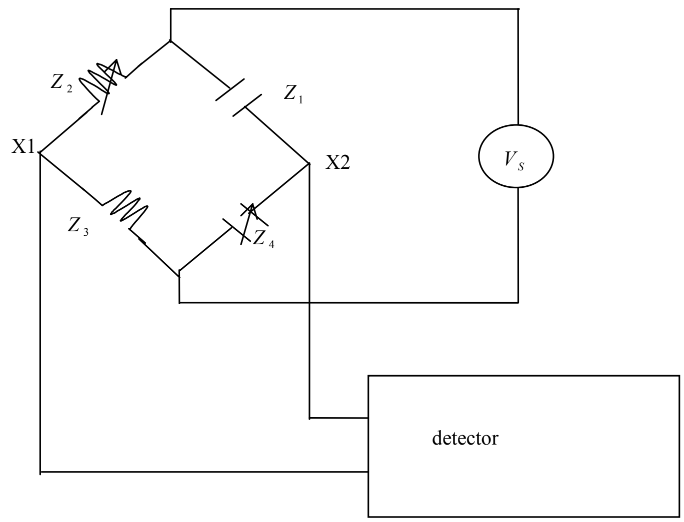

Figure 5-5 The Wheatstone bridge circuit

The bridge is balanced when $Z_4 Z_2 = Z_3 Z_1$. Then $V_{X2} = V_{X1}$, referenced to ground, at this time, the detected voltage difference between node X1 and node X2 will be zero. Normally in such a bridge, Z_1 and Z_3 are fixed in values. If Z_4 is changed, a change of Z_2 will need to be made to keep the bridge balanced. This is exactly the case in our position sensing. When Z_4 is changed due to the mirror movement, the bridge is out of balance. At this time, if Z_2 is kept constant, there will be a voltage difference between V_{X1} and V_{X2}. When Z_2 is changed accordingly until a balance bridge is satisfied, no voltage difference will be detected at the detector, and the value of Z_4 is calculated as $Z_4 = Z_3 \cdot \frac{Z_1}{Z_2}$.

5.5.2 A testing capacitor structure

To implement the Wheatstone bridge in our control system, when the sensing capacitor is used as one arm of Z_4, another three arms need to be selected. As discussed above, to keep the bridge balanced when Z_4 is changed, Z_2 has to be changed. In the meantime, we choose constant capacitance values in the arms of Z_1 and Z_3.

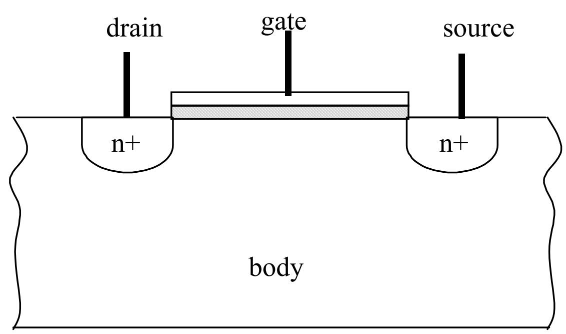

Figure 5-6 The testing resistor made from a MOSFET.

To realize such a variable impedance of arm Z_2 to balance the capacitor in the bridge, we introduce a variable resistance R_2, made from a MOSFET, with a structure shown in Figure 5-6. R_2 is the resistance between the drain and source of MOSFET M_1, which is in its triode region by applying appropriate gate voltage. In this way, different gate voltages applied on M_1 will result in different values of R_2. R_2 serves as Z_2 in the bridge.

So far, we have set the sensing capacitor as Z_4 and the MOSFET resistor R_2 as Z_2 in the bridge. Accordingly, we choose another identical structure MOSFET resistor R_1, and another capacitor C_3 as Z_3. Both R_1 and C_3 are constant values.

5.5.3 The feedback control architecture

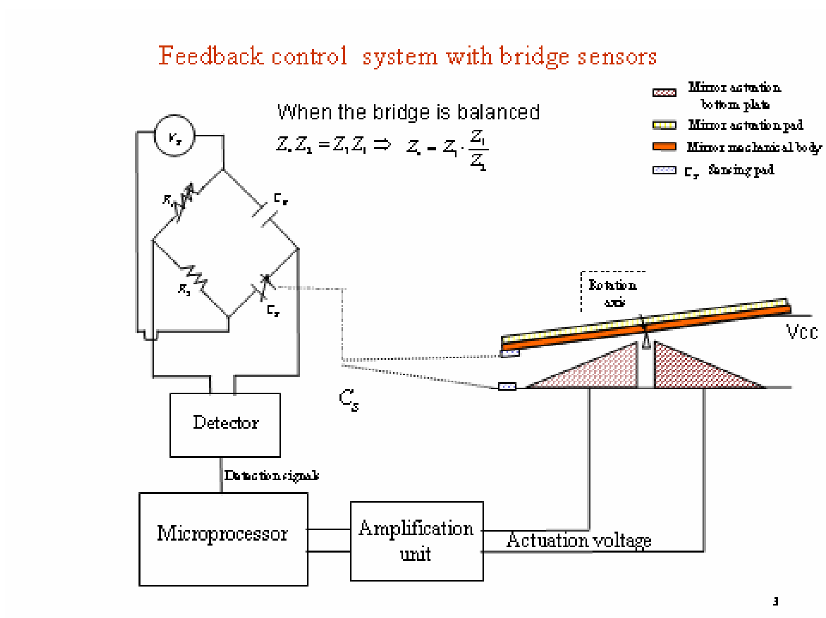

Figure 5-7 The architecture of the feedback control

Having discussed the sensing bridge, we are ready to determine the architecture of the feedback control for a MEMS mirror in a large count optical switch. This architecture is shown in Figure 5-7.

As shown in Figure 5-7, the feedback control schema is composed of several blocks. One block is the sensing bridge, which detects the angular position of the top mirror plate. Another block is the detection block, which filters out the noise and amplifies the position signals. These sensing signals are translated to digital signals and are sent to the controller block. The controller block receives these angular position signals, calculates the corresponding two other state variables, and then determines the required driving voltage based on the optimal control methodologies. Then through a Digital to Analog converter (DAC), the control block sends out the driving voltage to the bottom plate. (Top plate is applied a fixed Vcc). The electrical potential difference between this driving voltage and Vcc will determine the angular position of the top mirror plate.

As shown in Figure 5-7, the sensing pads can detect every angle through which the mirror turns. The sensing bridge is composed of four components. C_s is the sensing capacitor. R_1 is a variable resistor made from a MOSFET. The MOSFET's gate voltage determines the value of $R_1 . C_b$ is a fixed value balancing capacitor. R_2 is fixed value balancing resistor made from another MOSFET. C_s is located at the edge of the mirror. C_b, R_1, R_2 are located outside of the mirror.

A high frequency signal source drives the sensing bridge. Initially, the sensing bridge is balanced. The working function of the sensing bridge is illustrated in two cases. In one case, there is noise applied on the mirror plate. The mirror changes its angular position, deviating from its stable position. A change in C_s makes the bridge unbalanced, which means a voltage drop between V_{X1} and V_{X2}. As long as this voltage difference is detected by the detection circuitry, these analog signals are sent to the controller block, where these analog signals are sampled and converted to digital signals and are processed based on the optimal control methodology. An optimal driving voltage is then calculated and sent to the bottom plate. This brings the top mirror back to its originally stable position. During this process, the variable resistance R_1 is unchanged.

In anther case, there is a system command from the microprocessor to have the mirror switch the light beam from one channel to another channel, making the top mirror travel a rather large angular position. With this system command, a new R_1 is calculated by the microprocessor, and its new control gate voltage is sent to the MOSFET M_1. At the same time, the sensing circuitry senses the voltage drop between V_{X1} and V_{X2}. The microprocessor, just as in case one, processes these sensing signals on the basis of the optimal control methodologies. The optimal driving voltage is then calculated and sent to the bottom plate. This brings the top mirror quickly switched to the desired new position.

So far, we have studied the feedback control architecture of the MEMS mirror actuators and we have mentioned that the microprocessor sends the optimal driving voltages to the mirror actuators. We have already discussed in previous chapters that these driving voltages normally is high in value. Recall both the microprocessor and DAC have a limited range in output voltages. Thus there is a need to amplify these voltages up to the level of the high voltage range to drive the mirror actuators ultimately. In the next section, we will discuss the design of such high voltage drivers in this large channel count optical switch applications.

5.6 High voltage driving circuits for MEMS actuators

A MEMS based large channel count optical switch can consist of a large number of mirrors. Because the nature of repetition of the same driving circuits for hundreds or even thousands of mirrors, any effort reducing the complexity of such driving control circuits will result in great benefits for the system as a whole. This section will discuss the driving circuits for MEMS actuators. A circuit that can reduce by one-half the number of the driving control voltages is presented here.

First let us briefly review the system requirement on these high voltage drivers. The large channel count optical switch has put the demand that the driving circuits need to be simple so that they can be small in size and low in power consumption. Also the circuit should be easy to be integrated with other parts of the system, ideally, the whole system integrated in a chip. Plus, the driving circuits should stand high voltages up to two to three hundred volts. A high voltage driving circuit proposed here has very simple analog circuit architecture, reduces by half number of the voltage control signals and eliminates the digital control bit needed to select the two electro-plates for each mirror. Another benefit of this driver is its potential to be integrated with all the other circuits of the system in one single IC chip to ultimately achieve a SoC.

5.6.1 A featured high voltage driving circuit

Our design of the high voltage driving circuit has the architecture, as shown in Figure 5.8. It is based on the observation that only one electro-plate out of the two electro-plates labeled as A and B is actuated at some specific time as mentioned in Chapter 2. Thus one analog voltage controller is needed to drive the bottom plate A or B. Additionally, a one-bit digital control signal is needed to distinguish between bottom plate A or B.

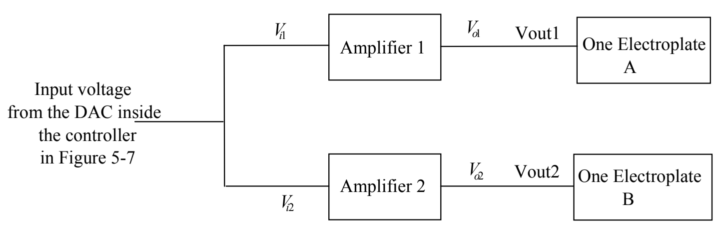

Figure 5-8 One cell of high voltage driving circuits with one input port and two output ports

The proposed high voltage driving circuit is composed of two amplifiers with one common input port, as shown in Figure 5-8. Figure 5-8 is one cell of such driving circuits.

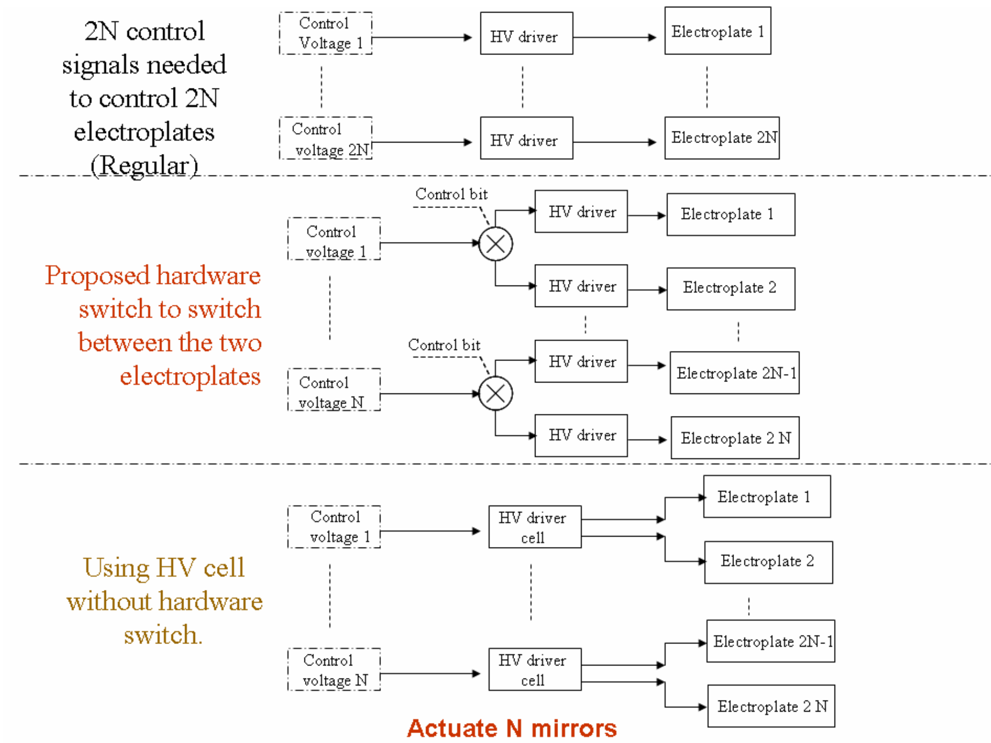

Figure 5-9 Comparison between the new and standard high voltage driving circuits to actuator N mirrors

Figure 5-9 shows a comparison between the new high voltage driving circuits and the regular ones to actuate N mirrors. In the regular high voltage driving circuits, 2N driving control signals are needed to drive N mirrors. Each mirror has two bottom plates, with a total 2N bottom plates. As the two bottom plates are mutually exclusively actuated, N hardware switches can used to cut the driving control signals by half to N, with an introduction of N digital control signals to switch between the two bottom plates A or B of each mirror.

By introducing a new high voltage driving circuit, the driving control signals are still be N while the N digital control signals for selecting between A or B Bottom plate have been eliminated. Thus our new high voltage driving circuit can reduce half the number of the driving control signals while eliminates the digital control bit to select one of the bottom plates in each mirror.

In Figure 5-8, the input comes from the DAC inside the controller in Figure 5-7. Both amplifiers in the circuit have the same output voltage range, which is the desired voltage to drive the micro mirrors in an optical switch. Here is the working principle of the circuit.

Assume the gain of the first and the second amplifiers are g_1 and g_2 respectively, and the desired output driving voltage range is for both from Vo_L to Vo_R volt, that is

$$V_{o_1} \in (V_{O_L}, V_{o_R}) \text{, and } V_{o_2} \in (V_{O_L}, V_{o_R}) \tag{5-75}$$

where V_{o_1}, V_{o_2} are the output voltages of the first and the second amplifiers respectively, and Vo_L, Vo_R are the lower and upper bound of the desired mirror driving voltage range. The input of both the amplifiers will range from

$$V_{s_n} + \frac{V_{O_L}}{g_n} \text{ to } V_{s_n} + \frac{V_{O_R}}{g_n},\ n \in (1,2) \tag{5-76}$$

where V_{s_n} is the DC offset of amplifier n.

Therefore

$$V_{i_1} \in (V_{s_1} + \frac{V_{O_L}}{g_1}, V_{s_1} + \frac{V_{O_R}}{g_1}), \text{ and } V_{i_2} \in (V_{s_2} + \frac{V_{O_L}}{g_2}, V_{s_2} + \frac{V_{O_R}}{g_2}) \quad (5\text{-}77)$$

where V_{i_1}, V_{i_2} are input voltages of the first and the second amplifiers.

The first and the second amplifier are designed to activate at mutually exclusive input signal ranges. Therefore, while one amplifier is actuated, the other will be cut off, and vice versa. That is

$$V_{i_1} \notin (V_{s_2} + \frac{V_{O_L}}{g_2}, V_{s_2} + \frac{V_{O_R}}{g_2}),\ V_{i_1} \notin (V_{s_1} + \frac{V_{O_L}}{g_1}, V_{s_1} + \frac{V_{O_R}}{g_1}) \quad (5\text{-}78)$$

Or

$$(\frac{V_{O_L}}{g_1}, \frac{V_{O_R}}{g_1}) \bigcap (\frac{V_{O_L}}{g_2}, \frac{V_{O_R}}{g_2}) = \phi \quad (5\text{-}79\text{-a})$$

$$V_{s_1} + \frac{V_{O_L}}{g_1} = V_{s_2} + \frac{V_{O_R}}{g_2} \quad (5\text{-}79\text{-b})$$

With this feature, the control input range can be determined in the following way:

1) Shift the desired input signal for the first amplifier into the range

$(V_{s_1} + \frac{V_{O_L}}{g_1}, V_{s_1} + \frac{V_{O_R}}{g_1})$,

2) Shift the desired input signal for the second amplifier into the range

$(V_{s_2} + \frac{V_{O_L}}{g_2}, V_{s_2} \frac{V_{O_R}}{g_2})$

3) Add these two ranges together.

Therefore, with one input port without introducing any digital control bits, the circuit can be used to drive two different actuators working mutually in time. In this way, an automatic distinguish ability between two outputs is implemented and the need of one bit digital selecting signal is eliminated.

5.6.2 Implementation of a high voltage driver and its simulation results

A design example is given here. Assume we have the following parameter requirements:

$$\begin{cases} V_{o_L} = 0V \\ V_{o_R} = 300V \end{cases} \tag{5-80}$$

Let

$$g_1 = 60\,,\ g_2 = 60\,,\ V_{s_1} = 1V\ ,\ V_{s_2} = -4V \tag{5-81}$$

For the second amplifier,

$$V_{i_1} \in (V_{s_1} + \frac{V_{o_L}}{g_1}, V_{s_1} + \frac{V_{o_R}}{g_1}) \quad = (1 + \frac{0}{60}, 1 + \frac{300}{60}) = (1,6) \tag{5-82}$$

For the second amplifier,

$$V_{i_2} \in (V_{s_2} + \frac{V_{o_L}}{g_2}, V_{s_1} + \frac{V_{o_R}}{g_2}) \quad = (-4 + \frac{0}{60}, -4 + \frac{300}{60}) = (-4,1) \tag{5-83}$$

Combining (5-82) and (5-83), then we have $V_{i_n} \in (-4V, 6V)$

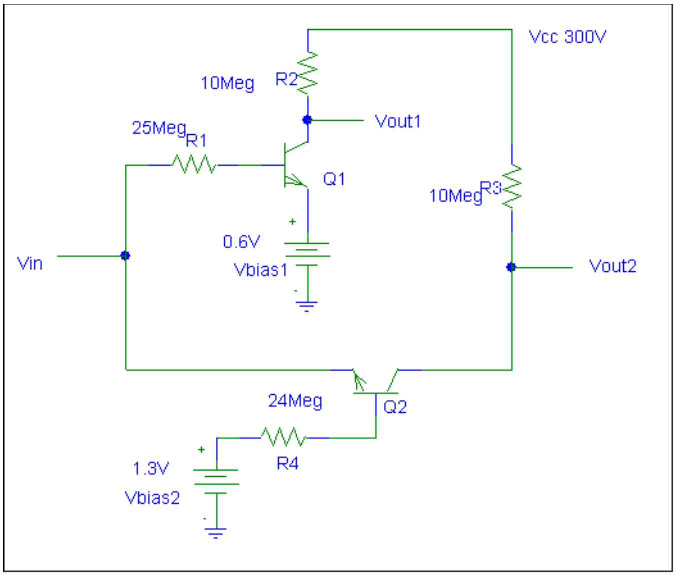

Figure 5-10 A cell circuit for MEMS actuation

One such cell is needed for each mirror actuator system because of two bottom electro-plates in each mirror system.

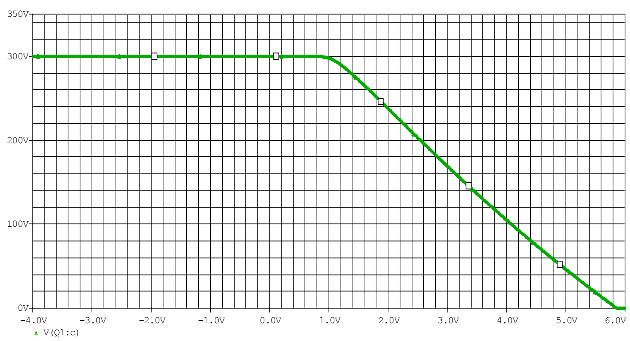

(a) DC sweep (V_{OUT1} vs. V_{in}) of the high voltage driver circuit with input sweep from -4V to 6V

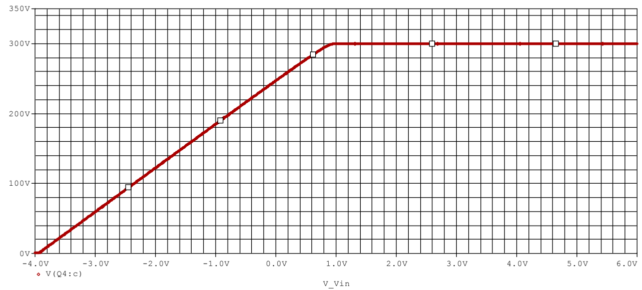

(b) DC sweep (V_{OUT2} vs. V_{in}) of the high voltage driver circuit with input sweep from -4V to 6V

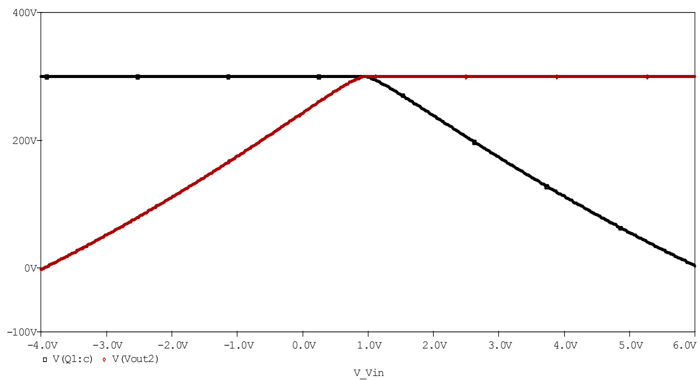

(c) V_{OUT1} and V_{OUT2} DC sweeping for the whole input range

Figure 5-11 DC sweep using PSpice simulation

One of the simplest implementation of Figure 5-8 is shown in Figure 5-10 with Bipolar transistors in discrete components. There are only two transistors Q1 and Q2, along with four additional resistors to drive the two independent and mutually exclusive working electro-plates. Both Q1 and Q2 share the same input Vin. Properly biased, this circuit can generate the needed high voltage for the electro-plates in the mirror actuator system, which are labeled V_{OUT1} and V_{OUT2} here, as shown in Figure 5-10. In future work, a MOSFET circuit can be implemented to achieve a SoC.

The simulations using PSpice for the circuit shown in Figure 5-10 is displayed in Figure 5-10. We can assume that V_{cc} in Figure 5-10 is 300V and assume that the top mirror plate is biased to V_{cc} (300V). The desired output range for both electro-plates is (0V, V_{cc}). When the input changes from –4V to 1V, which is the desired input signal range for the second amplifier, V_{OUT2}, the output from Q2 changes from 0V to V_{cc}, linearly with the input change. At the same time, the output of the first amplifier, V_{OUT1}, which is the output of Q1, keeps constant at V_{cc}. As we bias the top mirror at fixed V_{cc} DC voltage, then this means that no potential difference between the first electro-plate and the mirror plate, resulting no electrostatic actuation. When the input changes from 1V to 6V, which is the desired input range for the first amplifier, the output of the first amplifier, V_{OUT1}, drops linearly from V_{cc} to 0V. The first electro-plate is now being actuated by V_{OUT1}, while the output of the second amplifier, which is the output from Q2, keeps the constant voltage level at V_{cc}. This results in no actuation due to the second electro-plate.

After a brief explanation of the working principle of the cell circuit shown in Figure 5-10, we will detail its analysis. Specifically, we will give its design principle based on power consumption. First assume that this circuit is designed for a 256x256 optical switch system. There will be 256 input mirrors and 256 output mirrors with $2N$ structure. As mentioned in Chapter 2, each mirror actuator system is composed of one top mirror and two bottom electro-plates. The top mirror is biased to V_{CC}, while each bottom plate is connected to a high voltage driving circuit, which is mutually exclusively actuated. One such cell is needed for each mirror. Thus the total number needed for the high voltage driving cell is $(256+256)=512$. Assume that the total power budget of all the high voltage cells is $P_W = 5W$. Then for each driver cell shown in Figure 5-10, the power budget is $P_c = \frac{5W}{512} = 0.00977W$. Notice that this is the power budget for the whole cell during any time, no matter what the status of each bipolar transistor Q1 and Q2 is. Additionally, assume that the amplifier gain β for both Q1 and Q2 is the same.

The input's working range is (V_{IN_L}, V_{IN_R}), that is (-4V, 6V) here. Assume at first, the input voltage is at the edge of V_{IN_L}. Then Q1 is cut off, because its base voltage is less than the turn-on V_{BE-on} threshold voltage. This results in $V_{OUT1} = V_{CC} = 300V$. However, Q2 is in its working range, because its base voltage is greater than its turn-on V_{BE-on} threshold voltage, and its $V_{BC} < 0$. Thus at this moment, V_{OUT2} will be $V_{OUT2} = V_{cc} - R_3 \cdot I_{C2}$.

$$V_{OUT2} = V_{CC} - I_{C2} \cdot R_3 \tag{5-84}$$

To fit our design goal, it is required

$$V_{OUT2} \approx 0V \tag{5-85}$$

Because Q1 is cut off, and the electro-plate serves as a capacitor load, there is no current flowing except some ignorable leakage current. Thus at this moment, the circuit for the first channel V_{OUT1} consumes no power. Q2 is in its active working range; As β of Q2 are normally above 100, so the power consumption on R_4 can be neglected compared with that of R_3. That is the power consumption of the cell circuits is mainly determined by its power consumption of R_3. Thus

$$R_3 \approx \frac{V_{CC}^{\ 2}}{Pc} \tag{5-86}$$

Using the power budget we have and the V_{CC} value, the value of R_3 can be determined.

If we increase V_{IN}, $V_{IN} > V_{IN\_L} = -4V$. The base of Q1 still has lower voltage than its emitter, Q1 remains cutoff. In the meantime, the emitter voltage at Q2 is decreased, due to the increase of V_{IN}. However, the input voltage still sets positive base-emitter voltage and a negative base-collector voltage of Q2. Q2 is in its working active range.

$$I_{B2} = \frac{V_{Bias2} - V_{IN} - V_{BE2}}{R_4} \tag{5-87}$$

$$I_{C2} = \beta I_{B2} \tag{5-88}$$

From the above two equations and (5-84), we can solve that

$$V_{OUT2} = V_{CC} - R3 \cdot \beta \frac{V_{Bias2} - V_{IN} - V_{BE2}}{R_4} \tag{5-88-a}$$

Or $$V_{OUT2} = V_{CC} + \frac{R3 \cdot \beta}{R_4}\left(V_{IN} - V_{Bias2} + V_{BE2}\right) \quad \text{(5-89-b)}$$

The power consumption of the circuit during this linear range is composed of the power consumption in R_3 and R_4. As β of Q1 and Q2 are normally above 100, so the power consumption on R_4 can be neglected compared with that of R_3. Then we have the relationship to determine the value of R4:

$$P = P_{R3} + P_{R4} = I_{C2}{}^2 \cdot R_3 + I_{B2}{}^2 \cdot R_4 \approx \left(\beta \frac{V_{Bias2} - V_{IN} - V_{BE2}}{R_4}\right)^2 \cdot R_3 \le P_c \quad \text{(5-90-a)}$$

Or $$R_4 \ge \beta\left(V_{Bias2} - V_{IN} - V_{BE2}\right) \cdot \sqrt{\frac{R_3}{P_c}} \quad \text{(5-90-b)}$$

Or $$R_4 \ge \beta\left(V_{Bias2} - V_{IN\_\min} - V_{BE2}\right) \cdot \sqrt{\frac{R_3}{P_c}} \quad \text{(5-90-c)}$$

From (5-89), we can tell that there is a linear relationship between V_{OUT2} and V_{IN}. This is exactly the linear range shown in Figure 5-11 (b). In estimation of R_4 using (5-90-b), $V_{IN\_\min}$ should be used to keep the power consumption under budget. With the increase of V_{IN}, V_{OUT2} increases accordingly, while V_{BE2} is decreased, until to the point where $V_{BE2} = V_{BE-on}$. This is the point where Q2 will go into cut off with any more increase of V_{IN}. At the same time, when V_{IN} increases, the base voltage of R_1 increases. When it is higher than the threshold voltage of Q1, Q1 begins to work in the active range. In our design, we want to set the V_{IN} point when Q2 cuts off as the exact V_{IN} point when Q1 is turned on to the active range. That is if $V_{IN} = V_{IN\_T} = 1V$, then $V_{OUT2} = V_{CC} = 300V$ and $V_{BE2} = V_{BE-on}$. This requires that (5-89) becomes

$$V_{OUT2} = V_{CC} + \frac{R3 \cdot \beta}{R_4}\left(V_{IN} - V_{Bias2} + V_{BE-on}\right) = V_{CC}$$

Or
$$V_{IN\_T} - V_{Bias2} + V_{BE-on} = 0 \tag{5-91-a}$$

Or
$$V_{Bias2} = V_{IN\_T} + V_{BE-on} \tag{5-91-b}$$

For Q1, in order to have $V_{BE1} = V_{BE-on}$ at $V_{IN} = V_{IN\_T}$, then it requires

$$V_{BE1} = V_{IN\_T} - V_{Bias1} = V_{BE-on} \tag{5-92-a}$$

Or
$$V_{Bias1} = V_{IN\_T} - V_{BE-on1} \tag{5-92-b}$$

After the point $V_{IN} = V_{IN\_T}$, if V_{IN} continues to increase, Q2 will completely cut off and Q1 is completely in the active work range. For Q1, we have

$$V_{OUT1} = V_{CC} - I_{C1} \cdot R2 \tag{5-93}$$

$$I_{B1} = \frac{V_{IN} - V_{Bias1} - V_{BE1}}{R_1} \tag{5-94}$$

$$I_{C1} = \beta I_{B1} \tag{5-95}$$

Combining these three equations, we have:

$$V_{OUT1} = V_{CC} - \frac{\beta R2}{R_1}\left(V_{IN} - V_{Bias1} - V_{BE1}\right) \tag{5-96}$$

Equation (5-96) shows that with the continuous increase of V_{IN} after $V_{IN} = V_{IN\_T}$, there is a linear relationship between V_{OUT1} and V_{IN}. V_{OUT1} is decreased as a result of the increase of V_{IN}. This is exactly the linear range shown in Figure 5-11 (a). At this moment, the power consumption of the cell is mainly due to power consumption of R2. Then we have

$$P = P_{R1} + P_{R2} = I_{C1}{}^2 \cdot R_2 + I_{B2}{}^2 \cdot R_1 \approx \left(\beta \frac{V_{IN} - V_{Bias2} - V_{BE2}}{R_1} \right)^2 \cdot R_2 \le P_c \qquad \text{(5-97-a)}$$

Or $$R_1 \ge \beta \left(V_{IN} - V_{Bias2} - V_{BE2} \right) \sqrt{\frac{R_2}{P_c}} \qquad \text{(5-97 -b)}$$

Or $$R_1 \ge \beta \left(V_{IN\_\max} - V_{Bias2} - V_{BE2} \right) \sqrt{\frac{R_2}{P_c}} \qquad \text{(5-97 -c)}$$

Equation (5-97-c) is what we have obtained about the relationship between R1 and the power consumption. The highest value of V_{IN} should be used to guarantee the power consumption is limited by Pc. So the value of R1 can be determined if other parameters are known.

If V_{IN} increases more, at the point $V_{IN} = V_{IN\_R}$, Q1 enters saturation. The equations (5-93), (5-94), (5-95) do not hold any more. At that moment, V_{OUT1} will be the saturation voltage across Q1. This is normally a very small number, in the range of 0.1-0.3V, depending on the fabrication process of Q1. From (5-92-b), $V_{Bias1} = V_{IN\_T} - V_{BE-on1}$, which is a very small number, We can write

$$V_{OUT1} = V_{CE1} + V_{Bias1} \approx 0V \qquad \text{(5-98)}$$

As Q2 is cut off and Q1 is saturated, the power consumption at this moment is mainly determined by the power consumption of R2. Thus

$$P_c = \frac{\left(V_{CC} - V_{CE1} - V_{Bias1}\right)^2}{R_2}$$

$$\text{Or} \qquad R_2 \approx \frac{V_{CC}^{\ 2}}{P_c} \tag{5-99}$$

Using the power budget we have and (5-99), the value of R2 can be determined. After the determination of R2, R1 can be known from (5-97).

So far we have finished the determination of each component inside the circuit shown in Figure 5-10. Table 5-5 is a summary. The corresponding PSpice simulation results are also presented.

$V_{CC} = 300V$, $P_c = \frac{10W}{1024} = 0.00977W$			
components	PSpice simulation	Calculated from the left column	Formulas derived
R_2	10Meg	9.3Meg	$R_2 = \frac{\left(V_{CC} - V_{CE1}\right)^2}{P_c}$ (5-99)
R_3	10Meg	9.3Meg	$R_3 \approx \frac{V_{CC}^{\ 2}}{Pc}$ (5-86)
V_{Bias2}	1.3V	1.7V	$V_{Bias2} = V_{IN\_T} + V_{BE2}$ (5-91-b)
V_{Bias1}	0.6V	0.3V	$V_{Bias1} = V_{IN\_T} - V_{T1}$ (5-92-b)
R_1	25Meg	16Meg	$R_1 \geq \beta\left(V_{IN\_\max} - V_{Bias2} - V_{BE2}\right)\sqrt{\frac{R_2}{P_c}}$ (5-97-c)
R_4	24Meg	16Meg	$R_4 \geq \beta\left(V_{Bias2} - V_{IN\_\min} - V_{BE2}\right)\cdot\sqrt{\frac{R_3}{P_c}}$ (5-90-b)

Table 5-4 Summary of the design equations for the high voltage driving cell circuit

In this section, a high voltage driving circuit cell, which meets the special requirements of large channel count MEMS based optical switches, has been presented. The circuit is very simple in architecture; therefore, it can be easily integrated with other parts of the system and meet the trend of integrating the whole system on a chip.

5.7 The modular architecture of a scalable embedded system

In previous sections, we have mentioned that a microprocessor is inside the control block when we illustrated the feedback control architecture. To implement the feedback control architecture, to supply the optimal input to the high voltage driver, an embedded system is needed to control in real time. The embedded system for the MEMS actuator system is an important part of the embedded system for the whole optical switch system. Large channel count optical switches have put special demands on this embedded control systems for their scalability and reliability. It is cost and design preferable to add more modules in scalability for the increased number of channels based on the present system instead of starting from zero. Here "scalable" means the architecture can be scaled up or down to follow the requirements arising from different channel numbers. In this section, we will focus on the embedded control system in the MEMS actuator system. Specifically, we will study a modular architecture of scalable embedded systems using a shift register.

5.7.1 Objectives of the embedded system for MEMS actuators

The objective of the studied embedded system is to perform central control of the MEMS actuators to direct light beams and perform "switching" functions. Figure 5-12 gives the block diagram for the architecture of an embedded system for MEMS actuator control in large channel count optical switch applications. Besides the feedback control illustrated in Figure 5-7, this embedded system provides the control over other important issues in the system as well, such as the temperature control.

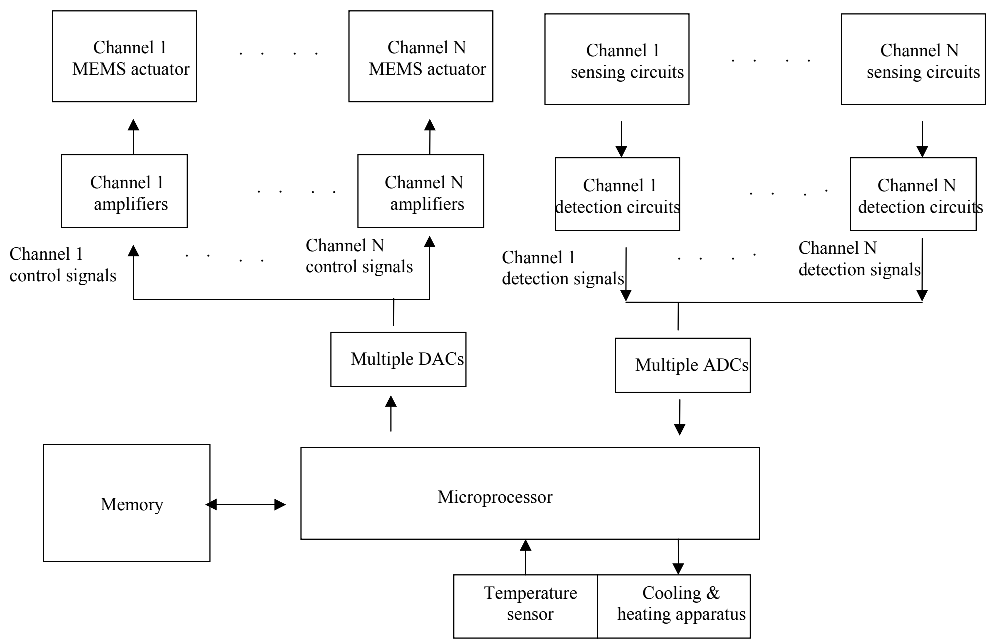

Figure 5-12 The embedded system for MEMS actuators in an optical switch

As shown in Figure 5-12, the control center of the embedded system is the microprocessor. It performs control algorithms and other system programs. Memory is for data and program storage. Sensing and detection circuits send the parameters of the mirror to the microprocessor. After the A/D converts these analog signals to digital signals, the microprocessor will process them with the optimal control algorithm. Initially, these are digital data. D/A converters (DACs) translate these digital data from the microprocessor to analog values in order to drive the amplifiers. The outputs from the amplifiers apply the required high voltages to drive the MEMS mirrors as in Figure 5-8. Also included in the architecture block is a temperature control subsystems. The register serves as a control buffer between the microprocessor and the targeted DACs.

We have illustrated the concept of embedded system for MEMS actuators in Chapter 2, where we pointed out the scalability is the goal for a good embedded system. Instead of using an embedded system targeted on a fixed number of channels, here a modular structure is illustrated by using a shift register. This will shorten the design cycle, increase the ability of easy maintenance, and reduce the system cost in the long run.

5.7.2 Descriptions of the modular structure of the embedded system

To solve the issue of limited capacity of output digital control ports of the microprocessor, we propose to use a serial shift register, as shown in Figure 5-13, to control between the microprocessor and DACs instead of using a decoder.

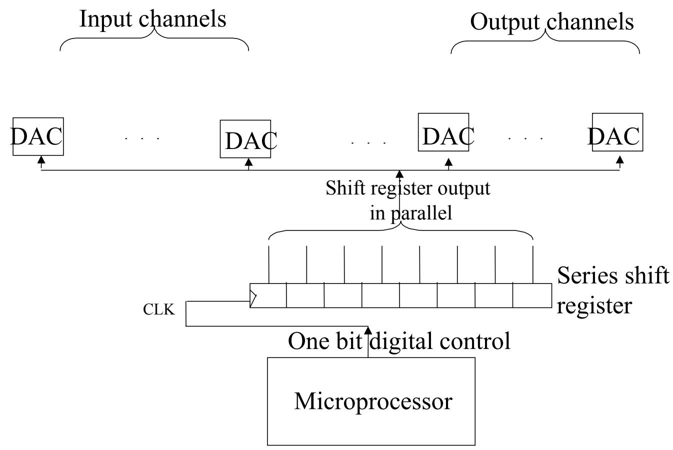

Figure 5-13 A series shift register used to get a modular structure of the embedded system

The function of a shift clock works in this way [37]. The shift register can shift either left or right depending on the chip configuration. We can assume that it is up as a left shift register. With each cycle of an incoming clock, the data inside the shift register will shift left by one bit. If wanted, at some specific clock cycle, all the data information can be sent out as a parallel output, as in Figure 5-13.

To select a specific DAC, the microprocessor provides the shift clock to the shift register, which has its parallel output wired to the chip enable pin of each DAC. Initially assume that all the data bits inside the shift register are all 0 except for only one 1. Assuming we use the left shift register, with each time a shift clock coming from the microprocessor, the data inside the shift register shifts one bit to the left.

The number of shift clock cycles determines which specific DAC is selected by setting the corresponding chip enable signal high.

In this configuration, when a need arises to increase the number of switch channels, no matter how many additional channels are needed, the hardware does not change at all except through adding more shift register bits while the software almost makes no change. No matter how many additional channels are needed, the microprocessor needs to provide only one digital control bit in this configuration. This one bit is used as the clock signal for the shift register. The modular structure is illustrated in Figure 5-14.

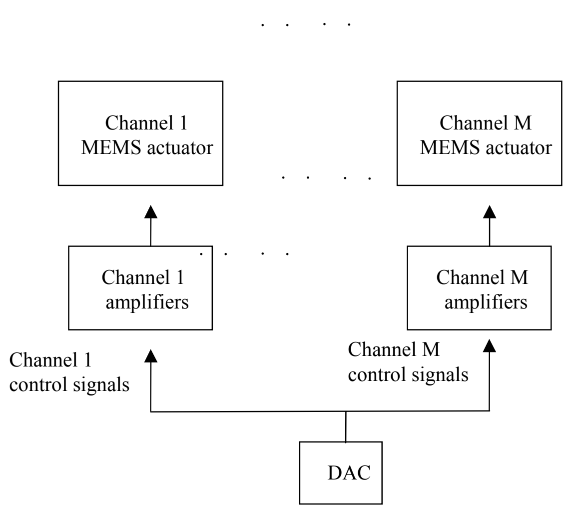

a) one module

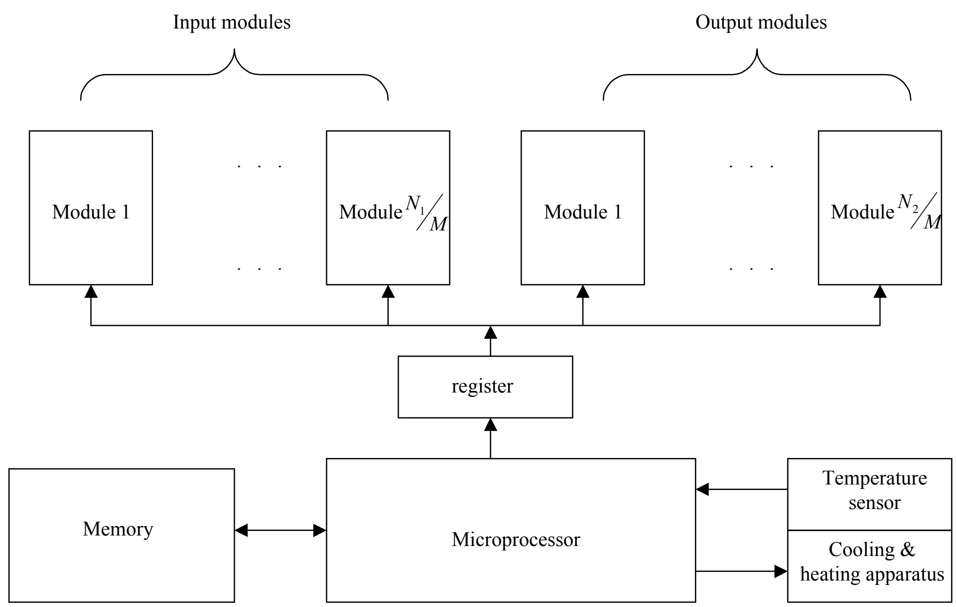

(b) The modular structure showing both input and output channels

Figure 5-14 A modular structure of the scalable embedded system
(M is the number of amplifiers that each DAC can drive)

Next, we will give an example to illustrate the idea with one-bit from the microprocessor to control the shift register. Let us assume that we work on a $N_1 \times N_2$ MEMS optical switch. Also assume that the total number of amplifiers driven by each DAC is M. There are altogether $N_1 + N_2$ mirrors in the system. From the discussion on the high voltage driving circuits in the previous section, we know that each mirror actuator needs one high voltage driving cell for its two bottom electro-plates, while the top mirror is at fixed electrical potential of Vcc. Each cell needs one input from the DAC. That is one inputs needed for each mirror actuator. Thus $(N_1 + N_2)/M$ DACs in a $N_1 \times N_2$ MEMS optical switch are needed.

In the modular structure shown in Figure 5-14, each module contains a DAC with M outputs. So each DAC can drive M high voltage cells and $2M$ MEMS electro-plates. That is each DAC to control M mirror actuators. The microprocessor provides one I/O port as the serial clock signal to shift the shift register. This one shift register can control up to S number of DAC, where S is the bit size of the shift register. We use the shift register in parallel output mode. Each bit of the output of the shift register is connected to the chip-selection pin of each DAC, and we set only one 1 for the data inside the shift register initially by a fixed hardware setting, as shown in Figure 5-15. In this way, the number of clocks will determine the specific DAC to be selected. Once a specific DAC has been chosen, consequently the specific driving cell and the electro-plates to be driven are determined. Again keep in mind that the clock to control the shifting comes from one digital control bit of the microprocessor.

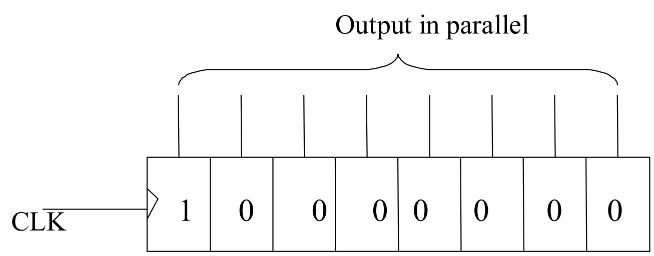

8 bit shift register with initialization

Figure 5-15 An example configuration of an 8-bit shift register

For example, if we are constructing a 256×256 optical switch, that is $N_1 = N_2 = 256$. So the number of input and output mirrors is each 256. The total number of mirrors is 512. If additionally the total number of outputs a single DAC can handle is 32, which means $M = 32$, the number of DACs needed for the input mirror is $\frac{256}{32} = 8$ and the DAC number needed for the output mirror is $\frac{256}{32} = 8$. Based on this calculation, two 8-bit serial shift registers will be used in the system. One is for the input DACs, and one for output DACs. They both have the same initialization as shown in Figure 5-15.

Suppose that the switch command is to switch input channel #33 to output channel #223. Each time the reset will set the register in the state of 1000,0000. As we want to select input channel #33, the 2nd input DAC will need to be selected. This requires the register to be in the state of 0000,0010, which can be realized by a left shift of two clocks cycles from its initial shift register status. As we want to select output channel #223, the 15th output DAC will need to be selected. This requires the register to be in the state of 0100,0000, which can be realized by a left shift of 15 bits from its initial shift register status by 15 clocks from the microprocessor. So the number of clock cycles sending from the microprocessor will determine the specific DAC to be selected.

This example shows how the system, specifically the serial shift register, performs in the modular structure. However, in the meantime, it also releases the tradeoff involved in using a scalable structure. Speed is scarified in an attempt to have a modular structure. Nevertheless, consider that the switching time of the mirror is in the range of ms and the shift clock frequency provided from the microprocessor is in the range of 100MHz [37]. Thus the time delay caused by each shift clock cycle is

$\frac{1}{100M} = 0.01\,\mu\text{s}$. Accordingly, this time delay due to the shift clock cycles is tolerable.

In the software part, everything is scalable if more clock cycles are needed to drive the register. The database structure inside the memory is scalable too as shown in Figure 5-16. When using this data structure, additional channels are easily considered by the software when N is a new number ($N \times N$ optical switch).

In this section, a modular structure of a scalable embedded system, which meets the special requirements of large channel count MEMS based optical switches, is presented. By using a shift register, the scalability in both hardware and software is achieved. Though the system might face a tradeoff in response time, this is not a big issue with the current technology for both MEMS and shift register. Therefore, it can meet the trend of integrating the whole system on chip.

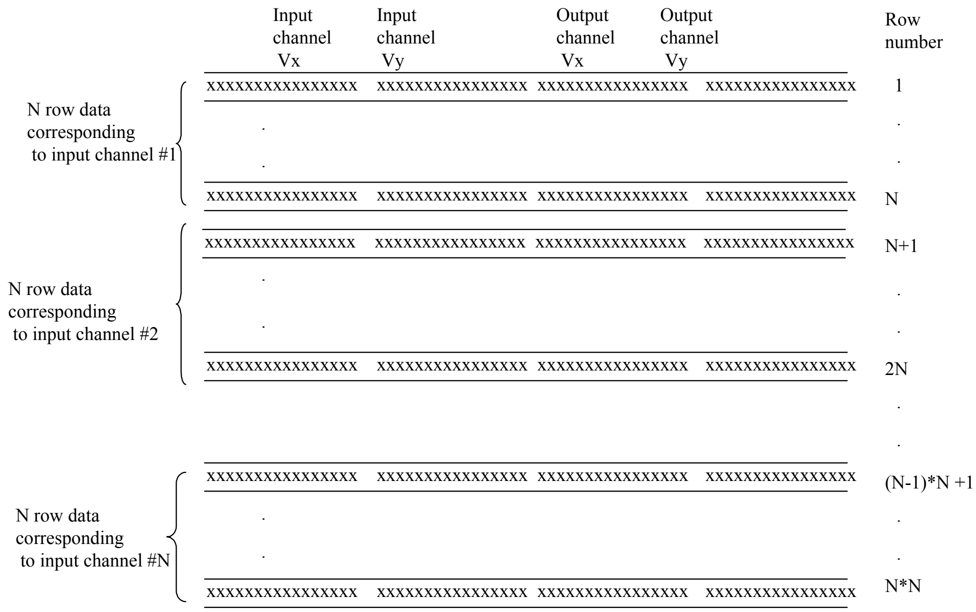

Figure 5-16 A data structure for the modular control of the MEMS actuators

5.8 Conclusions

We have covered the stability and control issues in the large channel count optical switch applications. From the view point of control theory, we have studied the stability of the optimal plate introduced in Chapter 3. Two control methodologies are applied to make the system immune to noise and any other disturbance. Implementation of these methodologies is realized by a feedback control architecture, which features a sensing bridge with a variable resistor made from a MOSFET and a variable sensing capacitor. Based on the special structural feature of the MEMS mirror introduced in Chapter 2, a novel high voltage driver is provided to cut the number of the required control actuating voltages by half and also to omit the digital control bit and the corresponding digital control circuits for each MEMS mirror. In the last section, a modular architecture of the scalable embedded system is introduced by using a shift register.

Chapter 6: Future Work and Conclusions

Abstract

This chapter summarizes the research work done in this dissertation. It also discusses the open problems in this area of actuating and to controlling MEMS mirrors in large-channel-number optical switches.

6.1 Conclusions

The research work performed in this dissertation is targeted on optimal control and actuation of a MEMS mirror plate in the applications of large-channel-number optical switches. An optimal electrostatic plate actuator is discussed in Chapter 3 along with a design methodology. After a force and torque analysis of three different configurations of the plate actuator, an optimal tilted bottom plate is presented to reduce the required driving actuating voltage by one-half of the present industry standard one. By considering planar fabrication processes available, a four-level stage structure is given as an example of a practical multi-step realization of such an optimal plate structure.

In Chapter 4, a transient analysis for the motion of the top plate in the optimal plate actuator is discussed with consideration of the squeeze film damping effects. The transient analysis is given for both the tilted bottom plate configuration and the horizontal bottom plate configuration. Their analogies to electrical circuits with

GVALUE components are recognized. Based on these, their transient responses are obtained from PSpice transient simulation.

In Chapter 5, the MEMS mirror system in control theory is investigated. When the internal conductance of the voltage source and the position-variation of the damping coefficients are considered, the analysis of the system, which is discussed in Chapters 3 and 4, is expanded further by using control state equations. Nonlinear state equations are presented after the introduction of the state variables. By using these nonlinear state equations directly, a Lyapunov function is investigated to confirm the system's stability in its working range. The Routh-Hurwitz test is performed to study the system stability after the linearization of the state equations at some equilibrium point.

By studying the special demands in large-channel-number optical switch applications, two optimal control methodologies are presented. A bang-bang control methodology is used to achieve fast settling time; while a feedback closed-loop control with real-time changing feedback gain is used to achieve the stability of the system when any perturbation appears. System architecture to implement these control methodologies is investigated. In this architecture, instead of using a popular mirror position sensor by using light power detection theory, an accurate sensing capacitor located on the mirror is introduced. The sensing capacitor is used in a sensing bridge circuit to detect the mirror position in real time. This mirror position information is fed back to the control microprocessor to be evaluated to determine the values of the actuating control voltages. Additionally, a new high voltage driving circuit is introduced and analyzed to cut these actuating control signal numbers by one-half along with the elimination of the control digital bit for each MEMS mirror system. This circuit also benefits the SoC concept for the whole system. Further, by using a shift register, a modular architecture of the embedded system, which produces a scalable structure, is presented in the last section. The system can be updated by adding more modules to the present system instead of starting from zero when there is a need to increase the channel numbers. This scalable embedded system is beneficial to cost reduction, future maintainability and design simplification.

6.2 Open problems for future study

Designing a successful MEMS mirror actuator system in the large-channel-number optical switch applications involves integrating electrical, mechanical, optical and control theories. The research of this dissertation has focused only on a few interesting areas, leaving various problems open to further work and study.

The number 1 problem is to analyze other 3D bottom plate structures, in addition to the one provided in Chapter 2. One such example is shown in Figure 6-1, in which case the mirror can perform a two-axis rotation. The structure of the bottom plate has the shape of a pyramid in Figure 6-1.

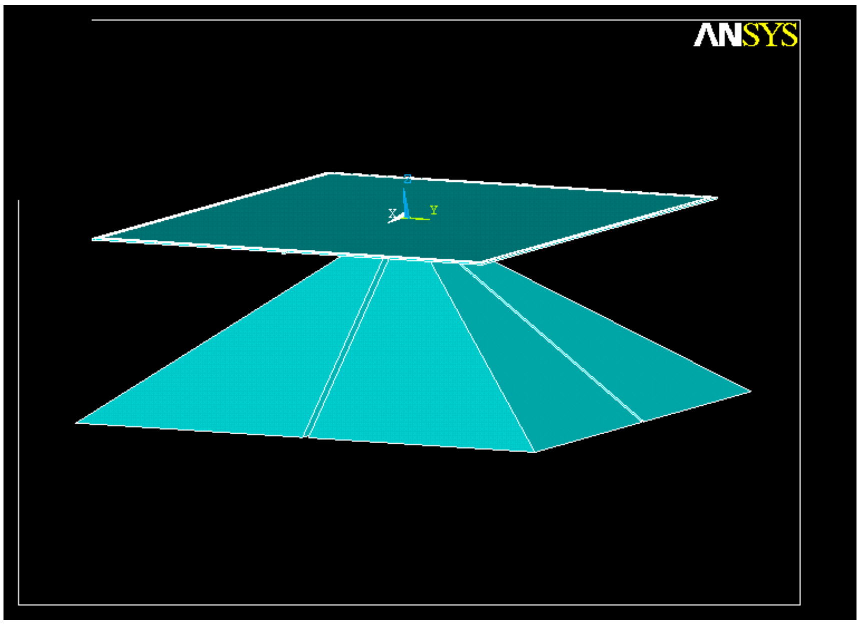

Figure 6-1 A 3D structure of the bottom plate for a MEMS mirror actuator

The number 2 problem is on system implementation of the architecture shown in Figure 5-8. More work can be done to detail this architecture's implementation, such as to fabricate the sensing capacitor and the variable MOSFET resistors, and to program software to implement the optimal control methodologies.

The number 3 problem is on how to interface both internally and externally. Due to the large number of MEMS mirrors and their control circuits involved in the large-channel-number optical switch applications, internally these control circuits need to have an interface to connect the mirrors and their associated electro-plates. Externally there is a packaging issue. This can be eventually solved by designing for a system on a chip (SoC).

The number 4 problem is related to fabricating mirrors. Even though MEMS manufacturing can be done using the present matured silicon planar technology, due to MEMS structure features there are special process problems to be solved to make MEMS fabrication as mature as its IC silicon process counterparts. In a MEMS mirror structure, complex geometries beyond the shape of thin plates are involved, such as the shape of a gimbal mount hinge. These require the fabrication processes involving a lot of etching and lifting, which make the MEMS fabrication quite different from its IC silicon counterpart. In addition, the large volume involved in IC technology helps to make the process mature quickly and to make the manufacturing price low. However, in the MEMS case, due to the low volume of products, MEMS products need a long time period for their fabrication to become as mature as their IC silicon counterparts.

The number 5 problem is on the mechanical and material analysis of the supporting gimbal mount hinge. Careful mechanical design needs to provide a smooth, reliable and functional suspension hinge during the whole life-time of optical switches, which is normally 20 years. Additionally, all the transient analyses we have covered here are based on the model of the squeeze film damping effects. Newly updated models to take care of the special shape of the bottom plate can help future system dynamical studies.

The number 6 problem is on the optical part. This is not covered in this dissertation. However, this part is important to the success of the whole system. The objective of a MEMS mirror is to direct light accurately from one input fiber to the desired output fiber in the large-channel-number optical switch applications. To achieve this objective, besides the optimal actuating and control matters discussed in this dissertation, there are challenges in optical alignment due to the involvement of a large quantity of optical fibers. Because the number of fibers involved is not trivial and the system's space is limited, a good optical path design including lens arrays and collimated fibers is critical to make the system successful with the required optical performance.

6.3 Summary

In summary, the demands arising from the high volume and high bit rate in transmitting information over optical fibers with the WDM and IP technologies have triggered the growth of a MEMS based OOO optical switch. As the key components in OOO optical switching, MEMS actuators provide the system with super-optical performance and low power consumption, which is especially beneficial to the large-channel-number optical switch applications. The MEMS based optical switch is the trend for the next generation of optical switch systems. As an integration of mechanical, electrical and optical components in a single system, MEMS actuators provide challenges along with opportunities to research and industry.

Appendix

This appendix is to provide the detail proof in Chapter 5 that

$$(a_3a_0 - a_2a_1) < 0 \qquad (5\text{-}59).$$

Let us look at $a_3a_0 - a_2a_1$

$$a_3a_0 - a_2a_1 = -\bar{x}_1^2 - \omega_J{}^2(\bar{x}_2 - \varphi_0) - (2\bar{\tau}\omega_J - (\bar{x}_2 - \varphi_0))(\omega_J{}^2 - 2\bar{\tau}\omega_J(\bar{x}_2 - \varphi_0))$$

$$= -3\omega_J{}^2\bar{x}_2 + \omega_J{}^2\varphi_0 - (2\bar{\tau}\omega_J - (\bar{x}_2 - \varphi_0))(\omega_J{}^2 - 2\bar{\tau}\omega_J(\bar{x}_2 - \varphi_0))$$

$$= \omega_J\left[-3\omega_J\bar{x}_2 + \omega_J\varphi_0 - (2\bar{\tau}\omega_J - (\bar{x}_2 - \varphi_0))(\omega_J - 2\bar{\tau}(\bar{x}_2 - \varphi_0))\right]$$

(A-1)

Because $\omega_J > 0$, To make $a_3a_0 - a_2a_1 < 0$, it requires that

$$\left[-3\omega_J\bar{x}_2 + \omega_J\varphi_0 - (2\bar{\tau}\omega_J - (\bar{x}_2 - \varphi_0))(\omega_J - 2\bar{\tau}(\bar{x}_2 - \varphi_0))\right] < 0 \qquad (A\text{-}2)$$

Or

$$-3\omega_J\bar{x}_2 + \omega_J\varphi_0 - (2\bar{\tau}\omega_J - (\bar{x}_2 - \varphi_0))(\omega_J - 2\bar{\tau}(\bar{x}_2 - \varphi_0)) < 0 \qquad (A\text{-}3)$$

Or

$$-3\omega_J\bar{x}_2 + \omega_J\varphi_0 - \left[2\bar{\tau}\omega_J^2 - 4\bar{\tau}^2\omega_J(\bar{x}_2 - \varphi_0) - \omega_J(\bar{x}_2 - \varphi_0) + 2\bar{\tau}(\bar{x}_2 - \varphi_0)^2\right] < 0$$

(A-4)

Or

$$-3\omega_J\bar{x}_2 + \omega_J\varphi_0 - \left[2\bar{\tau}\omega_J^2 - 4\bar{\tau}^2\omega_J(\bar{x}_2 - \varphi_0) - \omega_J(\bar{x}_2 - \varphi_0) + 2\bar{\tau}\bar{x}_2{}^2 - 4\bar{\tau}\bar{x}_2\varphi_0 + 2\bar{\tau}\varphi_0{}^2\right] < 0$$

Or

$$-3\omega_J\bar{x}_2+\omega_J\varphi_0-\left[2\bar{\tau}\omega_J^2-4\bar{\tau}^2\omega_J\bar{x}_2+4\bar{\tau}^2\omega_J\varphi_0-\omega_J\bar{x}_2+\omega_J\varphi_0+2\bar{\tau}\bar{x}_2{}^2-4\bar{\tau}\bar{x}_2\varphi_0+2\bar{\tau}\varphi_0{}^2\right]<0$$

(A-5)

Or

$$-2\bar{\tau}\bar{x}_2{}^2+\bar{x}_2\left[-2\omega_J+4\bar{\tau}^2\omega_J+4\bar{\tau}\varphi_0\right]-2\bar{\tau}\omega_J^2-4\bar{\tau}^2\omega_J\varphi_0-2\bar{\tau}\varphi_0{}^2<0 \qquad \text{(A-6)}$$

Or

$$-2\bar{\tau}\left[\bar{x}_2{}^2+\bar{x}_2\left(\frac{\omega_J}{\bar{\tau}}-2\bar{\tau}\omega_J-2\varphi_0\right)+\omega_J^2+2\bar{\tau}\omega_J\varphi_0+\varphi_0{}^2\right]<0 \qquad \text{(A-7)}$$

Or

$$-2\bar{\tau}\left[\begin{array}{l}\bar{x}_2{}^2+\bar{x}_2\left(\frac{\omega_J}{\bar{\tau}}-2\bar{\tau}\omega_J-2\varphi_0\right)+\left(\frac{\omega_J}{2\bar{\tau}}-\bar{\tau}\omega_J-\varphi_0\right)^2+\omega_J^2+2\bar{\tau}\omega_J\varphi_0+\varphi_0{}^2\\-\left(\frac{\omega_J}{2\bar{\tau}}-\bar{\tau}\omega_J-\varphi_0\right)^2\end{array}\right]<0$$

(A-8)

because $\bar{\tau}>0$ Then it requires

$$\left[\begin{array}{l}\bar{x}_2{}^2+\bar{x}_2\left(\frac{\omega_J}{\bar{\tau}}-2\bar{\tau}\omega_J-2\varphi_0\right)+\left(\frac{\omega_J}{2\bar{\tau}}-\bar{\tau}\omega_J-\varphi_0\right)^2+\omega_J^2+2\bar{\tau}\omega_J\varphi_0+\varphi_0{}^2\\-\left(\frac{\omega_J}{2\bar{\tau}}-\bar{\tau}\omega_J-\varphi_0\right)^2\end{array}\right]>0$$

(A-9)

Or

$$\left(\bar{x}_2 + \frac{\omega_J}{2\bar{\tau}} - \bar{\tau}\omega_J - \varphi\right)^2 + \omega_J^2 + 2\bar{\tau}\omega_J\varphi_0 + \varphi_0{}^2 - \left(\frac{\omega_J}{2\bar{\tau}} - \bar{\tau}\omega_J - \varphi_0\right)^2 > 0 \qquad \text{(A-10)}$$

Or

$$\left[\left(\bar{x}_2 + \frac{\omega_J}{2\bar{\tau}} - \bar{\tau}\omega_J - \varphi\right)^2 + \omega_J^2 + 2\bar{\tau}\omega_J\varphi_0 + \varphi_0{}^2 - \frac{\omega_J^2}{4\bar{\tau}^2} - \bar{\tau}^2\omega_J^2 - \varphi_0^2 + \omega_J^2 + \frac{\omega_J}{\bar{\tau}}\varphi_0 - 2\bar{\tau}\omega_J\varphi_0\right] > 0$$

(A-11)

Or

$$\left[\left(\bar{x}_2 + \frac{\omega_J}{2\bar{\tau}} - \bar{\tau}\omega_J - \varphi\right)^2 + 2\omega_J^2 - \frac{\omega_J^2}{4\bar{\tau}^2} - \bar{\tau}^2\omega_J^2 + \frac{\omega_J}{\bar{\tau}}\varphi_0\right] > 0$$

(A-12)

Or

$$\left(\bar{x}_2 + \frac{\omega_J}{2\bar{\tau}} - \bar{\tau}\omega_J - \varphi\right)^2 + \omega_J^2 - \frac{\omega_J^2}{4\bar{\tau}^2} + \omega_J^2 - \bar{\tau}^2\omega_J^2 + \frac{\omega_J}{\bar{\tau}}\varphi_0 > 0 \qquad \text{(A-13)}$$

Or

$$\left(\bar{x}_2 + \frac{\omega_J}{2\bar{\tau}} - \bar{\tau}\omega_J - \varphi\right)^2 + \omega_J^2 - \frac{\omega_J^2}{4\bar{\tau}^2} + \omega_J^2 - \bar{\tau}^2\omega_J^2 + \frac{\omega_J}{\bar{\tau}}\varphi_0 > 0 \qquad \text{(A-14)}$$

Since the first term is always not less than 0, if we can show the second term is greater than zero, then (A-14) holds. Let us look at the second term in (A-14)

$$\omega_J^2 - \frac{\omega_J^2}{4\bar{\tau}^2} + \omega_J^2 - \bar{\tau}^2\omega_J^2 + \frac{\omega_J}{\bar{\tau}}\varphi_0 > 0 \qquad \text{(A-15)}$$

Or

$$\omega_J\left(\omega_J - \frac{\omega_J}{4\bar{\tau}^2} - \bar{\tau}^2\omega_J + \frac{\varphi_0}{\bar{\tau}}\right) > 0 \tag{A-16}$$

Since $\omega_J > 0$, then it requires that:

$$\omega_J - \frac{\omega_J}{4\bar{\tau}^2} - \bar{\tau}^2\omega_J + \frac{\varphi_0}{\bar{\tau}} > 0 \tag{A-17}$$

In (A-17), there is $\bar{\tau}$. It is a function of $\bar{x}_2$, which is $\bar{\tau} = \frac{\tau}{\left(1 - \frac{\gamma}{\cos\beta}\bar{x}_2\right)^3}$. Since from (5-58), we know that there is a range for $\bar{x}_2$ $0 < \bar{x}_2 < \frac{\varphi_0}{3} = \frac{\beta}{3\gamma}$, then we can claim that there must be some bound to $\bar{\tau}$. In this way, we can prove the validity of (A-17). Notice $\gamma\bar{x}_2 = \bar{\alpha}$, $0 \le \bar{\alpha} < \frac{\beta}{3}$ then:

. $0 \le \frac{\bar{\alpha}}{\cos\beta} \le \frac{\beta}{3\cos\beta} \Rightarrow 1 - \frac{\beta}{3\cos\beta} \le 1 - \frac{\bar{\alpha}}{\cos\beta} \le 1 \Rightarrow$

$$\left(1 - \frac{\beta}{3\cos\beta}\right)^3 \le \left(1 - \frac{\bar{\alpha}}{\cos\beta}\right)^3 \le 1 \Rightarrow \frac{1}{\left(1 - \frac{\beta}{3\cos\beta}\right)^3} \ge \frac{1}{\left(1 - \frac{\bar{\alpha}}{\cos\beta}\right)^3} \ge 1 \Rightarrow$$

$$\frac{\tau}{\left(1 - \frac{\beta}{3\cos\beta}\right)^3} \ge \frac{\tau}{\left(1 - \frac{\bar{\alpha}}{\cos\beta}\right)^3} \ge \tau \Rightarrow \frac{\tau}{\left(1 - \frac{\beta}{3\cos\beta}\right)^3} \ge \bar{\tau} \ge \tau \tag{A-18}$$

Similar we can have:

$$-\frac{\tau^2}{\left(1 - \frac{\beta}{3\cos\beta}\right)^6} \ge -\bar{\tau}^2 \ge \tau^2 \Rightarrow -\frac{\tau^2}{\left(1 - \frac{\beta}{3\cos\beta}\right)^6} \le -\bar{\tau}^2 \le -\tau^2 \Rightarrow$$

$$-\frac{\tau^2\omega_J}{\left(1-\frac{\beta}{3\cos\beta}\right)^6} \le -\bar{\tau}^2\omega_J \le -\tau^2\omega_J \tag{A-19}$$

From (A-18), we have $\frac{\left(1-\frac{\beta}{3\cos\beta}\right)^3}{\tau} \le \frac{1}{\bar{\tau}} \le \frac{1}{\tau} \Rightarrow$

$$\frac{\left(1-\frac{\beta}{3\cos\beta}\right)^6}{\tau^2} \le \frac{1}{\bar{\tau}^2} \le \frac{1}{\tau^2} \Rightarrow \frac{-\left(1-\frac{\beta}{3\cos\beta}\right)^6\omega_J}{4\tau^2} \ge \frac{-\omega_J}{4\bar{\tau}^2} \ge \frac{-\omega_J}{4\tau^2} \tag{A-20}$$

From (A-18),

$$\frac{\left(1-\frac{\beta}{3\cos\beta}\right)^3}{\tau} \le \frac{1}{\bar{\tau}} \le \frac{1}{\tau} \Rightarrow \quad \frac{\left(1-\frac{\beta}{3\cos\beta}\right)^3\varphi_0}{\tau} \le \frac{\varphi_0}{\bar{\tau}} \le \frac{\varphi_0}{\tau} \tag{A-21}$$

Combining (A-21), (A-20) and (A-19), we can have that

$$-\frac{\tau^2\omega_J}{\left(1-\frac{\beta}{3\cos\beta}\right)^6} \le -\bar{\tau}^2\omega_J \le -\tau^2\omega_J \tag{A-22}$$

Related to (A-17), then we have

$$\begin{aligned} &\omega_J - \frac{\omega_J}{4\tau^2} + \frac{\varphi_0\left(1-\frac{\beta}{3\cos\beta}\right)^3}{\tau} - \frac{\tau^2\omega_J}{\left(1-\frac{\beta}{3\cos\beta}\right)^6} \\ &\le \omega_J - \frac{\omega_J}{4\bar{\tau}^2} - \bar{\tau}^2\omega_J + \frac{\varphi_0}{\bar{\tau}} \le \omega_J - \frac{\omega_J\left(1-\frac{\beta}{3\cos\beta}\right)^6}{4\tau^2} - \tau^2\omega_J + \frac{\varphi_0}{\tau} \end{aligned} \tag{A-23}$$

Combining (5-25), (5-11), and putting all the parameters as listed in Table A-1, (A-23) becomes

$$
\begin{aligned}
&\omega_J - \frac{\omega_J}{4\overline{\tau}^2} - \overline{\tau}^2\omega_J + \frac{\varphi_0}{\overline{\tau}} \geq \\
&1.7625\times10^4 - \frac{1.7625\times10^4}{4\cdot\left(5.8184\times10^{-4}\right)^2} + \frac{2.4162\times10^{20}\cdot(1-0.1822)^3}{5.8184\times10^{-4}} \\
&-\frac{5.8184\times10^{-4}\cdot1.7625\times10^4}{(1-0.1822)^6} = 2.2711\times10^{23}
\end{aligned} \tag{A-24}
$$

The tilted fixed bottom plate
$\alpha_M = 8$, $\rho = 19.3\times10^3$ kg/m^3 $k = 3.3901\times10^{-9}$ N/m, $\varepsilon = 8.854\times10^{-12}$ $L = 125\,\mu$m, $W = 250\,\mu$m, $\delta = 3\,\mu$m, $t = 2\,\mu$m $\beta = 27.7179$ degrees=0.4839 radians according to (3-37) $\frac{\beta}{3\cos\beta} = 0.1822$, $\tau = 5.8184\times10^{-4}$ second, $\omega_J = 1.7626\times10^4$, $\varphi_0 = 2.4162\times10^{20}$ $\eta = 1$, $\mu_{air} = 1.79\times10^{-5}$, $g_s = 100$ Simens

Table A-1 Parameters used to check the Routh Arrays

From(A-24), it can be seen that (A-17) is satisfied, which means (5-59) is satisfied $(a_3a_0 - a_2a_1) < 0$. Till this point, we finish the proof that (5-59) holds.

Reference

[1] R. Muller, "MEMS – the view back… and the vistas ahead", *TRANSDUCERS'01 EUROSENSORS XV*, June 10-14, 2001 Munich, Germany: digest of technical papers, Publisher: Springer, pages 20-23,

[2] D.J. Bishop, et al., "The Little Machines That are Making it Big", *Physics Today*, Vol. 54, Issue 10, Oct. 2001, pages 38-45

[3] D.J. Bishop, et al., "The Lucent LambdaRouter: MEMS technology of the future here today," *Communications Magazine*, IEEE, Vol. 40, Issue: 3, Mar. 2002, pages 75 -79

[4] J.M. Younse, "Mirrors on a chip", *IEEE Spectrum*, Vol. 30, Issue: 11, Nov. 1993, pages 27-33

[5] Van Kessel, et al., "A MEMS-based Projection Display", *Integrated Sensors, Microactuators, & Microsystems (MEMS),* Proceedings of the IEEE, Vol. 86, No. 8, Aug, 1998, pages 1687-1704

[6] C.C. Beatty, "A Chronology of Thermal Ink-Jet Structures," *Tech. Digest Solid-State Sensors and Actuator Workshop*, Hilton Head Island, SC. June 3-6, 1996, pages 200-204

[7] K.E.Petersen, "Silicon torsional scanning mirror", *IBM J. Res. Develop*., Vol. 24, No.5, 1980, pages 631-637

[8] M.C Wu, et al. "Advanced MEMS for photonics", Device Research Conference, 2002. 60th DRC, *Conference Digest*, 24-26 June 2002, pages 13 – 16

[9] M.C. Wu, "Micromachining for Optical and Optoelectronics Systems", *Proceedings of the IEEE*, vol.85, no.11, Nov. 1997, pages 1833-1856

[10] R.S. Muller and K.Y. Lau, "Surface-micromachined microoptical elements and systems," *Proceedings of the IEEE*, Vol.86, No.8, Aug. 1998, pages 1705-1720

[11] W. Noell, et al., "Applications of SOI-Base Optical MEMS," *IEEE Journal on Selected Topics in Quantum Electronics*, Vol. 8, No. 1, January/February 2002, pages 148-154

[12] P.B. Chu, S. Lee and S. Park., "MEMS: The path to large optical crossconnects", *IEEE Communication magazine*, Vol. 40, Issue 3, Mar. 2002, pages 80-87

[13] E.L. Goldstein and L.Y. Lin, "Optical-layer networking with lightwave micromachines: What do service-providers need and when do they need it?", In: *2000 IEEE/LEOS International Conference on Optical MEMS*, pages 27-28.

[14] Nadya Anscombe, "The MEMS-Based Optical Switch," *Photonics Spectra,* Laurin Publishing, Dec. 2003, Vol. 37, Issue 12, pages 68

[15] Nadim Maluf, "*An introduction to microelectromechanical systems engineering*", published Boston : Artech House, c2000.

[16] S. C. Gustafson, et al. "Micro-actuated mirrors for beam steering", in *Miniaturized Systems with Micro-optics and Micromechanics II*, M. Edward Motamedi, et, al, Editors, Proc. SPIE 3008, 1997, pages 91-95

[17] J. B. Lee, et al. "Photovoltaic on-demand high voltage pulse generator as an on-board power source for electrostatic actuator array", ", in *Miniaturized Systems with Micro-optics and Micromechanics,* M. Edward Motamedi, et, al, Editors, Proc. SPIE, vol.3878, 1999, pages 329

[18] T. Ikeda "Fundamentals of piezoelectricity", Publisher: Oxford University Press, 1990

[19] J.W.Judy, R.S Muller, "Magnetically actuated, addressable microstructures", *Journal of Microelectromechanical Systems*, vol.6, no.3, Sept. 1997, pages 249-256.

[20] P. Lorrain, "*Electromagnetism*", 2nd edition, W.H. Freeman and Company, 1990

[21] L. Lin and E. L. Goldstein, "Opportunities and Challenges for MEMS in Lightwave Communications", *IEEE J. on selected topics in quantum electronics*, Vol.8, No.1, Jan./Feb. 2002, pages 163-172

[22] W.C. Tang, et al, "Electrostatic Comb Drive Levitation and Control Method," *Journal of Microelectromechanical Systems*, Vol. 1, No. 4, Dec 1992, pages 170-178

[23] R. Legtenberg, et al., "Comb-drive actuators for large displacements", *Journal of Micromechanical Microengineering*, Vol.6, No.3, Sept. 1996, pages 320-329

[24] V. P. Jaecklin, et al., "Micromechanical comb actuators with low driving voltage", *Journal of Micromechanical Microengineering*, Vol. 2, No. 4, Dec. 1992 pages 250-255

[25] R. Sawada, et al. "Improved Single Crystalline Mirror Actuated Electrostatically By Terraced Electrodes with High-Aspect Ratio Torsion Spring," *Optical MEMS, 2003 IEEE/LEOS International Conference*, 18-21 Aug. 2003 pages 153–154

[25] W.G. Wu, et al, "Electromechanical and optical properties of torsion mirror actuators for optical switch applications", *Optical Switches and Optical Interconnection II*, Lih-Yuan Lin, et al Editors, Proceedings of SPIE Vol. 4907, 2002 pages 36-43

[26] Chuan Pu, and Chris Wu, " Technologies for large-scale optical switching: Recent advances and future prospects", *Optical Switches and Optical Interconnection II*, Lih-Yuan Lin, et al Editors, Proceedings of SPIE Vol. 4907, 2002, pages 23-30

[27] T.E. Stern, and K. Bala, "Multiwavelength Optical Networks: A layered Approach", Reading, MA: Addison-Weslesy, 1999

[28] D.J. Bishop, et. al., "The rise of optical switch," *Scientific American*, Jan. 2001, pages 88-94

[29, 1-2] V.A. Aksyuk, et. al. "Beam-steering micromirrors for large optical cross-connects", *J. of Lightwave Technology*, Vol.21, No. 3, Mar. 2003, pages 634-642

[30, 2-9] V.A. Aksyuk, et al. "238x238 micromechanical optical crossconnect", *IEEE Photonics Technology Letters*, Vol. 15, Apr. 2003, pages 587-589

[31] J. Kim, et al., "1100x1100 port MEMS-Based optical crossconnect with 4-dB Maximum loss", *IEEE Photonics Technology Letters*, Vol.15, No.11, Nov. 2003, pages 1537-1539

[32] D. H. S. Maithripala, et. al., "A port-controlled Hamiltonian approach to control of an electrostatic MEMS actuator", *Proceedings of IMECE'03, 2003 ASME International Mechanical Engineering Congress*, Washington, D. C., Nov. 15-21, 2003, pages 687-691

[33] E. K. Chan, and R. W. Dutton, "Electrostatic micromechanical actuator with extended range of travel", *Journal of Microelectromechanical Systems,* Vol. 9, No. 3, 2000, pages 321-328.

[34] L. Wang, et. al. "Stroke-length control of a MEMS device", *IEEE conference, ISIE'2000*, Cholula, Puebla, Mexico, pages 535-539

[35] J. I. Seeger and S. B. Crary, "Stabilization of Electrostatically actuated mechanical devices", *Proc. of the Ninth Int. Conference. On solid-state sensors and actuators (Transducers'97),* Chicago, IL, June 16-19, 1997, pages 1133-1136

[36] D. C. Green, "*Digital Electronics*", 5th edition, Harlow, Longman, 1999

[37] http://www.fairchildsemi.com/ds/74/74F675A.pdf

[38] D. T. Neilson, et.al, "Fully provisioned 112x112 micro-mechanical optical crossconnect with 35.8Tb/s demonstrated capacity", Optical Fiber Communication Conference, 2000, Vol. 4, Mar. 7-10, 2000, pages 202-204

[39] V. A Aksyuk, et.al, "238x238 surface micromachined optical crossconnect with 2dB maximum loss", Optical Fiber Communication Conference and Exhibit, 2002. OFC2002, Vol. 4, Mar. 17-22, 2002, pages FB9-1 – FB9-3

[40] Stephen D. Senturia, "Microsystem design", Kluwer Academic Publishers

[41] Y. Ma and K. Timko, "Multichannel, high-voltage IC amplifiers for optical MEMS", Vol.18, Issue 8, *Lightwave*, July 2001, pages 85-88

[42]http://www.photonics.com/dictrionary

[43] http://civil.colorado.edu/courseware/struct_labs/wheatstone.html

[44] Nathan Ida, "Engineering electromagnetics", 2nd edition, Springer-Verlag New York

[45] J. Buhler et, al. "Electrostatic aluminum micromirrors using double-pass metallization", *Journal of Microelectromechanical Systems*, vol. 6, issue 2 , Jun 1997, pages 126-135

[46] D. H. S. Maithripala, "Capacitive stabilization of an electrostatic actuator: An output feedback viewpoint", *Proceedings of the American Control Conference, Denver, Colorado*, Jun 4-6, 2003, pages 4053-4058

[47] K. Chang, et al; "Squeeze film damping effect on a MEMS torsion mirror", *Journal of Micromechanics and Microengineering*, Vol.12, No.5, Sept. 2002, pages 556-561

[48] Shen, Liang Chi and Kong, Jin Au, "Applied electromagnetism", 3rd edition, PWS Publishing Company, pages 382-383

[49] Gui, xingmao, et al, "Math handbook", Shanghai Science Publication, 1993

[50] T. F. Elbert, "Estimation and control of systems", Van Nostrand Reinhold Company, 1984

[51] J.E. Fouquet, “Tutorial: waveguide-based optical cross-connect switches”, OFC (Optical Fiber Communication Conference and Exhibit), 17-22 March. 2002, pages 583

[52] J. E. Fouquet, “Compact optical cross-connect switch based on total internal reflection in fluidic-containing planar lightwave circuit”, Optical Fiber Communication Conference and Exhibit, 2000, OFC 2000, Baltimore, March 2000, paper TuM1-1

[53] S. Venkatesh, et al, “Recent advances in bubble-actuated cross-connect switches”, Lasers and Electro-optics, 2001, CLEO/Pacific Rim 2001. The 4th Pacific Rim Conference on, Vol.1, 15-19 July 2001, pages I-414- I-415

[54] T. Watanabe, et al. “Silica-based PLC 1x128 thermo-optic switch”, Optical Communication, 2001. ECOC ‘01. 27th European Conference on, Vol.2, Sept. 30-Oct. 4, 2001, pages134-135

[55] R. Kranhenbuhl, et al. “Performance and Modeling of Advanced Ti:LiNbO3 digital switches”, *Journal Lightwave Technology*, Vol.20, No.1, Jan 2002, pages 92-99

[56] C.M. Gallep and E. Conforti, “Reduction of Semiconductor Optical Amplifier Switching Times by preimpulse step-injected current technique”, *IEEE Photonics Technology Letter*, Vol. 14, No, 7, July 2002, pages 902-904

[57] X. Ma and G.S. Kuo, “Optical switching technology comparison: optical MEMS vs. other technologies”, *IEEE Optical Communications magazine*, Vol. 41, Issue 11, Nov. 2003, pages S16-S23

[58] K. C. Nguyen, “3-D MEMS optical switch for fiber optic communication applications”, *Optical Switches and Optical Interconnection II*, Lih-Yuan Lin, et al Editors, Proceedings of SPIE Vol. 4907, 2002, pages 31-35

[61] M. F. Gardner and J. Barnes, “Transients in Linear System” , Vol.1, New York, John Wiley & Sons, Inc.1957, page 56

[62] J. B. Muldavin and Gabriel M. Rebeiz, “Nonlinear Electro-Mechanical Modeling of MEMS Switches”, *2001 IEEE MTT-S International Microwave Symposium Digest*, Vol.3 Piscataway, NJ, USA: IEEE, 2001, pages 2119-2122.

[63] F. Pan etc, “Squeeze film damping effect on dynamic response of a MEMS torsion mirror”, *Journal of Micromechanics and Microengineering*, Vol.8, No.3, Sept. 1998, pages 200-208.

[64] S. Simom, "Modeling and design aspects of the MEMS switch", International Semiconductor Conference, 2003, Vol. 1, pages125-128

[65] J. B. Star, "Squeeze-film damping in solid-state accelerometers", *Tech. Digest IEEE solid State Sensor and Actuator Workshop (Hilton Head Island, SC, 1990)*, 1990, pages 44-47

[66] Young W C 1989 "Roark's formulas for stress and strain", 6th edition, New York: McGraw-Hill, page 348

[67] H. Nishiyama and M. Nakamura, "Form and capacitance of parallel-plate capacitors", *IEEE Transaction. On components, packing and manufacturing technology-Part A*, Vol. 17, No.3, Sept. 1994, pages 477-484

[68] Y. Nemirovsky and O. Bochobza-Degani, "A methodology and model for the pull-in parameters of electrostatic actuators", *Journal of Microelectromechanical systems*, Vol. 10, No.4, Dec. 2001, pages 601-615

[69] J. Buhler et, al. "Electrostatic aluminum micromirrors using double-pass metallization", *Journal of Microelectromechanical systems*, Vol. 6, Issue 2, Jun 1997, pages 126-135

[70] http://www.dcsc.tudelft.nl/~sc4030/collegesides/sc4030college4.pfd

[71] F. L. Lewis, and V. L. Syrmos, "*Optimal Control*", 2nd edition, John Wiley & Sons, Inc.

[72] R. W. R. Darling, "Converting matrix Riccati equations to second-order linear ODE", *SIAM Rev.* Vol. 39, No.3, Sept. 1997, pages 508-510

[73] L. Lin et al, "On the expandability of Free-Space Micromachined Optical Cross Connects", *Journal of Lightwave Technology*. Vol. 18, No. 4, April, 2000, pages 482-489